Spectroscopic Analysis of GRB 060526

Josefine Helene Selj

Thesis Submitted for the Master’s Degree

Institute of Theoretical Astrophysics
University of Oslo

June 2007

Acknowledgments

First of all, I want to thank my supervisor, Andreas Jaunsen, for introducing me to such a new and intriguing field as Gamma-Ray Bursts. I am very grateful for the patience and efforts he has put down to answer my continuing questions and that there was always time when I came knocking on the door. The fantastic opportunity I got to visit La Silla Observatory in Chile gave memories for life - and some insight in the workings of telescopes and GRBs was also won. Thank you.

Dark Cosmology Center in Copenhagen, and particularly Johan Fynbo, is thanked for providing the spectroscopic data for this thesis. During the week spent at Dark I was guided through the first fumbling introduction to IRAF - and pingpong. Thank you.

Jan-Erik is thanked for the late hours spent in the Danish Telescope at La Silla and for teaching me about what we saw - GRB host galaxies, and how to see it - operating the telescope. Also thanks for tips and help with IDL. Thank you.

The people in and around Fysisk Fagutvalg and Fysikkforeningen over the last years have been an invaluable source of motivation, inspiration and great fun. Especially I want to thank Marte for her friendship and endless discussions on the shortcomings of physics, cosmology and men. Also thanks to Gorm for his patience when this thesis was all I could talk about, and his care when I hardly could walk about. Thanks to Anders, Jostein, Yngvild and Henning for sharing time, opinions and friendship throughout my time at Blindern. It would not have been the same without you. Thanks to Sofie, Kosovare, Thale, Iselin, Stefano, Hanne Sigrun, Nicolaas, Glenn and everybody else who has made the study hall of Astro a great place to work and socialize. Thank you.

Finally, I want to thank my parents for encouraging me to study and for being so genuinely interested in and enthusiastic about what I do. Thank you!

Contents

Chapter 1

Introduction

As starting point for this thesis, a short historic review on GRBs is given, based primarily on the paper Zhang & Mészáros (2004). A few lines of history is illustrative to see where it all began and what is accomplished so far. The main subject of this introduction is to present our motivations and goals for the thesis; to put forward what we wish to accomplish with our data and connect this to existing trends in the GRB-field. The introduction is ended by a short outline of the contents of the remaining pages.

History

The first Gamma-ray Bursts (GRBs) were discovered in the late 1960s, by the US Vela satellites. These satellites were built to detect the gamma-radiation from secret nuclear weapon tests, and Vela really did pick up occasional bursts of gamma rays from unknown sources. In the period of July 1969 - July 1972, 16 bursts were detected. However, the satellites picked up the bursts at slightly differing times, which enabled the direction to be decided. Luckily, the gamma-rays were not from nuclear weapons, they were gamma-ray bursts. Neutron stars and Active Galactic Nuclei (AGNs) were also discovered around the same time, but while the nature of neutron stars and AGNs were uncovered relatively rapidly, GRBs remained a mystery for decades. The lack of observational data left freedom for theoreticians and modelers to play around, and the number of theories grew thereafter. It was not until the 1990s that our observational knowledge started to accumulate. BATSE (Burst And Transient Source Experiment), which orbited around Earth as a part of NASA's Compton Gamma-Ray Observatory, was the first instrument which could locate the positions of the gamma-ray bursts with reasonable accuracy (better than Vela). In fact, as late as in 1995 a debate on the cosmic origin of GRBs was held - on the 75th year anniversary of the famous Curtis/Shapely debate. One of the main arguments for GRBs to lie within the galaxy was that for them to be seen at high redshifts, their energies must be enormous. It was BATSE which provided evidence for an isotropic distribution of GRB's, indicating their cosmological origin (although the very same arguement was also used to advocate a galactic origin). These days nobody questions the cosmic origin of GRBs, as redshift measurements clearly place these events at very large distances from earth. Regarding the energy, it seems like the astronomical community today agrees that the gamma-rays are probably collimated - the matter ejected in two jets - reducing the required amount of energy to that comparable with a hundred typical supernovae, i.e. 10^{52} ergs. In fact, one type of GRBs seem to be intimately connected to supernovae. But now I anticipate the events. The next big step of progress came with Beppo-SAX, an Italian satellite launched in 1996, which pinpointed the first GRB low energy X-ray afterglow. Since our atmosphere is opaque to gamma-rays, satellites are our only option for doing the initial detections, and in these days Swift is doing an excellent job detecting an ever growing number of GRBs for us to follow up on. It has given enormous progress in the field, since its speedy response and accurate localization has made it possible to rapidly follow up with ground based observations.

Motivation

As Gamma-ray Bursts are related to a range of other fields of astrophysics, they have become a popular object of study; firstly, their close connection with the deaths of super massive stars (Hjorth et al., 2003; Stanek et al., 2003) make GRB studies relevant to the fields of stellar structure and evolution, supernovae and supernovae remnants. This connection also make GRBs highly relevant in studies of the star formation rate of the early universe. With an improved understanding of GRB properties and possible biases in choice of hosts, GRBs might become the ideal probe of star formation (Fynbo et al., 2007). Secondly, studies of the properties of host galaxies, as well as the GRB locations within the hosts provide valuable information about the nature of GRB progenitors. In addition, they can play a similar role to AGNs by probing the intergalactic material, only their luminosities are even greater and can enable us to look even further into the early history of the universe (Fynbo et al., 2006a). GRBs may also play the role of standard candles, but as of today, the relation between their observable features and their luminosity is not tight and accurate enough to give robust results. There is even hope that as more and more distant GRBs are detected, a region of complete absorption due to neutral hydrogen, called the Gunn-Peterson effect, will be seen. This would signalize that the epoch before complete ionization is reached (Barkana R. & Loeb, 2001). Also, several GRB progenitor scenarios are believed to generate gravitational wave signals, making GRBs one of the major targets for detecting gravitational waves (Zhang & Mészáros, 2004). Central engine studies have promoted studies about the mechanisms for extracting energy from accretion disks or spinning black holes (Zhang & Mészáros, 2004). These are some of the general motivation factors for studying GRBs. I will now turn to the specific motivations for this thesis.

This thesis presents a full analysis of low resolution spectroscopic VLT data of the Gamma-ray Burst 060526. It illustrates what can, and what cannot, be done with low resolution data. There was one aspect of particular interest to us when we started this work, namely the metallicity of the absorbing system in which the GRB is embedded. In addition there were several other properties we wanted to look at, if possible. For instance, which abundances can be determined and how are they affected by dust and ionization? What - if anything - may these abundances reveal about the nucleosynthetic history of the absorbing medium? The column density of this GRB was known to be low compared to the majority of GRBs, why is this so? Finally, we wished to obtain an estimate of the the star formation rate of the host galaxy of GRB 060526.

The potential GRBs hold as powerful probes of the star formation rate (SFR) in the early universe is one of the most important reasons to study GRBs. The SFR is again intimately linked to the formation of galaxies and thereby large structures in the universe. Detection of Lyα in emission can give an estimate of the SFR in the host galaxy of GRB 060526. Even lack of such emission can give an upper limit on the SFR. However, the value of GRBs as sources of information on SFR steams not only from the SFR of the host galaxy which can directly measured, but also indirectly from the fact that GRBs are related to supermassive stars and therefore trace the star formation in the universe.

To fully exploit the potential of GRBs as tracers of SFR, the conditions needed to produce GRBs must be known (Fynbo et al., 2007) and possible selection biases must be uncovered. Therefore host galaxy morphology, luminosity, metallicity and mass in addition to progenitor models, are of importance, as these properties may shed light on any existing biases. Previous studies indicate that the majority of GRB host galaxies are blue and subluminous (Sollerman et al., 2005; Fruchter et al., 1999; Jakobsson et al., 2005), and in fact they are significantly fainter and more irregular than the hosts of the core-collapse supernovae (Fruchter et al., 2006). It is however not clear why this is so. Among the suggestions is a possible metallicity bias (Fruchter et al., 2006); if the hosts are generally low-mass galaxies, low metallicity may be inferred from the mass-metallicity correlation. In addition, calculations (Woosley, 2005) suggest that the dynamics of the preferred

Wolf-Rayet progenitor model depend on low metallicities to produce GRBs. Although most spectra are low resolution, making it is difficult to acheive sufficiently accurate metallicities, the number of GRBs with inferred metallicities is continuously growing, increasing the probability of resolving this issue. In this context, the metallicity of GRB 060526 is another piece in the puzzle and its placement relative to the existing picture will be discussed in the coming pages.

Abundance studies may give detailed clues on the cosmic chemical evolution. This is, however, a science with small margins, errors in column densities and metallicities may easily be mistaken for nucleosynthetic patterns, or dust and ionization may alter the relative abundances. Even though we expect that higher resolution data will be needed to provide the required accuracy to infer nucleosynthetic patterns, an attempt to constrain abundance ratios will be made. The column density of neutral hydrogen should however be easily obtained as the Lyα absorption feature is within the wavelength range of the data. In addition to being essential for metallicity studies, the amount of neutral hydrogen is also interesting in itself. The great majority of GRBs are embedded in damped Lyman alpha (DLA) systems with $\log N(\mathrm{HI}) > 20.3$, but GRB 060526 has a reported column density lower than this. GRBs are believed to originate in galactic-like molecular clouds, therefore it is an open question why some GRB environments have significantly lower H I column densities than the molecular clouds (Jakobsson et al., 2006).

Thesis Outline

In Chapter 2, I give a general picture of the most important aspects of Gamma-ray Bursts, beginning with the classification into short and long bursts, then concentrate on long GRBs which are the subject of this thesis. The rest of Chapter 2 will deal with their progenitor models and host galaxies and place GRBs within a cosmological context. In Chapter 3 I take a closer look at spectroscopy, one of the best tools we have to study the universe and the basis of this thesis. The actual spectroscopic data are presented in Chapter 4. The same chapter also guides the reader through the necessary reductions steps. The actual analysis of the spectra are carried out in Chapter 5; absorption lines are identified and two methods, curve of growth analysis and Voigt profile fitting, are used to measure column densities of the unblended lines. Based on these values metallicity, dust-to-gas ratio and abundances are derived in Chapter 6. Discussions of the derived properties of the ISM of GRB 060526 also follow in this chapter. Finally, the summary and outlook remain for Chapter 7.

Chapter 2

Background

Gamma-ray Bursts are the most energetic cosmic events in today's universe. It is not easy to find a trustworthy progenitor for these extravagant processes - how can such amounts of energy be released? Today more than 500 GRBs have been observed and in this section I will describe the different aspects of GRBs, starting with their classification into two main types, long and short, and continue with more detailed information about long bursts. The topics include the progenitor in the collapsar model, the fireball shock model, explaining the prompt emission and afterglow, and finally, the host galaxies. My thesis will mainly be concerned with the afterglow spectrum and the surrounding absorbing medium, not so much with the progenitor and its physics. However, I feel that some information about the burst itself is important for the overall picture. Much of this chapter is based on the papers Piran (2005) and Zhang & Mészáros (2004), while Section 2.3.1 is largely based on the paper Fryer et al. (2007). When using additional papers, these will be cited. However, before getting into the Gamma-ray Bursts, a brief detour to look at the relationship between redshift and distance is useful. For any valuable information to be gained from GRBs – and most other astronomical objects – it is critical that we know their distance. At cosmological distances, one can either use a luminosity-distance relation, photometric redshift measurements or one can measure the redshift by spectroscopic line-identification. The latter is done for all GRBs whenever possible. Redshift is usually not 'translated' into distances, but used as a measure of distance – and time – itself. Distances to GRBs are almost always referred to in terms of redshift, so also in this thesis.

2.1 Redshifts and cosmological distances

The *cosmological redshift, z,* of an object has the fortunate quality of being directly observable, it just requires comparing the observed wavelengths of spectral lines with their rest wavelengths. Therefore redshifts are such a convenient way of measuring distances. As opposed to Doppler redshift, cosmological redshifts are not caused by random motion of objects, it is the result of space itself stretching. The ratio between the emitted and observed wavelengths is equal to the expansion of the universe in this time-span, i.e. the ratio of the scale factors of the universe at the two times

$$\frac{a(t_0)}{a(t_e)} = \frac{\lambda_0}{\lambda_e} = z + 1 \,,$$

where λ_0 is the observed wavelength, λ_e is the emitted wavelength and the last equality comes from the definition of z. Too be more accurate, the scale factor is a function of time which relates physical coordinates (proper coordinates) to coordinates moving along with the expansion (comoving coordinates). The current value of a is equal to one: $a(t_0) = 1$, where t_0 is the present age of the universe. So, the redshift measures how much the universe has expanded between the times of emission and reception of the signal. Now that we have the connection between redshift and the scale factor, we can go on to see that the scale factor is related to distance through Hubble's law

$$v(t) = \frac{\dot{a}(t)}{a(t)} d_p(t) = H(t) d_p(t) \,,$$

where $v(t)$ is recessional velocity, $H(t) \equiv \dot{a}(t)/a(t)$ is the Hubble parameter and $d_p(t)$ is the proper distance. The proper distance is the length of the geodesic between two points at a specified time and therefore depend on the chosen cosmology. By comparing redshifts with distance measurements obtained using other methods, cosmological models may then be tested. From Hubble's law we see that the points in the universe are moving apart with a speed proportional to their distance. Note that mathematically and observationally there is no difference between regular Doppler redshifts and cosmological redshifts. It is the *reason* for the shifts that distinguish them. The present value of the Hubble constant is obtained after numerous measurements of velocities of objects and their respective distances. The best measurements of the current value of the Hubble parameter indicate that $H(t_0) = 72 \pm 8 \mathrm{kms}^{-1} \mathrm{Mpc}^{-1}$ (Freedman et al., 2001).

2.2 Classification of GRBs

GRBs are divided into two primary groups: *short bursts* and *long bursts*. Short GRBs (SGRB) have a shorter duration and emit a larger fraction of their energy as high energy photons than long GRBs (LGRB). We say that the SGRBs are hard, and the LGRBs are soft. Figure 2.1 clearly illustrates how GRBs divide themselves into one group with short duration (SGRB) and another group with

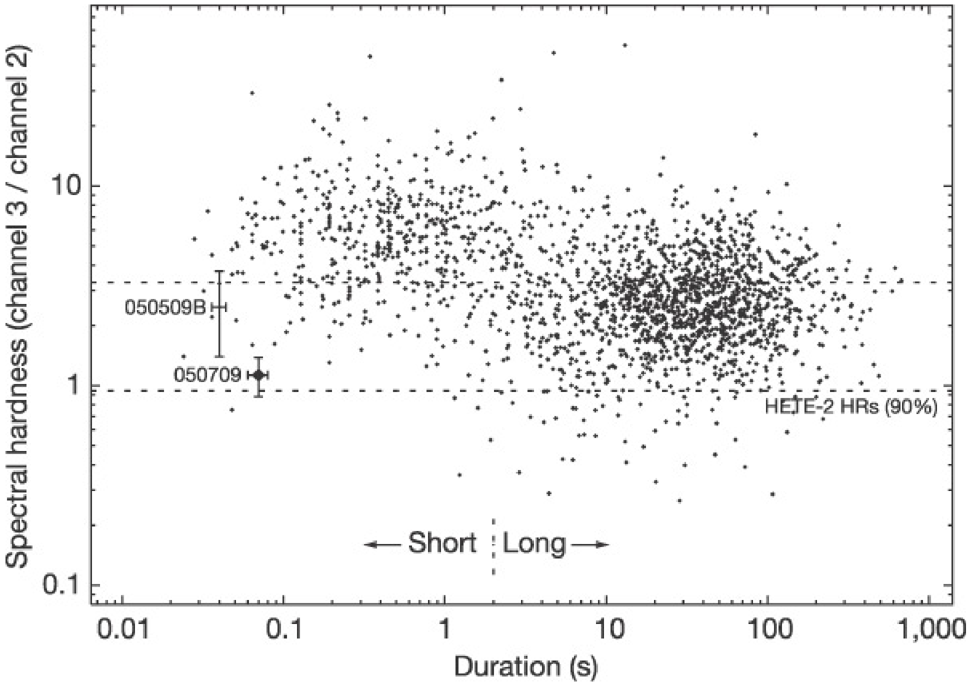

Figure 2.1: Long and short GRBs. From observations it is evident that the two groups have different spectral properties. The figure is from Hjorth et al. (2005). The spectral hardness is measured by integrating the counts above background during the time in which 90 $\%$ of the photons arrive, T_{90}, in different energy ranges (Kouveliotou et al., 1993). Here the ratio of $100 - 300$ keV and $50 - 100$ keV is used.

longer duration (LGRB) with a division line at approximately 2 seconds. Other subgroups of GRBs exit, including dark bursts, the recent discovery of supernova-less LGRBs and the closely GRB-related X-ray flashes. I will take a brief look at each. Not all the properties we use for characterizing GRBs are necessarily intrinsic, and so not all subgroups of GRBs must be taken from different populations. It might simply be observational biases messing with the big picture.

Information on *short bursts* is limited, because until recently no counterpart to the gamma-rays were observed at any other frequency. However, starting with the detection of the X-ray afterglow of the short burst GRB 050509b, several more afterglows in both optical, X-ray and radio wavelengths have now been detected. These data reveal that the host galaxies of short bursts have little star formation and the SGRBs do not have an associated supernova, thus strengthening the theory of differing progenitors for long and short GRBs. Promising suggestions for the progenitor of SGRBs so far include the model where two neutron stars coalesce or a neutron star is devoured by a black hole (Nakar, 2007). This causes an enormous release of gravitational potential energy. The lack of material around such a system means that the energy release stops as soon as the merger is complete - hence the short duration of the burst.

X-ray flashes (XRFs) have similar durations to the long, soft GRBs, but they have low gamma-ray flux, high X-ray flux and so their spectral peaks are at lower energies. Afterglow emission in X-ray, optical and near infrared has been detected and their position has indicated that XRFs are found in star forming galaxies. The recent event XRF 060218 associated with SN 2006aj clearly demonstrated that some XRFs originate in the core collapse of a massive star in a Type Ic supernova (Sollerman et al., 2006; Pian et al., 2006). One theory suggests that it is the difference in viewing angle that creates XRFs (Levan et al., 2006). However, observations of the GRB 060218/XRF 060218 indicate that the lower luminosity of XRFs is an intrinsic property, not a result of our viewing angle (Pian et al., 2006). The supernova associated with XRF 060218 has properties between those of a normal supernova of type Ibc and those powering a gamma-ray burst.

There is no unambiguous definition of what a *dark burst* is. A LGRB where there is no optical afterglow is usually dubbed a dark burst, but some choose to narrow down the definition to only include bursts where there are no afterglow, regardless of band. Jakobsson et al. (2004) propose an operational definition of dark bursts as those bursts that are optically sub-luminous with respect to the fireball model, i.e. that have an optical-to-X-ray spectral index $\beta_{OX} < 0.5$. There are several suggestions to what might be the cause of dark bursts. Observational biases such as obscuration by interstellar matter or a high redshift may be responsible, or, the darkness is intrinsic and we have a new real subgroup of LGRBs. Mészáros et al. (2005) argue that the observational biases can explain the ratio between bursts with an afterglow (in any band) and dark bursts. To keep the GRB theory as simple as possible this is also the most appealing thought.

The detection of GRB 060614 (Fynbo et al., 2006a; Gehrels et al., 2006), a long duration GRB (102 s) with a spectrum that fits better within the short GRB subclass and a missing supernova, bred a new subclass of GRB dubbed *supernova-less LGRBs*. There is one more GRB fitting into this class, namely GRB 060505 which had a duration of 4 s. Some argue that these should be considered a more energetic version of the short-hard class of bursts (Zhang et al., 2007) and that the classification of GRBs should be changed to take such events into account.

2.3 Long Gamma-ray bursts

2.3.1 The progenitor and the collapsar model

The long bursts are, at least in some cases, connected with the beamed energy of a specific kind of supernova event, known as a hypernova. The term hypernova may be used to denote all core-collapse explosions which exhibit stronger than normal explosion energies and/or evidence for asymmetries. With this definition, the ’supernovae’ associated with GRBs are a subset of the hypernova class, believed to have a different engine than normal supernovae. Our best indication of the relation between supernovae and GRBs is that several LGRBs have shown late-time ’bumps’ in their light-curves. These ’bumps’ arise when the light from the supernova starts to out-shine the declining GRB afterglow. There are now three particular certain cases establishing that long-duration gamma-ray bursts coincide with the explosions of very energetic core collapse supernovae. These are SN 1998bw with GRB 980425 (Tinney et al., 1998), SN 2003dh with GRB 030329 (Hjorth et al., 2003) and SN 2003lw with GRB 031203 (Thomsen et al., 2004). However, 2006 brought a surprising discovery of two GRBs with no accompanying supernova, GRB 060505 and GRB 060614 (Fynbo et al., 2006b). The progenitor of these supernova-less GRBs may be the same as for short GRBs, or they may demand a progenitor-model of their own, maybe one of the many models suggested before the definitive association between GRBs and supernovae. It might be time for some serious dusting and at-the-bottom-of-the-drawer searching, but, as there is not much hope of exiting discoveries in my drawers, I will concentrate on the most widely accepted model for supernovae-associated LGRB, the *collapsar model*. This model suggests that the explosion is produced after a massive star collapses to a black hole. The energy released during accretion of the in-falling stellar material onto this black hole provides the energy for the explosion. However, this can only occur if the energy does not also accrete onto the black hole. The collapsar model provides three general constraints which may help determining the exact type of progenitor. Firstly, a black hole must be formed. Secondly, the model must produce sufficient angular momentum in the star to form a disk around the black hole. Thirdly, the model must eject the hydrogen envelope. Two main types of progenitors have been suggested in the collapsar model; single stars and binaries.

In both cases, the preferred progenitor-stars are Wolf-Rayet (WR) stars (Campana et al., 2006b; Woosley & Heger, 2006; Hirschi et al., 2005). WR stars are evolved, hot, massive stars which have very strong stellar winds. It is a normal stage in the evolution of massive stars, in which strong, broad emission lines of helium and nitrogen ("WN" sequence) or helium, carbon, and oxygen ("WC" sequence) are visible. Such super massive stars, i.e. stars with a Zero Age Main Sequence (ZAMS) mass between 40 and 100 solar masses, collapse when their silicon has fused into iron and the last step on the nuclear burning-ladder is reached. When there is no further energy to gain from nuclear burning, radiation pressure caves in for gravity and a core collapse supernova signalizes the death blow of the star. Depending on the mass - and the mass-loss - of the star, it may either be held up by degenerate neutron pressure, or collapse entirely, becoming a neutron star or a black hole, respectively. The angular momentum of the collapsing star causes the formation of a spinning accretion torus around the newly formed black hole. Gravitation pulls the surrounding stellar material into this accretion disk. The polar regions are quickly cleared of gas, such that just 10 seconds after the burning ended it has around a tenth of the density of the equatorial region. This allows energy to be released in two jets along the rotation axis. It is probably collisions between different layers of gas and the following shocks in these jets, which cause the actual gamma-ray burst. If the earth happens to lie along the rotation axis (i.e. the jet axis), it receives a huge burst of gamma-rays, a LGRB.

However, it is also clear that the collapse of WR stars not always results in a GRB, since the GRB rate is not great enough compared with SNe. The need for a selection process is therefore evident and all good spectroscopic identifications so far point in the direction of SNe Ic (Fruchter et al., 2006) - that is, the core collapse supernovae which don't show hydrogen nor helium in their spectra, being the underlying supernovae. But, even within this subclass of supernovae, only a small fraction can be able to produce GRBs if the observed number of GRBs are to be explained.

In addition to the selection problem, there is also a problem of retaining enough angular momentum in the inner regions. For single stars, calculations show that typical massive stellar deaths probably produce *slow* pulsars with less angular momentum than what is needed to produce a GRB. This is true for the most common variety of supernova, Type IIp, which results from the deaths of red supergiants (RSGs). If instead more massive stars are considered, and especially stars that lost their hydrogen envelopes early on, their cores can rotate more rapidly. Therefore theory suggest that it might be easier to make a GRB if the star does not go through the red supergiant phase. Even taking this into account it is theoretically very difficult to produce GRBs from single WR stars. One way out of this dilemma, outlined by Woosley & Heger (2006), is to decrease the standard WR mass-loss rates currently in use. Three arguments are used to justify this scenario. First, one does expect some scatter in the mass-loss rates of stars having the same mass, composition and angular momentum on the main sequence. Second, WR stars are known to have lower mass-loss rates than other massive stars. And finally, the strong dependence on metallicity must be taken into account; the lower the metallicity, the lower the mass loss. Therefore low metallicity WR stars may be able to attain a rotation rapid enough to produce GRBs. Calculations and models (Woosley & Heger, 2006) indicate an upper metallicity limit of about one third solar, $0.3Z_{\odot}$.

The classical binary model involves mass transfer; the problem of loss of angular momentum in a stellar wind can be avoided if the hydrogen envelope is ejected via binary mass transfer. When the most massive star in a binary system evolves off the main sequence, it expands and envelopes its companion. The companion then spirals in towards the core of the massive star, ultimately ejecting the hydrogen envelope of the massive star. This is only one of several models involving binary systems. More exotic models also exists, for instance the case where the two stars in the binary have nearly equal masses and hence the companion evolves off the main sequence before the more massive star collapses. The stars merge and produce a single massive star which has lost most of the hydrogen envelopes of both stars. Another suggestion proposes that the merger of a neutron star of black hole with its companion could produce a collapsar-like outburst. A general trend in the binary models is that they seem to fit the observed metallicity constraints better than the single star progenitor model.

In time, observational constraints will hopefully be strong enough to differentiate between the various progenitors. One important observational constraint is metallicity and for high redshifts, absorption line spectroscopy is one of the best methods to obtain information about abundances. Also the rate of bursts, the surrounding environment and host galaxy morphology can contribute to settle the subject of LGRB progenitors.

2.3.2 Emission from a GRB - the fireball shock model

The standard fireball shock model explains the mechanism creating the observed emission from GRBs. It is the most widely used, and verified, theory for interpreting the GRB afterglow and prompt emission. The fundamental observations constituting the basics of this model are fairly straight forward. The millisecond variabilities constrain the size of the initial burst region. The emission places a lower limit on the amount of energy. Such amount of energies in such small volumes must imply a black hole, which then constitutes the inner engine. A model for the emitted radiation must be able to explain why it is non-thermal and also how and where the prompt- and afterglow emission is produced. The 'fireball' of this model refers to the jet of material moving at relativistic speed. It is assumed to be a mix of photons, electron/positron pairs and a small amount of baryons. The fireball behaves as a shock wave as it races outward, plowing into and sweeping up matter in its way. Gamma-rays are produced from the series of collisions and shocks arising when fast moving material in the jet overtake slower moving matter, this is called *internal shocks* and are responsible for the *prompt emission*. In this scenario the *afterglow emission* of gamma-ray bursts are synchrotron radiation created when the outflowing material collides with the interstellar medium, also called *external shocks*. Initially, X-rays result, but as the matter continue to loose kinetic energy, a wide range of frequencies, through visible and down to radio, can be seen. This was a rough sketch of the standard fireball shock model. A few aspects of this theory deserve a little more attention. The afterglow and the radiative processes behind it are central as this is the origin of the analyzed spectrum. For completeness, prompt emission will also receive a closer look.

Prompt emission and variability

The *prompt emission* decides the duration of the burst, and is the origin (together with the hardness of the spectrum) of the division between long and short GRBs. The prompt emission is the initial gamma radiation picked up by satellites orbiting the earth. It works as the alarm clock for initiating follow-up observations from ground. The duration of the prompt emission spans five orders of magnitude, from 0.01 s for short bursts to more than 100 s for long bursts. Common measures for the duration are T_{90} or T_{50}, which correspond to, respectively, the time in which 90% and 50% of the photons arrive. The division line between the two appears to be approximately $T_{90} = 2$ s, and typical values are 20 s for long bursts and 0.2 s for short bursts. Even if the total prompt emission lasts for as long as 100 seconds, the majority of the energy can be released in periods of only milliseconds. For GRBs to vary on such short time scales, the size of the emitting region must be very small, or the different distances and finite speed of light would in effect ’smear’ the emission out in time. However, if the amount of energy involved in a typical GRB really was produced in such a small space, the system would be opaque to photon/photon pair production, making the burst far less luminous and with different spectral fingerprint than what is observed. Therefore one concludes that the emitting system is moving towards us at relativistic velocities; the burst is then compressed in time due to the relativistic Doppler effect - the emission seems to be coming from a much smaller area than it in fact does. A related question is why this variability is there at all. If the GRBs are due to matter moving towards us, as the argument above enforces, why the great variation? The generally accepted explanation for this is the ’internal shocks’, collisions of multiple shells traveling at slightly different velocities. Such a collision will convert enormous amounts of kinetic energy into random motion of particles, amplifying all emission mechanisms. The most important radiative processes are likely synchrotron radiation and inverse Compton emission.

Afterglow

The radiation in other wavelengths following the prompt emission at gamma ray wavelengths is denoted GRB *afterglows*. Afterglows have been detected in the X-ray, the optical/infrared and the radio bands. The very first afterglow was detected in X-rays by BeppoSAX in February 1997, until then there were no known counterparts to GRBs. BeppoSAX also determined the position, which led to the detection of an optical afterglow. The first radio afterglow was detected in GRB 970508. Today more than 250 X-ray afterglows are observed. Not all bursts have afterglows detectable in all bands. Using the definition of dark burst as a burst with an X-ray to optical slope too shallow for the synchrotron fireball model (Fynbo et al., 2007), at least 25% of swift GRBs are dark.

The x-ray afterglow is the first and strongest, but also the shortest signal. It seems to begin while the burst is still ongoing. The X-ray flux depends on the frequency and the time. High frequency and long time means a smaller X-ray flux. The overall energy emitted in an X-ray afterglow is usually a few percent of the total burst energy (Piran, 2005). The X-ray afterglow is present in 90% of the bursts. One day after the burst, the observed *optical afterglow* typically has a magnitude [1] of $19 - 20$. The signal decays as a power law in time, and, like the X-ray afterglow it is also a power law in frequency. Many afterglow light curves show a break to a steeper declination. This break is usually interpreted as a jet break that allows estimates of the opening angle of the jet, and then indirectly of the viewing angle. In most cases the afterglow fades within a few weeks, and reaches a plateau corresponding to the emission of the host (Piran, 2005). This is important to know when observing host galaxies, since we need to know at what time the host galaxy will be the major contributor to the observed light. The continuum spectra are broken by absorption (emission) lines, corresponding to absorption on the way from the source to earth. *The radio afterglow* peaks last, and this happens about 10 days after the burst. Only about one fifth of the GRBs with observed x-ray afterglow have radio afterglow.

Light curves are a common way to illustrate how the flux of an object evolves with time. The signatures of both the prompt emission and the afterglow is clearly visible in Figure 2.3.2. In several cases, the light curve shows red bumps after

---

[1] The term magnitude is here referring to the apparent magnitude, i.e. the brightness of the object as seen from earth measured on a logarithmic scale with the bright star Vega approximately at the zero point.

a week to a month (depending on the redshift of the burst). As previously mentioned, these bumps are interpreted as evidence for an underlying supernova.

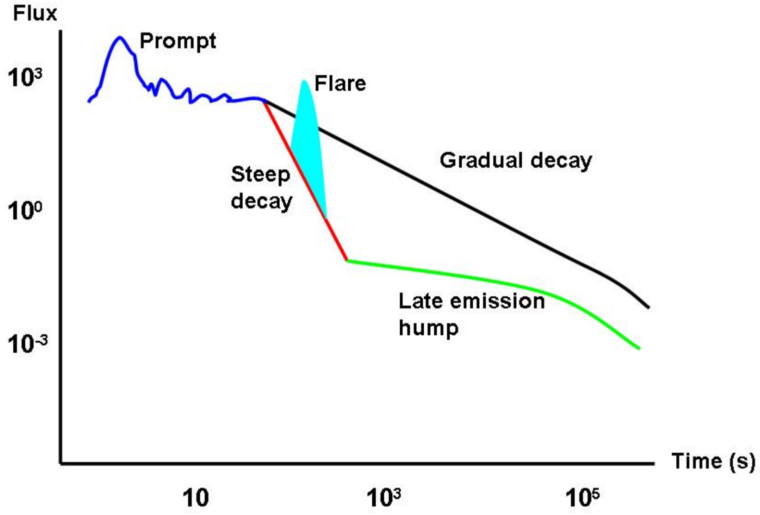

Figure 2.2: A schematic view of the early GRB X-ray light curve. Following the prompt decay, the afterglow typically evolves in one of the two outlined paths, either a step decay followed by a late time bump, or a more gradual decay. Flares can occur in either decay path. The figure is taken from O'Brien & Willingale (2007).

2.3.3 Radiative processes

The two radiative processes which are thought to be important sources of emission during gamma-ray bursts are synchrotron radiation and inverse Compton scattering. These processes determine the form of the continuum observed in the afterglow spectra. The following review is based on the lecture notes of Trulsen (2006).

The Lorentz force, $\mathbf{F_L} = -e\mathbf{v} \times \mathbf{B}$ acting on an electron with charge e and velocity, $\mathbf{v}$, in a magnetic field, $\mathbf{B}$, will give rise to a spiraling orbit of the electron provided that there exists a velocity component perpendicular to the direction of the magnetic field. That means that the electron has an acceleration, and as all accelerated charges it will emit *synchrotron radiation*. Magnetic fields are a common feature in the universe and synchrotron radiation constitutes a common contributor to the total radiation observed. To say more about the nature of synchrotron radiation, it is useful to set up the full formula of the Lorentz force with contributions from both electric and magnetic fields.

$$\frac{d(\gamma m v)}{dt} = m\gamma^2 \frac{\mathbf{v}^2}{\mathbf{r}^2} = \mathbf{F} = q(\mathbf{E} + \mathbf{v} \times \mathbf{B})\,, \tag{2.1}$$

where $\mathbf{r}$ is the radius of the orbit, m is the mass of the charged particle, $\mathbf{F}$ is the force, $\mathbf{E}$ is the electric field, q is the charge and the relativistic acceleration of a circular orbit, $\mathbf{a}$ is

$$\mathbf{a} = \gamma^2 \frac{\mathbf{v}^2}{\mathbf{r}^2} \tag{2.2}$$

and the Lorentz factor is defined as

$$\gamma = \frac{1}{\sqrt{1 - \mathbf{v}^2/c^2}}\,,$$

where c is the speed of light in vacuum. The angular frequency is given by

$$\omega = \frac{2\pi}{T} = \frac{2\pi}{2\pi\mathbf{r}/\mathbf{v}} = \frac{\mathbf{v}}{\mathbf{r}}\,, \tag{2.3}$$

where T is the period, $\mathbf{r}$ is the radius and $\mathbf{v}$ the velocity. The electrons in the plasma will have a broad distribution of kinetic energies. The velocity of the electron determines both the radius of the orbit (Eq.2.2), and hence the angular frequency of the electron – the gyro frequency (Eq.2.3). The gyro frequency is again directly proportional to the radiated frequency spectrum. Therefore, the spread in kinetic energies among the electrons give rise to a corresponding spread in spectral emission lines, resulting in a continuous total synchrotron radiation spectrum. So, from pure synchrotron radiation, we do not expect to see discrete lines. Two other important characteristics of synchrotron radiation are a non-thermal and linearly polarized spectrum. A non-thermal spectrum means that it does not follow Planck's radiation law. The polarization direction is perpendicular to the projection of the magnetic field.

Compton scattering is the decrease in energy of an X-ray or gamma-ray photon, when it interacts with matter (usually a free electron). Consequently, *inverse Compton scattering* is when the photon gains energy in the interaction. This is a free-free process, and, as synchrotron radiation, it contributes to continuum emission. Synchrotron radiation has for a while been believed to be the main mechanism of GRB emission, but it now seems that also inverse Compton scattering may have its role to play in GRBs. For instance the low flux of prompt UV/optical emission, such as in GRB 060218, can be explained by inverse-Compton scattering (Dai et al., 2006) and also analysis of GRB 030227 (Castro-Tirado et al., 2003) and GRB 000926 (Harrison et al., 2001) show evidence for Compton scattering.

2.3.4 Luminosity correlations

When the properties of an observable feature directly or indirectly depend on an objects' luminosity, we have a luminosity correlation. An observation of this property will then infer an estimate of the luminosity, provided that the correlation is accurate and well calibrated. Two objects for which excellent examples of luminosity correlations exist, are supernovae type Ia where the luminosity is closely correlated with the declination rate, and cepheids where luminosity changes with the variability period. Such objects are often called 'standard candles'. This does not mean that all objects within a specific type of standard candle has the same luminosity, supernovae Type Ia can vary with more than four orders of magnitude, it simply means that there are other, implicit ways, to measure luminosity without already knowing the distance. This subsection is largely based on the paper (Schaefer, 2006).

Accurate determination of the distances to GRBs are of great importance if they are to be used as probes of the early universe. When no spectroscopic data are acquired, or the data can not disclose the redshift, distance measurements must depend on luminosity correlations. For GRBs there are at least five luminosity relations which can be used as independent luminosity distance indicators. Not all are of equally good quality, and all of them are not obtained in every GRB dataset, therefore GRBs are not the ideal standard candle. The five observables which correlate with luminosity are listed below. The *Variability* (V) of a burst is a quantitative measure of whether its light curve is spiky or smooth. The *spectral lag* of a GRB is the time difference between the soft and the hard photons. The light curve of photons with energy around $25 - 50$ keV will tend to be delayed relative to those with energy around $100 - 300$ keV. However, only the brightest bursts have their peak times defined well enough to make this a useful definition (Schaefer, 2006). The *minimum rise time* (τ_{RT}) is a measure of how fast the GRB light curve rises. A GRB light curve can vary from being a single simple exponential-decay light curve to one with a dozen complex, spiky bursts. It turns out that the *number of peaks*, N_{peak} also has a correlation with luminosity. In this correlation the challenge is to decide what to count as peaks. The fifth luminosity correlation connects the total collimation-corrected energy in gamma-rays emitted by the burst, E_γ, with the *source frame spectral peak energy*, E_{peak} (Ghirlanda et al., 2004). The opening angle of the jet is derived from the break time observed in the afterglow light curves of the burst. This is the tightest relation for GRBs. For bursts where some, or all, of the above features have been observed, an estimate of the absolute luminosity may be inferred and therefore also the distance. This distance will depend on the spesific cosmology chosen. If a distance measurement is obtained from both the redshift *and* a luminosity correlation, this is enough information to plot the GRB in a Hubble Diagram. This could then provide a test on the cosmological model used.

2.4 The host galaxies

There are (at least) two good reasons to study GRB host galaxies. The first is that they can give information on when and where massive stars were formed throughout the history of the universe. The second is that their properties and the exact localization of the GRB within the host may help us understand the precise nature of the progenitor (Fynbo et al., 2007). As knowledge of the second point is essential to exploit the full potential of GRBs on the first point, I will start with the properties of host galaxies and continue with the localization of GRBs within the host. The road to information on many host galaxy properties such as chemical abundances, dust-to-gas ratio and ionization state, go through the interaction between GRBs and the interstellar material. This interaction is the topic of Section 2.5.

2.4.1 Morphology and metallicity

GRB hosts are not of a single morphological type, they include a broad diversity of galaxy types such as spirals, mergers and ellipticals (Conselice et al., 2005). In spite of this, they have some general characteristics; often they are extremely blue, star-forming galaxies, exhibiting strong emission lines, including most of the Balmer series and Helium lines. Such lines are typical of young, very massive stars. Because of the close connection between supernovae and GRBs, it is natural to assume that the host galaxies of the two must be similar. However, after a closer investigation, this does not seem to be the case (Fruchter et al., 2006). The host galaxies of the Gamma-ray Bursts are significantly fainter, smaller and more irregular than the hosts of the supernovae (Fruchter et al., 1999, 2006). While almost half of a sample of observed SNe lies in grand-design spirals, only one out of eighteen GRB hosts (in the same redshift bin) is a grand-design spiral (Fruchter et al., 2006). In general, the host galaxies of SNe and GRBs, differ both in their intrinsic magnitude and size. The massive progenitor stars are found in galaxies of all sizes, and therefore should not be able to account for the differences in host galaxies. One possible explanation is that the fundamental difference between the LGRB and SN host population lies not in their size or luminosity, but rather in their metallicity or chemical evolution. The small size and low luminosity of the GRB hosts may then be explained as a result of a correlation between galaxy mass and metallicity ($M-Z$ relation); the more massive the galaxy the higher the metal abundance (Fruchter et al., 2006, 1999).

Before proceeding, I must make the point that it is by no means clear how severe this proposed low metallicity bias is, or even whether it really exists. Among the evidence reducing the severity of a metallicity bias is GRB 020127 ($z = 1.9$), where the host has a measured metallicity of approximately $Z = 0.5Z_\odot$ (Berger et al., 2006a). This shows that at least some GRBs occur in massive, metal-enriched galaxies. Also the host galaxies of GRB 000926 (Savaglio et al., 2003) and GRB 980425 (Sollerman et al., 2005) have metallicities well above the theoretical $0.3Z_\odot$ limit for WR stars. This indicates that either there must exist other progenitors (e.g. binaries), or that massive stars with metallicities greater than $0.3Z_\odot$ also can produce GRBs. Fynbo et al. (2007) and references therein draw attention to the existence of progenitor models for long duration GRBs where there is no obvious dependence on metallicity. Hence the role of metallicity is still an open question, but it seems now to be agreement in the community that at least for $z > 2$, a possible metallicity bias will have very little effect because of the lower average metal abundance at higher redshift. This is good news for the star formation-tracer properties of GRBs. In fact, Conselice et al. (2005) argue that GRBs are an effective tracer of star formation and may be the ideal tracers of typical galaxies undergoing star formation at any epoch, making them possibly the best hope of locating the earliest galaxies at $z > 7$, while Fynbo et al. (2006a) conclude that GRBs are 'promising complementary probes of chemical evolution at high redshift'.

Optical studies of $z < 1$ host galaxies show that GRBs occur in galaxies with low luminosities and blue colors relative to field galaxies (Fruchter et al., 1999; Sokolov et al., 2001). For higher redshifts, $z > 1$, we might find a different story, because *relative* to field galaxies, the nature of GRB hosts seem to evolve with redshift. While lower redshift GRB hosts are smaller, less luminous and bluer galaxies, higher redshift hosts are more concentrated and have typical field galaxy sizes (Conselice et al., 2005; Vreeswijk et al., 2005; Fruchter et al., 1999). This is the result of a general evolution of galaxies, while the GRB hosts have remained the same. In the metallicity-biased scenario these observations may be explained as follows: The least luminous galaxies at each redshift interval may become increasingly metal-poor compared to more luminous galaxies ($M_B < -20$) Kobulnicky & Kewley (2004). In other words the difference in metal abundance between galaxies today is probably much larger than at earlier times. Therefore, at high redshift most galaxies are low in metallicity and it does not constitute a real restriction on hosts. At lower redshifts the differences have increased dramatically, excluding the luminous, most metal rich galaxies as GRB hosts.

As an alternative to the metallicity biased selection, it is suggested that the blue colors of GRB hosts may rather reflect their young stellar population, and so cause the selection of young star burst galaxies (Berger et al., 2006a). A star burst galaxy is a galaxy with an exceptionally high rate of star formation. Two very common types of GRB host galaxies, irregulars and Wolf-Rayet galaxies, i.e. galaxies containing a large population of WR stars, are often classified as star burst galaxies. In this star burst galaxy biased scenario, the driving parameter would be stellar population age, not low metallicity.

2.4.2 Localization within the galaxy

The positions of the afterglow in the host galaxies have been regarded as consistent with GRBs being associated with star forming regions containing extremely young, bright and massive stars. This is quite natural since a GRB progenitor needs to be more massive than $18M_{\odot}$ to form a black hole, and probably even more massive than this to produce the observed energies. From this one can draw the conclusion that GRBs trace the light distribution. Supernovae also trace light distribution, and since LGRBs and supernovae are so closely related, this seems like a nice and suitable coincidence in accordance with our expectations. However, by taking a closer look, the picture becomes less clear. While both populations trace the light, GRBs take the light tracing-sport to greater extremes. The location of Gamma-ray Bursts are even more concentrated in the very brightest regions of their hosts than are the supernovae (Fruchter et al., 1999). In fact, they are even more concentrated on the blue light of their hosts than the light itself!

2.5 GRBs and the interstellar medium

The reason why we can have such in depth knowledge about high redshift host galaxies, is the interaction between GRBs and the interstellar medium (ISM). Superimposed on the continuum from the GRB afterglow, the interstellar medium will give rise to spectral lines. The information gained will therefore depend on the properties and chemical content of the ISM.

The ISM consists of an extremely dilute and tenuous (by terrestrial standards) mixture of ions, atoms, molecules, larger dust grains, cosmic rays, and magnetic fields. Although dust produces most of the obscuration that is easily noticeable, it only constitutes about 1% by mass. The remaining 99% is gas, predominantly hydrogen in its various forms; neutral hydrogen (H I), ionized hydrogen, and molecular hydrogen (H_2). Helium comprises about 25% by mass, 10% by number, of the total, while metals account for only a few percent. The helium is primarily a result of the primordial nucleosynthesis, while supernovae are mainly responsible for the metal enrichment (Bradley & Dale, 1996). The interplay between stars and the ISM helps to determine the rate at which a galaxy depletes its gaseous content, and therefore its lifespan of active star formation.

Spectroscopic analysis of GRB afterglows may give column density measurements for ions present in the surrounding ISM. The accuracy of such measurements will depend greatly on the resolution of the spectrum. Density measurements can be used to constrain the physical properties of the ISM, including the metallicity, dust-to-gas ratio, ionization state and chemical abundance of the gas.

GBRs provide a way to probe intervening gas in galaxies and the intergalactic medium (IGM). Another widely used probe of the ISM- and IGM is damped Lyman α systems (DLAs) which lie in the sightline of a quasi stellar object (QSO). Such systems are dubbed QSO-DLAs. However, the detection of these DLA systems depend on the chance alignment of the quasar and DLA gas. The cross section for alignment and the presence of dust may bias the system so that they are not representative samples of the ISM. GRB absorption systems with large abundances of neutral hydrogen are dubbed GRB-DLAs. The limit for DLA systems is a H I column density, N(H I), above 20.3. As we will see later, most GRB systems are GRB-DLAs. GRB-DLA systems have several advantages over QSO-DLA systems; GRBs are located in star-forming galaxies with typical offsets of only a few kpc. They therefore probe the most intense star formation, while for quasar sight lines, the probability of intersecting an individual star-forming cloud is very small. Another advantage is that the host galaxy and any intervening DLA system can be studied directly when the afterglow of the GRB has faded.

2.5.1 Do GRBs origin in molecular clouds?

There are reasons to believe that the clouds of GRBs are molecular; Reichart & Price (2002) argue that when judging from the mass and sizes of the clouds of GRBs with undetected optical afterglows, the clouds must be molecular clouds if they are to be gravitationally stable. Assuming the column density of galactic-like molecular clouds, the number of dark bursts may be comparable with the number of bursts with detectable optical afterglows. As this is what is observed, it may suggest that bursts with optical afterglows also occur in molecular clouds (Reichart & Price, 2002). Alternatively, if one assumes that dark optical afterglows are not an intrinsic property of GRBs, but an observational effect, then the molecular cloud origin of bursts with detectable afterglows follows without further arguments. The hypothesis of GRBs occurring in molecular clouds may be tested by comparing the observed GRB N(H I) distribution with the expected column density distribution for bursts in the galactic-like molecular clouds.

2.5.2 Is the probed ISM affected by the GRB?

Recent comparison of X-ray to optical column density ratios in GRB afterglows suggests that the gas probed by optical afterglow spectra is not the cloud in which the burst occurs (Watson et al., 2007; Vreeswijk et al., 2006a). This means that the optical/UV spectroscopy of GRB afterglows typically probes environments that are little affected by the progenitor. In other words, the metallicity derived from absorption-line spectroscopy, such as in this thesis, may not be representative for the metallicity of the region of the GRB progenitor. However, the result is encouraging with respect to use GRBs as probes of star-formation regions in the early universe. Another advantage is that assumptions regarding ionization conditions applied to DLAs also should be valid for the absorption systems around GRBs. The discussion on ionization in Section 6.6 rests on this assumption.

2.6 GRBs as cosmological probes

GRBs are important for information on a range of different cosmological aspects, one of the most important being the star formation history of the universe (Fynbo et al., 2007). The mere detection of high redshift GRBs give information on the earliest populations of stars and the epoch of ’first light’. If information about metallicity evolution of star-forming regions is to be gained, high resolution spectroscopy must be achieved. Information about the epoch of re-ionization can come from the measurements of overlap in Lyman-α absorption in the afterglow spectra, called the Gunn-Peterson effect (Loeb, 2002). Also GRBs may play a role in the testing of different cosmological models.

2.6.1 The star forming history

At recombination, which occured at redshift $z = 1080$, the universe became transparent. The cosmic background radiation originated at this redshift. The background radiation then started to cool off and when it falls below 3000 K, the universe entered the ’dark ages’. The ’dark ages’ refer to the lack of visible light in the universe. At about $z = 20$, we get the ’first light’, corresponding to the epoch of the first star formation. Their ultraviolet radiation re-ionized the universe, and after this the universe is transparent in the ultraviolet. Accordingly, as GRBs are indirectly related to star formation, they are expected to occur up to at least $z = 10$ and possibly even to $z = 15 - 20$. These redshifts are far larger than what is expected for the most distant QSOs, $z \approx 5$ (Lamb & Reichart, 2000). Swift has already observed GRBs up to $z = 6.29$ (GRB 050904, Cusumano et al., 2006) and it is hoped that redshifts all the way up to $z = 10$ may be observed. A further advantage over quasi-stellar objects (QSOs) is that high redshift GRB afterglows can be hundreds of times brighter than high redshift QSOs. Plenty of light allow high resolution and more details. The fact that some GRBs are related to the collapse of massive stars, leads to the expectation that the rate of such GRBs should be approximately proportional to the *star-formation rate* (SFR). Since GRBs are detectable at very high redshifts and their redshifts may be measured from the absorption-line systems, GRBs may provide unique information about the star-forming history of the very high redshift universe.

To understand what a metallicity bias could mean for the completeness of GRBs as cosmological probes, it is important to know the present mean metallicity, Z, and how it declines with redshift (Fynbo et al., 2006a). Zwaan et al. (2005) find a present day mean metallicity in the gas phase of $Z \sim 0.44 Z_{\odot}$ and a slope between -0.25 and -0.30 dex per unit redshift. This means that at $z \sim 1$ and earlier, the mean metallicity of the gas is below the cut-off value above which single massive stars in the collapsar models do not make GRBs. It is therefore likely that GRBs at $z \gtrsim 2$ will be fairly unbiased tracers of star-formation, while they become increasingly biased at $z < 1$ if there is a low metallicity bias. There exist GRBs with metallicity measures above the cut off value. This indicates that collapsars resulting from single massive stars are not the only progenitors to long GRBs or that massive stars with higher metallicities also can produce long GRBs (Fynbo et al., 2006a).

A method that has been used for tracing star formation is identification of Lyman break galaxies (LBG), which are star forming galaxies. However, only about one third of the UV light from LBGs is emitted by galaxies luminous enough for the ground based LBG survey to be able to detect it (Fynbo et al., 2006a). Using only LBGs to derive the total star-formation density means that an extrapolation to the poorly determined faint end of the luminosity function is unavoidable. Using GRBs, this faint end can be probed, since the selection is not limited by the brightness of the host (Fynbo et al., 2006a; Jakobsson et al., 2005). GRBs allow the measurement of metallicities at very high redshifts $(z > 6)$, which is inaccessible to QSO-DLA. This makes GRBs promising complementary probes of chemical evolution at high redshift.

2.6.2 Hubble diagrams

The *Hubble diagram* is a plot of distance versus redshift, the slope giving the expansion history of our universe. This expansion history depends on the amount of mass in the universe, both normal and dark, as well as on Dark Energy. In the late 1990's, observations of supernovae out to a redshift of near $z = 1$ demonstrated that the universal expansion is now accelerating (Riess et al., 1998). This was the first real evidence for the mysterious energy now dubbed Dark Energy. One of the few ways to measure the properties of the Dark Energy is to extend the Hubble diagram to higher redshifts (Schaefer, 2006). Many models have been proposed that make specific predictions as to the shape of the Hubble diagram, so if there is an 'observed' Hubble diagram to compare with, this offers a way of testing and possibly eliminating models. Supernovae have traditionally been the target of 'Hubble diagram-makers', but to really see the differences between the models, the Hubble diagram must be extended to higher redshifts, were the differences are most pronounced. GRBs are a good candidate for such studies, but as of today their shortcomings as reliable standard candles limit the progress. However, Hubble diagrams using GRBs have been made. Independent measurements of redshift from optical spectroscopy *and* distance measurements from luminosity relations, are sufficient to plot the GRB on a Hubble diagram. In such a diagram the redshift is plotted on the x-axis, while the distance modulus $(M-m)$ is plotted on the y-axis. The distance modulus relates the absolute and apparent magnitudes to the distance by

$$m - M = 5\log d - 5\,,$$

where m is apparent magnitude, M is the absolute magnitude and d is the distance. To use this method to test cosmology models, it is important that the calibration of the luminosity relations is performed for every separate cosmology considered. This is because the luminosity distance, and therefore the distance-axis in the HD diagram, change within different cosmological models. Another concern is whether GRB progenitors have undergone evolution that will affect the luminosity correlation. However, the luminosity indicators are the result of light travel time delays, conservation of energy in the shocked material, and the degree of relativistic beaming Schaefer (2006). These variables are not likely to change with age or metallicity. This means that even though distant bursts might be more luminous on average than nearby bursts, the luminosity indicators will in any case return the correct luminosity.

2.6.3 GRBs as probes of the reionization epoch and the IGM

The time of reionization is one of the most important unknown quantities relevant to the study of large scale structures (Loeb, 2002). GRBs may help resolve this issue; their UV spectra can be used to measure the evolution of the neutral intergalactic hydrogen with redshift. Neutral hydrogen is a very effective absorber at wavelengths shortwards from the Lyα break. Loeb (2002) argues that if a GRB is located at a redshift larger by $> 18\%$ than the reionization redshift, then the Lyα

and the Lyβ troughs will overlap. When neutral hydrogen absorption features overlap and cause complete Lyα absorption, it is called the Gunn-Peterson effect. As GRBs exits at high redshifts they can probe the IGM at $z > 5$ when reionization is believed to have taken place (Barkana R. & Loeb, 2001). The sightlines of GRBs may reveal clustering of the Lyman α lines and the metal absorption-line systems. Such clustering might tell us about the clustering of matter at the largest scales. Similar analysis have been done on QSO sightlines. Detection of metal absorption lines in the spectrum of GRB afterglows, produced either in the inter galactic medium (IGM) or in the host galaxy of the GRB, can also help unravel the evolution of the IGM metallicity with redshift and its link to the evolution of galaxies. Detection of X-ray absorption by intergalactic metals can be used to establish the existence of the warm component of the IGM which has not yet been observed (Loeb, 2002). Other possible ways of using GRBs as cosmological probes include cosmological microlensing of gamma-ray bursts (Loeb, 2002).

Chapter 3

Spectroscopy

In the previous chapter I outlined the great amount of information GRBs may provide us with. A powerful tool with which to extract this information is spectroscopy. In this chapter I describe, theoretically, how spectroscopy unvail the properties of the absorbing medium. The review is largly based on the books (Emerson, 1996) and (Tennyson, 2005) and the lecture notes of (Trulsen, 2006) and (Petitjean, 1998).

In short, spectroscopy is the study of the spectrum of electromagnetic radiation, including visible light. It can be used to derive a well of properties of distant stars and galaxies, such as their relative motion - via Doppler shifts, their distance - via redshifts, temperature, pressure and magnetic fields and chemical composition. These parameters may in turn give away age, history and information about ongoing dynamical processes. It is important to note that the information we gain is not just about the source of the radiation itself, equally valuable is the imprint set on the radiation by the surrounding and intervening medium. By describing the physics on atomic and subatomic level, quantum mechanics enables us to understand the particular shape of a spectrum. Although we have come a long way with recognizing the different mechanisms and their effects, many are so marginal that they are hard to actually observe. In general we can divide radiation processes into three broad categories; bound-bound transitions, bound-free/free-bound transitions and free-free transitions. It is the bound-bound transitions which lead to the formation of emission/absorption lines in the spectra, and thus the transitions we use when measuring abundances from lines in an electromagnetic spectrum. Simply knowing at which wavelengths we have the different transitions enables us - in theory - to find how many such transitions are needed to produce the observed feature, and, knowing the probability for each transition, calculate the amount of such atoms. Unfortunately, there are a few minor details, such as lower order quantum mechanical effects, changes occurring during radiative transport, and, maybe most importantly, telescope limitations, which make things a tiny bit more complicated. Bound-free transitions, and free-free transitions, where the electron involved in the transition is free, either before and/or after the collision, are responsible for the continuum spectra. Synchrotron radiation is an example of free-free transition where the electron is in a free state both before and after the event. I have already mentioned that the radiation processes usually linked to GRBs are synchrotron radiation and inverse Compton scattering. The following sections will keep a broader view, linking the radiation and radiation transport to the actual, observed spectrum.

3.1 Line profiles

Typical spectra have a continuum sprinkled with emission- and absorption lines. Each line has a *line profile*. The shape and depth/height of the line profile is the combined result of the probability of a specific transition, the number of atoms available in the 'right' state and modifications due to radiation transport. The probability and number of atoms are proportional to- and conveniently described by the *absorption/emission coefficient*. Several processes contribute to broadening of the spectral lines, causing the observed absorption or emission line features in the spectra to have finite widths. The three most important types of line broadening are *natural line broadening*, which is always present, *collisional or pressure line broadening*, due to collisions with other particles and *Doppler line broadening*, due to the motion of the observed atoms.

Any excited state in an atom or molecule has a natural lifetime. The length of the lifetime depends on transition rates to allowed lower states. In accordance with Heisenberg's uncertainty principle the energy uncertainty increases inversely proportional to the natural lifetime of the excited state. In other words, an excited state with a very short lifetime, will have a large spread in energy and hence give rise to a correspondingly broadened line. The longer the lifetime, the narrower the line profile. This is natural line broadening. The shape of the natural line profile is said to be Lorentzian. It has a full width at half maximum $\delta\omega_{\mathrm{FWHM}} = \frac{1}{\tau_i} + \frac{1}{\tau_f}$, where τ_i is the lifetime of the initial state, and τ_f is the lifetime of the final state. Collisions between atoms in a gas will lead to a further broadening of spectral lines, but the line profile will remain Lorentzian. This process is called *Collisional or pressure broadening*. The collision frequency ν_i increases with increasing pressure of the gas. Collisional broadening will normally dominate over the natural line width, in fact the natural line will actually only be observed for gases with vanishing pressure. Relative motion between the atoms in an emitting or absorbing medium gives rise to what is called *Doppler broadening*. It is important to distinguish between Doppler broadening and Doppler shift. Whereas Doppler shift is due to collective radial motion of the medium relative to an observer and causes the whole line to shift to a different wavelength, Doppler broadening is relative motion between the atoms in the medium, i.e turbulence. The corresponding line profile is referred to as a Doppler line profile. The spectral line profile will in this case take a Gaussian shape (assuming a Gaussian velocity distribution) with relatively broad on the middle with narrow wings. The full width at half maximum, $\Delta\omega_{FWHM}$ is given by

$$\frac{\Delta\omega_{FWHM}}{\omega_0} = \sqrt{\frac{8\ln 2\mathcal{T}}{Mc^2}}\,,$$

where ω_{FWHM} is the width of the line at half height measured in frequency, ω_0 is the center of the line, M is the atomic mass and $\mathcal{T}$ is the kinetic temperature in energy units $\mathcal{T} = kT$. The Doppler width is proportional to the rest wavelength and inversely proportional to the square root of the mass of the atom concerned. It is therefore much greater for a hydrogen atom than for example an iron atom. The overall line profile always contains both Doppler and collisional/natural line broadening components, with the Doppler component dominating near the line center and the collisional component dominating the wings of the line. For both components to be taken into account, a convolution of the Gaussian and Lorentzian forms is required. The convolved profile is called a Voigt profile. Line profiles are regularly used to infer density and temperature of the emitting or absorbing medium, temperature mainly from the central core of the line, density from the wings. I will come back to this in Section 3.2.

The formation of the line does not alone produce its final shape. During transport, between the source and the observer, the radiation may experience great changes. It will move through the interstellar and intergalactic medium, and may be altered by absorption and emission from the intervening gas. Also ours means and tools of observation will be of great importance for what we eventually can see.

3.2 Column densities and equivalent width

The simplest measure of the width of a line is the equivalent width, W. The equivalent width is the width of a rectangle centered on a spectral line that, on a plot of intensity against wavelength, has the same area as the line. When looking at the relationship between column density and equivalent width, the optical depth is important. *Optical depth*, τ is defined as the integral of the *absorption coefficient* with respect to distance along a particular line of sight. If we increase the number of atoms in the line of sight through the cloud, the line strength will at first increase in proportion to the number of atoms along the line-of-sight, but as the optical depth through the cloud increases some of the emission will be absorbed before it can escape from the cloud. The line strength will then no longer increase proportionally with the number of atoms along the line-of-sight. Eventually, increasing emission will be balanced by increasing absorption, the line strength will cease to grow, and we say that the line is optically thick. Whether a medium is optically thin or thick vary at different wavelengths. The probability of a photon to be absorbed will depend on its wavelength, since different wavelengths will take part in different interactions. For highly probable interactions, the medium will quickly become optically thick, while other parts of the spectrum will stay completely optically thin. By definition, optically thin media have $\tau < 1$ and optically thick media have $\tau > 1$. In a cloud with $\tau_\lambda = 1$, the average free path a photon (with wavelength, λ) travell before it is absorbed is exactly the length of the cloud. So for $\tau < 1$ it has a lower probability to be absorbed, and therefore a higher probability to escape from the cloud. For calculations it is convenient to use the extremes highly optically thin, $\tau \ll 1$, or highly optically thick, $\tau \gg 1$, thereby avoiding the limiting cases whenever this is a reasonable approximation.

A plot of $\log(W/\lambda)$ versus $\log(Nf\lambda)$ is called a *curve of growth*, often abbrivated COG. A curve of growth will be linear for very weak, or optically thin, lines. For medium strong lines, the curve bends over into a horisontal branch before rising slowly for the very strong lines on the *damping* part of the curve, see Figure 3.1. The curve of growth is therefore a convenient way to illustrate the interplay of optical depth, column densities and equivalent widths. Most importantly it provides the possibility for all lines of a given ion to contribute to determining the abundances.

The Doppler parameter, b, is an important term in this context. It refers to both collisional broadening and turbulence broadening. In the optically thin case shown in Figure 3.1, the total area of the absorption line is equal, regardless of the value of the b-parameter. The larger b-value gives a broader line, but the lower b-value gives a deeper line. This corresponds to the highly optical thin – or unsaturated – case, ($\tau_o < 0.1$). The equivalent width does then not depend on the Doppler parameter, b. The optically thin regime is referred to as the linear part of the curve of growth where the determination of the column density, N, from the equivalent width, W, is easy and reliable. For any transition, Petitjean (1998)

$$N(\mathrm{cm}^{-2}) = 1.13 \cdot 10^{20} \frac{W_r(\text{Å})}{\lambda^2(\text{Å}) f} \, . \tag{3.1}$$

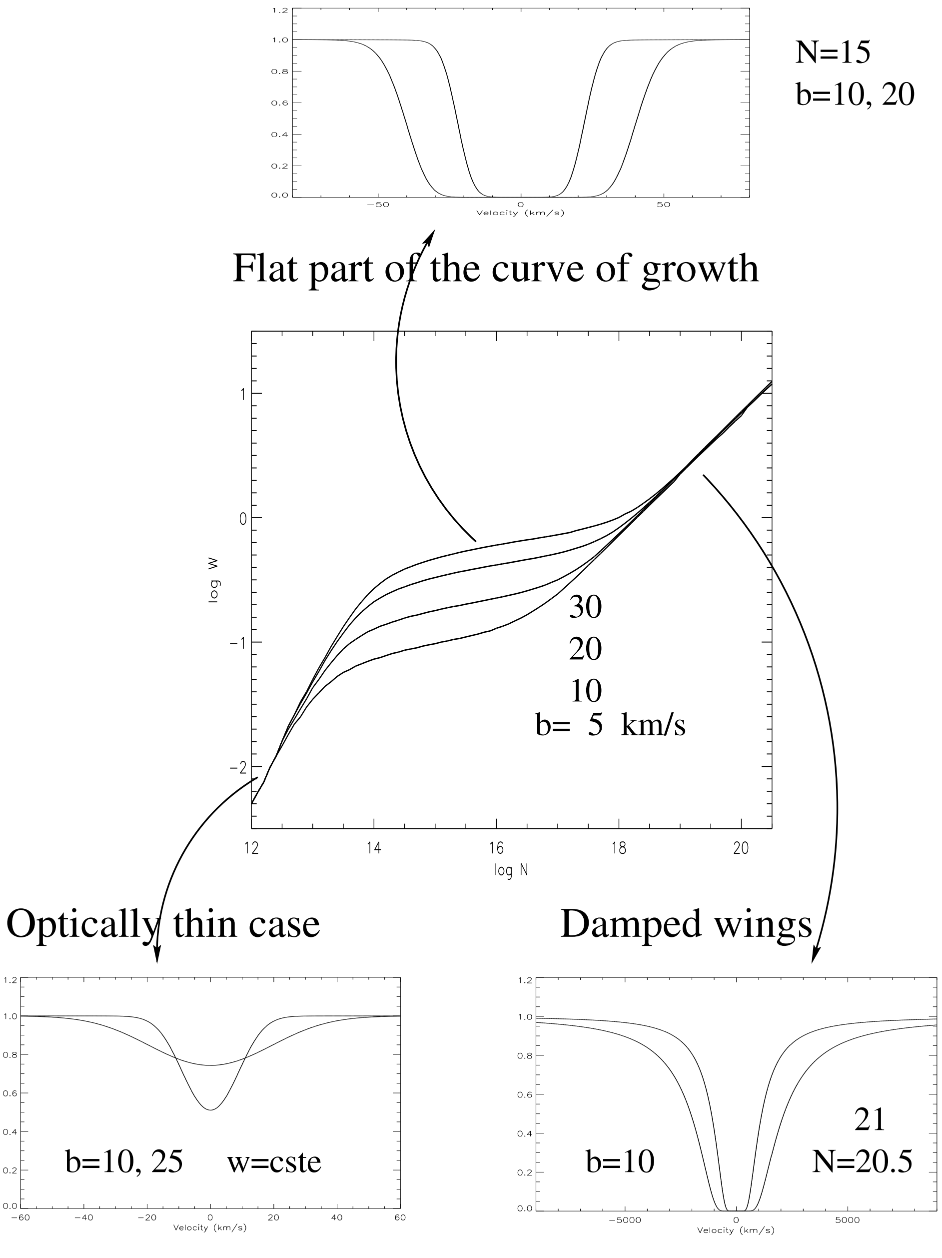

Figure 3.1: This is an illustration of the three different regimes of the curve of growth, representing the connection between column density and equivalent width. The figure is taken from Petitjean (1998). Note that the velocity scale in the three different regimes are not the same.

The oscillator strength f is a measure of the likelihood of a specific transition.

In the flat part of the curve of growth, Figure 3.1, the larger b-value leads to a larger area of the absorption line. The flat bottom of the line means that it is optically thick – or saturated, i.e. the number of ions is no longer directly proportional to the equivalent width. This means that the logarithmic or flat-part (since the scaling is logarithmic) of the curve of growth is characterized by the large dependence of N on b. Thermal broadening and turbulence will therefore greatly affect the equivalent width of lines in this regime. The effects of Doppler -and collisional broadening exceed the saturation effects, meaning that the saturation is evident in the bottom of the line, but the wings are still mainly formed by the turbulence and collisional conditions in the cloud. Therefore, calculating column densities from lines in this regime is unreliable. The relation is

$$\frac{W}{\lambda_0} = 2\frac{b}{c}\sqrt{\ln(\tau_0)}\,, \tag{3.2}$$

where c is the speed of light, b is the Doppler parameter, λ_0 is the central wavelength of the transition, and τ_0 is the optical depth at the center of the line given by (Petitjean, 1998)

$$\tau_0 = 1.497 \cdot 10^{-15} \frac{N(\mathrm{cm}^{-2}) f \lambda_0(\text{Å})}{b(\mathrm{km/s})}\,. \tag{3.3}$$

The absorption lines in the very heavily saturated part of the curve of growth typically have prominent damped wings. The equivalent width does not depend on the Doppler parameter, b, because the line broadening due to b are typically much less than the saturation effects for $\log N > 20.3$ (the damping limit). Therefore the column density can be accurately determined from fitting of the wings of such highly saturated lines. It is worth noting that even though the damping limit is set at $\log N > 20.3$, this is a constructed limit, and the column density may be precisely determined also for ions with column densities slightly less than this limit.

An alternative way of obtaining column densities is by fitting the absorption lines. For high resolution spectra this is the preferred procedure as the results are more accurate and velocity components may be resolved. For intermediate resolution data, the fitting procedure may also be applied but velocity components are in general not resolved. Section 5.3.1 describe absorption line fitting in more detail. Similarly the curve of growth analysis has many pitfalls, which will be discussed in 5.4. In Section 5, both fitting and COG analysis are used to derive abundances for GRB 060526.

Chapter 4

Observations and data reductions

This chapter will present the data of GRB 060526 used for this thesis. A few words will also be said about the satellite which has given gamma-ray burst observations a great lift, namely Swift, and the telescope where the spectroscopic data was taken, VLT. Preprocessing, carried out in IRAF, is the theme for the rest of the chapter. The reader will be guided through the reduction steps from cosmic cleaning to combination of the frames. I focus on the processes, what they do and why they are needed, rather than on the specific IRAF tasks.

4.1 Spectroscopic data of GRB 060526

GRB 060526 is a long-duration burst detected by the Swift satellite and localized by the Burst Alert Telescope on May 26th, 2006 at 16:28:30 UT. The position was refined by the X-Ray Telescope and a subsequent optical afterglow (OA) was detected (Campana et al., 2006a). The FORS1 instrument on the Very Large Telescope (VLT) was used to obtain OA spectra (Jakobsson et al., 2006). The images are obtained through the ESO program ID 077.D-0661(C) of Paul Vreeswijk and given to us by the DARK cosmology center in Copenhagen. The first spectrum is taken with grism 300V, obtained on May 27th at 01:17 which is 8 hours, 49 minutes after the onset of the burst. The last frame is taken at 04:04 the same night; this means that in all frames it is the afterglow spectra that is observed. The prompt emission had faded and the host galaxy was much weaker than the afterglow. In order to improve the S/N, the datasets taken with the same grism are combined. The slit width used was $1\farcs0$. A summary of the spectroscopic observations are given in Table 4.5.

Table 4.1: **Spectra of GRB 060526 from FORS1/VLT**

time May 27(UT), 2006	exp. time (s)	grism	spectral range (Å)	S/N	resolution (Å)
01:17:04	600	300V	3650 - 8900	27	11.1
01:29:46	900	600I	7000 - 9200	16	4.4
01:47:28	900	1200B	3860 - 4400	13	2.4
02:05:35	900	600V	4080 - 7200	20	4.5
02:24:00	1200	300V	3650 - 8900	36	11.1
02:57:05	1800	1200B	3860 - 4400	20	2.4
03:30:41	1800	600V	4080 - 7200	30	4.5
04:04:08	1800	600I	7000 - 9200	21	4.4

4.1.1 Signal-to-Noise

The standard equation giving the signal-to-noise (S/N) of a measurement made with a CCD is often called the 'CCD equation' and is given by

$$\frac{S}{N} = \frac{N_*}{\sqrt{N_* + n_{pix}(N_S + N_D + N_R^2)}}, \tag{4.1}$$

where N_* is the total number of photons collected from the object of interest. The denominator is the 'noise term', n_{pix} being the total number of pixels under consideration for the S/N calculation, N_S the total number of photons per pixel from the background, N_D the total number of dark current electrons per pixel and N_R^2 the total number of electrons per pixel resolution from the read noise. [1] From the equation we can see that if the total noise is dominated by the noise contribution from the source itself, the CCD equation becomes

$$\frac{S}{N} = \frac{N_*}{\sqrt{N_*}} = \sqrt{N_*}. \tag{4.2}$$

This simplified equation is used to produce the S/N in Table 4.5. It is calculated from a single pixel around the central wavelength of the grism. The total number of counts is found by

$$total\, counts = FWHM \cdot peak \cdot gain \tag{4.3}$$

---

[1] As this noise source is not a Poisson noise source, but a shot noise it enters into the noise calculation as the value itself, not the square root of the value as Poisson noise sources do.

where FWHM is the full width half max of the Gaussian profile and the gain is a conversion factor between analog-to-digital unit (ADU) and electrons, which for FORS1 is 1.4. The S/N is improved by combining the spectra taken in the same grism. Adding the total counts by

$$\frac{S}{N}_{total} = \sqrt{N_{*1} + N_{*2}}\,, \tag{4.4}$$

gives a S/N of 45 for the 300V grism, 36 for the 600V grism, 26 for the 600I grism and 24 for the 1200B grism. The signal-to-noise of these spectra may also be evaluated by looking at the combined signal-to-noise spectra which are output from the task `comb1Dspec` in IRAF. The central signal-to-noise ratios resulting form this course are ~ 30 for 300V, ~ 25 for 600V, ~ 18 for the 600I grism and ~ 15 for 1200B. So, we see that these are in general lower than the values stated above. We assume that the reason for this is that the assumption made in the calculation, that the dominant noise contribution is from the source itself, may not be a good approximation for these data. The difference will, however, not have any practical implications here.

4.2 Previous studies of GRB 060526

There are two papers treating observational data of GRB 060526; Dai et al. (2006) have studied the light curve of the GRB, Thöne et al.,(2007) in prep. have analyzed both photometric and spectroscopic data. The evolution of the afterglows, both optical and X-ray, of GRB 060526 show rich features, such as flares and breaks (Dai et al., 2006). They claim a possible achromatic jet break in the optical and X-ray afterglow light curves at $T \sim 2.4 \cdot 10^5$ seconds. Achromatic breaks in the optical afterglow are usually interpreted as the jet break. If the breaks were found at the same time in other wavelengths, this is considered as support of the beaming model of the GRBs. This is because achromatic breaks are most easily explained by a jet (Dai et al., 2006). A jet angle of $\theta \sim 7^\circ$ and a prompt emission size of $R_{promt} = 2 \cdot 10^{14}$ cm is also estimated. Thöne et al.,(2007) have combined their photometric data with that of Dai et al. (2006) to obtain well sampled light curves, particularly in the VBR bands. The light curve is best fit as a broken power-law with break time at $t = 2.55$ days. Thöne et al.,(2007) also find that the host galaxy itself cannot be detected down to limits of $R > 26.3$.

4.3 Swift and VLT

The information on VLT and Swift in this section is mainly collected from their respective homepages on the internet, the ESO Paranal homepage and the official

NASA Swift homepage.

VLT

The VLT consists of a cluster of four 8.2 meter telescopes operated by the European Southern Observatory. They are located at the Paranal Observatory on Cerro Paranal, a $2,635$ m high mountain in the Atacama desert in northern Chile where the observing conditions are among the best in the world. Even though the telescopes can work together as a single large coherent interferometric instrument (the VLT Interferometer), the principal role of the VLT telescopes is to operate as four independent telescopes. The VLTs are equipped with a large set of instruments permitting observations to be performed from the near-UV to the mid-IR with a range of techniques including high-resolution spectroscopy, multi-object spectroscopy, imaging, and high-resolution imaging. In particular, the VLT has several adaptive optics systems, which at infrared wavelengths correct for the effects of the atmospheric turbulence, providing diffraction limited images. For the images of GRB 060526 used in this thesis, the telescope Kueyen (meaning moon in the Mapuche language) was used with its FORS1 (FOcal Reducer and low dispersion Spectrograph) mounted. FORS1 is a visible light camera and Multi Object Spectrograph with a 6.8 arcminute field of view. It is a multi mode optical instrument mounted on a Cassegrain focus and works in the wavelength range $330 - 1100$ nm. The different modes include both imaging modes and spectroscopic modes such as MOS - movable slits and longslit spectroscopy, LS. The LS mode is used for the GRB images, while the MOS mode is used for the standard star in the images reduced in this thesis.

Swift

The Swift telescope comprises three instruments which work together to provide rapid identification and multi wavelength follow-up of GRBs and their afterglows. Swift is part of NASA’s medium explorer (MIDEX) program and since its launch into a low-Earth orbit on November 20, 2004, Swift has contributed greatly to the progress of Gamma-ray Burst studies. It detects roughly two GRBs per week and transmits their accurate positions for rapid follow-up observations. Unlike most NASA satellites, Swift is actually not an acronym, but the name of a bird which can change angles very quickly in mid-flight. The three co-aligned instruments on Swift are the Burst Alert Telescope (BAT), the X-ray Telescope (XRT), and the Ultraviolet/Optical Telescope (UVOT). The largest instrument on-board Swift is the BAT, which can view approximately a sixth of the entire sky at one time. Within seconds of detecting a burst, the spacecraft will rapidly repoint itself to aim the XRT and UVOT at the burst to enable high-precision X-ray and optical positions and spectra to be determined. The positions will then be relayed to the ground for use by a network of observers at other telescopes.

At the very beginning of this thesis, we had a look at the accuracy of the BAT error circles compared to the refined XRT positions, see Figure 4.1. As I found no available tables in a useful format over BAT position and XRT position, I first made such a table, using data from the Swift homepage. This table was then plotted (BAT position - XRT position) and a circle the size of a typical BAT error circle, 5 arcmin, was over-plotted. As can be seen, the BAT error circle is a conservative error estimate. Of the 25 plotted GRBs, only one XRT position is not in accordance with the BAT position. Most points are in the inner part of the circle, indicating a smaller discrepancy between BAT and XRT positions.

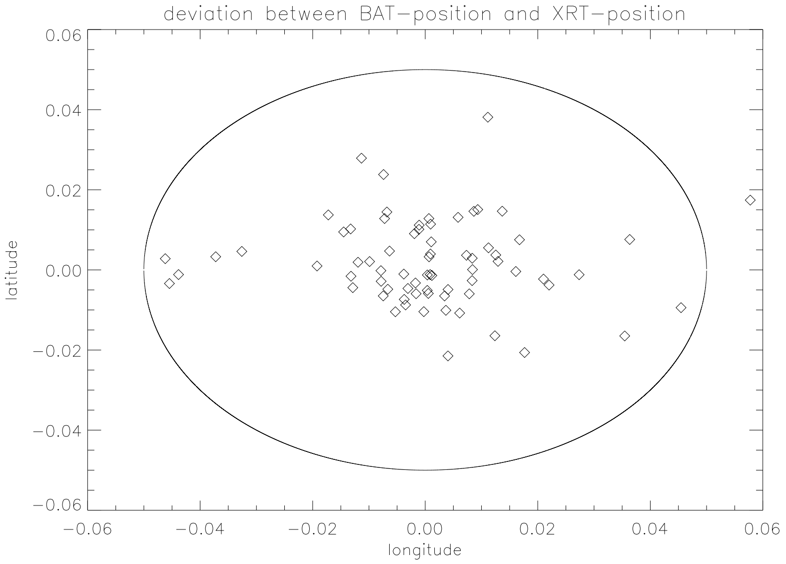

Figure 4.1: A plot of relative positions of the BAT error circle and the refined XRT position of gamma-ray bursts. Data points are taken from the swift home page.

4.4 Data reductions

The data we get when observing is raw material. Therefore, in order to recover as much of the true signal in the CCD image as possible, the data are preprocessed. Background- and instrumental noise are removed through a series of reduction steps from cleaning of cosmic rays to bias-subtraction, overscan-subtraction and flat-fielding. Then comes the exciting extraction of the spectra, identification of lines for wavelength calibration, flux calibration and finally combination of the spectra. In the following I will go through each of these steps and why they are necessary in order to get a beautifully clean and information-rich picture in the end. For the reduction of the spectroscopic frames of GRB 060526, a script called *forslongslit* written by Paul Vreeswijk is used. It is a script written especially for reduction of spectroscopic images from FORS1 and FORS2 at the Very Large Telescope (VLT) at Paranal, Chile. A detailed description of this script can be found in Appendix A.

4.4.1 CCD detectors

Since their first application within astronomy as optical detectors in the 1970s, the CCDs (Charged-Coupled Devices) have dominated completely. This popularity arises from their large dynamic range and high quantum efficiency. The basic detection mechanism is related to the photo-electric effect; the essential part of a CCD is the array of small light-sensitive pixels, which accumulates electric charge when exposed to light. The pixels are made up of silicon, where the photo-electric effect takes place in the wavelength range near IR - soft X-ray, and outside these limits the CCD appears transparent to incoming photons. The electrons knocked loose by radiation are trapped in potential wells produced by numerous small electrodes. There they accumulate until their total number is read out of the array, row by row. CCD values are initially in ADU (Analogue Digital Units), which is related to the number of detected electrons by the gain of the CCD detector. The quantum efficiency (QE) of the CCD is a measure of photon-loss and is defined as the ratio of the number of detected photons to the number of incident photons at a particular frequency.

4.4.2 About IRAF/PyRAF

For reductions I have mainly used the Python version (PyRAF) of the Image Reduction and Analysis Facility (IRAF). This is a general-purpose astronomical image processing system, developed by the National Optical Astronomy Observatories in Tucson, Arizona. IRAF/PyRAF consists of various specialized software-packages which have been developed at different locations.

The image header

The image header file is a combination of ASCII text and binary information about the image: data type, size, times of creation/modification and so on. In the case of the GRB data I have reduced, the header file also contains very useful information about the configuration in place for each and every frame. It is easy to find grism, exposure time, number of pictures in one series, image type and much more directly from the image header.

Scripts

This is a programming environment in PyRAF which can be very useful when processing or modifying a large number of frames. A script is a text file consisting of a sequence of PyRAF commands. Scripts are executed by typing cl < scriptname. For example I use the script `trim.cl` to cut of the top and bottom of all bias-subtracted frames before they are flat-fielded. The most important script for these reductions is `forslongslit`, which utilizes various standard tasks in PyRAF.

4.4.3 Preprocessing with PyRAF

Cosmic cleaning

As the name suggests, this is a procedure to clean the science frames of pixels affected by cosmic ray incidents. The calibration frames do not need to go through this procedure as cosmic rays are effectively cleaned when combining the frames to master frames. In this thesis, the script LA-COSMICS by van Dokkum (2001), is used to remove cosmics. As input, only the spectrum is needed, as output the cleaned spectrum and a bad pixel map are obtained. The script rejects the brightest pixels which are not part of an extended object. The program is based on a variation of Laplacian edge detection. The algorithm identifies cosmic rays of arbitrary shapes and sizes by the sharpness of their edges and discriminates between poorly sampled point sources and cosmic rays. Optional variables enable the user to change both the standard deviation and the number of iterations.

Overscan section and bias frames

Bias- or zero frames are images with zero exposure time. The frame is subtract these from the science frames to get rid of the artificially induced electronic offset. The Analog-to-Digital Converter (ADC) cannot handle negative values, so this offset is there to ensure that the ADC always receives a positive signal. All CCD data have such an offset which must be removed if the data values are to be truly representative of the counts recorded per pixel. This bias level will vary slightly from frame to frame, which means that it has to be individually determined and corrected for each frame. For this purpose we have the overscan-region; a few unexposed columns or lines. The bias level is removed by subtracting the mean pixel value of the overscan strip section of the image. In most cases the bias

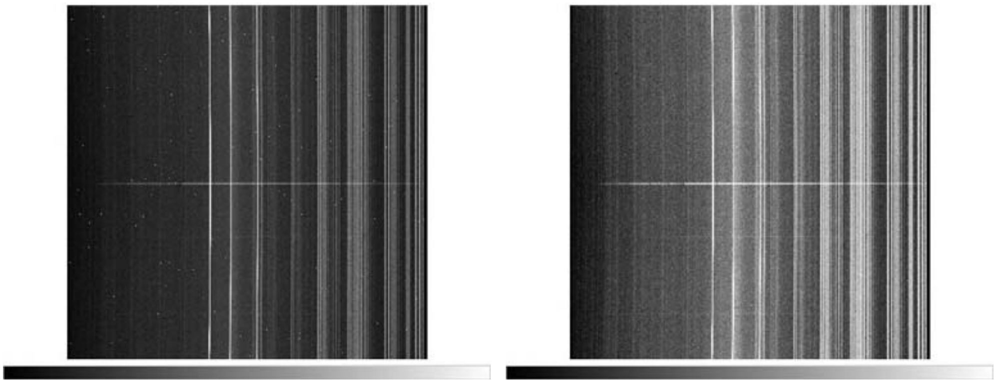

(a) The original frame, 600s in grism 300V, without cosmics removed.

(b) The frame, 600s in 300V, after cosmics are removed.

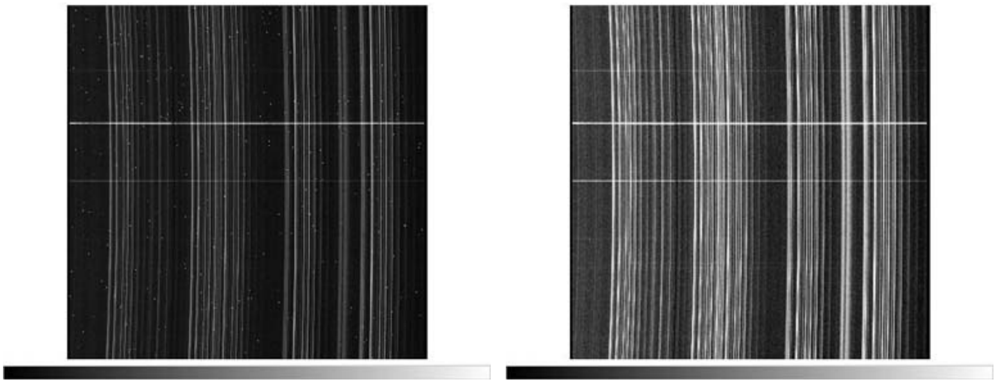

(c) The original frame, 1800s in grism 600I, without cosmics removed.

(d) The frame, 1800s in grism 600I, after cosmics are removed.

Figure 4.2: This figure illustrates the effect of removing cosmics. Both images become more grey after the removal because the variation in brightness is reduced and smaller intrinsic variations therefore give larger effect on the grey scale. Note how little signal there is from the GRB in the 600I frame. The GRB is located in the middle of the picture - it is not the brighter horizontal line in the upper half.

level also varies over the frame, and a so-called bias frame should be subtracted to remove any significant pattern which is common for all frames. This bias frame is usually a master bias, meaning that it is created from the average of a number of individual bias frames. You can say that the overscan-region corrects for time-variations in the bias level, while the bias frames correct for spatial-variations.

Also note that if the master bias reveals no significant pattern there is no need to subtract it, as more noise is induces in the science frames. During the preprocessing of the frames from GRB 060526, both bias frames and the overscan-region were used.

Dark current

The 'dark current' is a signal added to the background in long exposure frames and is due to thermally created electrons. The amount of dark current is directly proportional to exposure time. Since the dark current is negligible for FORS1 and FORS2, no dark frame subtraction is necessary for these instruments.

Trimming

Trimming means that you cut away the parts of your frame that are not useful. In spectroscopy this can be in both the x-axis and the y-axis. At the start of the x-axis you have the overscan region, which does not include any useful data. It can therefore be cut away after the overscan is done. In spectroscopy other objects on the slit may sometimes cause problems during reductions, it can therefore be smart to cut the frames in the y-direction as well. See for instance Figure 4.2(d) were the strongest signal (horizontal) is not from the GRB. To avoid problems with the optimally extraction used in *forslongslit*, this unwanted signal is trimmed away. To have any effect, this must be done before extracting the spectra.

Flatfielding

A flat-field image is used in calibration to correct for the slight variations in gain and QE value of each pixel in the CCD. To flatten the pixels' relative response to the incoming light, the science frames are divided by a flat-field frame. The ideal flat-field image would be an exposure with uniform illumination of every pixel in order to map the internal variations in sensitivity between the pixels. Usually a lamp shining on the inside of the dome or the twilight sky is used as light source for flat-field images. When using the dome as a screen to take *dome flats*, it is difficult to obtain uniform illumination. This is why many astronomers prefer taking exposures during twilight in the evening or in the morning to obtain *sky flats*. On the other hand, a problem with sky flats would arise if bright stars were visible in the image. This problem is solved by dithering between each exposure and using the median rather than the average of each pixel. For both methods, five to ten flats from each filter should be obtained in order to get the master flat-field image of the quality required for proper image reduction. Each filter should have its own flat-fields, since the pixel response to incoming light is wavelength dependent. The process will also efficiently remove possible dust specks present on the filter. The dust specs are visible as darker "doughnuts", as they are not on the CCD surface and therefore out of focus. These dust particles cast a shadow on the CCD and therefore effectively lower the CCD sensitivity at those points.

Extraction

To actually obtain the spectra, Figure 4.5, the aperture must be identified, defined, traced and extracted from the two dimensional CCD image. Typically the IRAF-task `apall` is used to carry out the extraction. This is a collection of individual tasks which each handle one separate step. In the identification procedure the aperture belonging to the object of interest is picked. In the simplest possible case, this would be one single row (or column, whichever is perpendicular to the dispersion axis). More realistically, the spectrum is smeared out over a few rows and these rows need to be summed up at each point along the dispersion. Often the CCD spectra are not precisely aligned with the CCD pixels. This will lead the spectrum to curve slightly over the CCD and therefore it will not follow the same ’central row’ along the dispersion. In `apall` one can interactively identify and fit (’trace’) this curvature and thereby account for it in the extracted spectrum. A sample of the background is also made, so that this may be subtracted from the extracted spectrum. After defining which pixels come from the object of interest, these are plotted in a new one-dimensional picture and we have the extracted spectrum. The brightness of the spectrum, at this point usually measured in pixels/ADU, is plotted along the y-axis and the pixels along the x-axis. The conversion of each of these axes into absolute flux and wavelength, respectively, is the subject for the next two subsections.

Wavelength calibration

Since all GRBs are distant and usually in motion relative to us, the wavelengths are not located at their ’normal’ positions. However, the wavelength range of the grisms used are known, and luckily the spectral signature is often so unique that some features will be recognizable. This will then enable us to find the redshift of the observed spectra (recall the relation between wavelength and redshift, Section 2.1). To achieve accurate results with this method, we must know exactly what wavelengths we are observing. The essence of wavelength calibration is therefore to assign a wavelength to each pixel. This is done by using arclamps giving emission lines with known wavelengths. The science frame is then wavelength calibrated by applying the pixel-wavelength solution found with arclamps. PyRAF also helps you along the way by fitting the assigned wavelengths to the spectra and displaying the goodness of the fit. The root mean square (rms) should preferably be below 0.1 in the final calibration. For FORS1 and FORS2 the emission lines for calibration in each grism can be found in the manual. If there are no such calibration frames available, they can be taken in the telescope during daytime (not to waste valuable night time). Even with a good fit, it is a good idea to check that

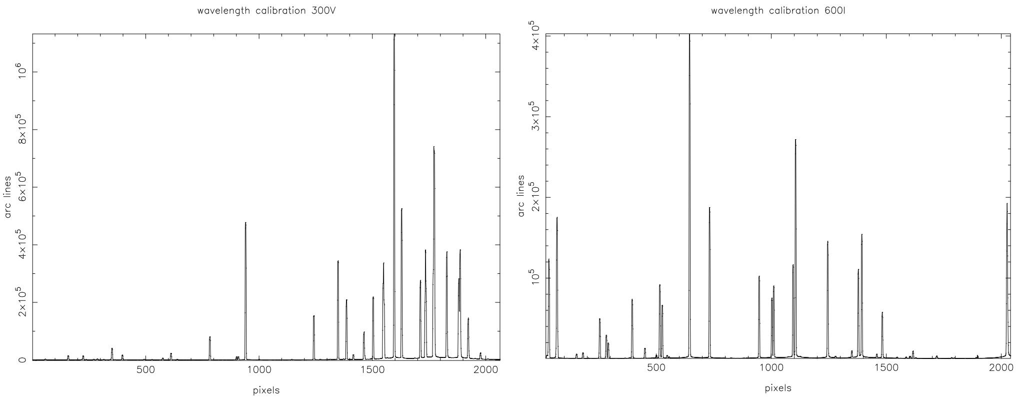

(a) Grism 300V

(b) Grism 600I

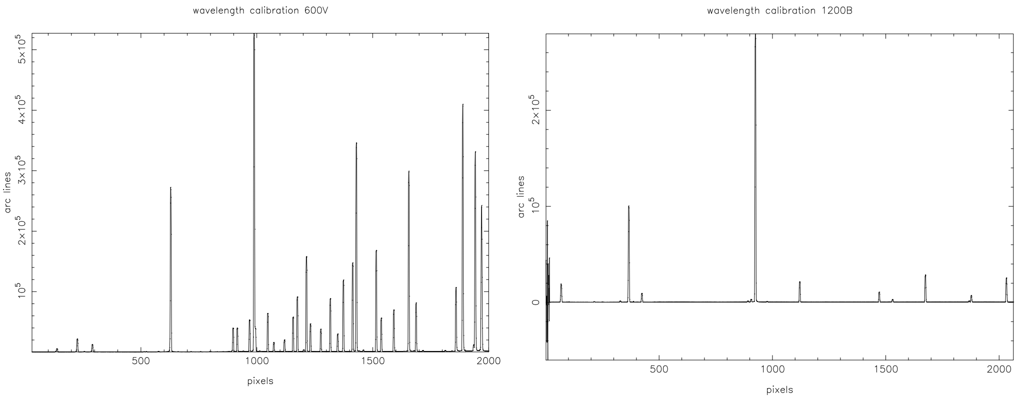

(c) Grism 600V

(d) Grism 1200B

Figure 4.3: Arclines used as reference spectra for wavelength calibration of the spectra in four different grisms.

one's wavelength calibration is correct, or to what extent it is correct. One way of doing this is to look at the wavelength of the skylines in the background part of the mulitispec frame PyRAF gives you. The skylines should be at the same, well known wavelengths, as they originate in the atmosphere and therefore are not shifted. With the use of all available skylines in each grism, we get the results displayed in Tables 4.2, 4.3, and 4.4. As none of the wavelengths from the list are

Table 4.2: **Grism 600I**

skyline air	measured vacuum	measured air	difference
7276.4243	7278.75	7276.63	0.21
7750.6562	7753.13	7750.88	0.22
7913.7178	7916.28	7913.98	0.26
8344.6133	8347.27	8344.85	0.24
8827.1123	8829.72	8827.16	0.05

Table 4.3: **Grism 600V**

skyline air	measured vacuum	measured air	difference
5197.9282	5201.50	5199.99	2.06
5577.3467	5579.37	5577.75	0.40
5889.9590	5891.60	5889.89	-0.07
6300.3086	6302.20	6300.37	0.06
6363.7827	6365.93	6364.08	0.03

Table 4.4: **Grism 300V**

skyline air	measured line vacuum	measured line air	difference
5197.9282	5200.47	5198.96	1.03
5577.3467	5579.62	5578.00	0.65
5889.9590	5893.90	5892.19	2.23
6300.3086	6302.73	6300.90	0.59
6363.7827	6365.82	6363.97	0.19
7276.4243	7279.35	7277.24	0.82
7750.6562	7753.49	7751.24	0.58
7913.7178	7916.52	7914.22	0.05
8344.6133	8347.36	8344.94	0.33
8827.1123	8831.55	8828.99	1.88

included in the wavelength range of grism 1200B, no check has been performed on that grism. All given skylines are listed in air, but during calibration in PyRAF vacuum wavelengths were used, so all measured wavelengths must be corrected

Table 4.5: **Conditions and positions for standard- and science frames**

start time May 27(UT)	Alt. (deg.)	Az. (deg.)	Airmass	grism
Standard frames				
04:46:56	75.386	0.746	1.033	600V
04:50:09	75.363	3.063	1.033	600I
04:52:57	75.322	5.037	1.034	300V
04:55:38	75.258	7.046	1.034	1200B
04:58:14	75.174	9.022	1.034	600I
05:02:21	75.002	12.054	1.035	300V
Science frames				
01:16:09	44.309	242.993	1.430	300V
01:28:57	46.855	240.262	1.369	600I
01:46:39	50.277	236.000	1.299	1200B
02:04:21	53.599	230.968	1.242	600V
02:22:28	56.721	225.002	1.196	300V
02:56:15	61.414	211.654	1.139	1200B
03:29:20	64.428	194.306	1.108	600V
04:02:54	65.030	174.642	1.103	600I

for the difference between air and vacuum,

$$\lambda_{air} = \frac{\lambda_{vac}}{n_{air}} = \frac{\lambda_{vac}}{1.00029} .$$

Using this formula on every obtained vacuum wavelength center, the third column in each of the list is obtained. The last column is the difference. Summarized, the wavelength calibration of grism 600I looks good, that of 600V looks very good if one disregard the blend at ~ 5197 Å, while that of grism 300V is a bit more varying. For my purposes the obtained accuracy on the wavelength calibration should be good enough.

Flux calibration

In order to have the absolute flux, not just the relative (i.e. counts on the CCD), frames of a standard star are needed. This standard must be taken on the same night, and preferably as close as possible to the main object. The meaning is to gain information about the observing conditions - extinction, seeing, airmass, and use this to calibrate the actual flux of the object of interest. The standard used for calibration here is EG 274, a hot DA white dwarf, meaning that it is in its final stage as a star and only strong hydrogen lines are present. Data from this star are obtained after the GRB spectra on the same night, at a slightly higher altitude and lower airmass, see Table 4.5. This information is then used when flux calibrating the object frame. You compare the known flux of the standard, with the flux that is observed at that night, and then assume the same relationship between the real flux and the observed flux of the science object. PyRAF does this nicely for you, without too much hassle. Appropriate standard stars suitable for the specific observations may be found from catalogues. The standard is then imaged in the same grisms as the GRB, Figure 4.4. For the standard to be useful, it needs to go through the same reduction steps as a normal science frame.

Renormalizing the flux

Converting the continuum flux to magnitudes, photometry may be used to check the resulting absolute flux calibration. The absolute flux calibration in the section above results in a continuum level of $1.7 \cdot 10^{-17}$ ergs /s/cm around 5300 Å. However, converting this into magnitudes one gets 20.8, which is significantly higher than the photometric V band magnitude of 20.2 obtained by Thöne et al. (2007, in prep) 10.5 hours after the onset of the burst. The two frames in grism 600V are taken 10 and 11.5 hours after the burst, and therefore no time-correction is applied. The V band magnitude is used as this has a sensitivity region covering $5000 - 6000$ Å . As the photometric results are likely more reliable for magnitude measurements, the spectra are renormalized with respect to the photometry. However, it is really only the star formation rate (SFR) derived in Section 6.5 that depend on a correct absolute flux calibration. As it is the Lyα feature that is used to obtain the SFR and this lies in grism 600V, the renormalizing of the fluz is only applied to this grism. Although the V-band does not cover the whole 600V grism, it covers Lyα and it therefore suffice to renormalize the spectra with respect to this band. The flux difference may then be added on to the spectra using the PyRAF task `imarith`.

$$2.512^{V(mag)} = 2.512^{20.2} = 1.2 \cdot 10^{8}$$

$$\begin{aligned} F^{GRB}_{lambda} &= \frac{F^{Vega}_{lambda}}{flux - ratio} \\ &= \frac{3.6 \cdot 10^{-9}}{1.2 \cdot 10^{8}} \\ F^{GRB}_{lambda} &= 3.0 \cdot 10^{-17}\,, \end{aligned}$$

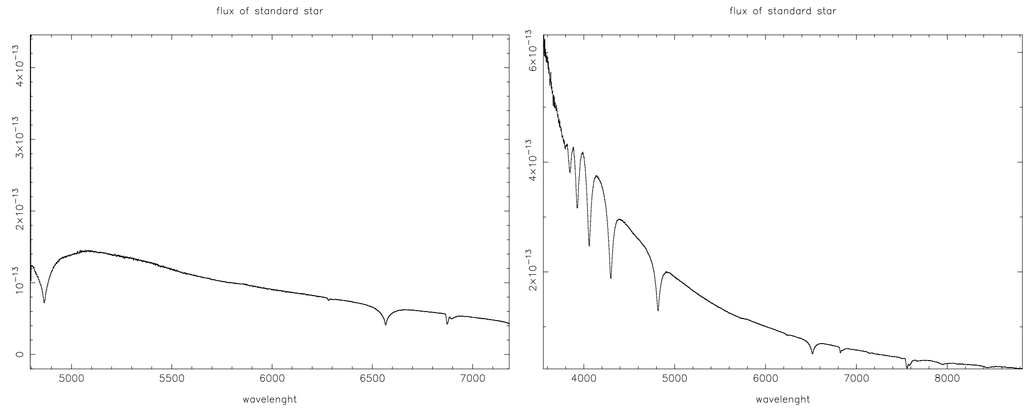

(a) Grism 600V

(b) Grism 300V

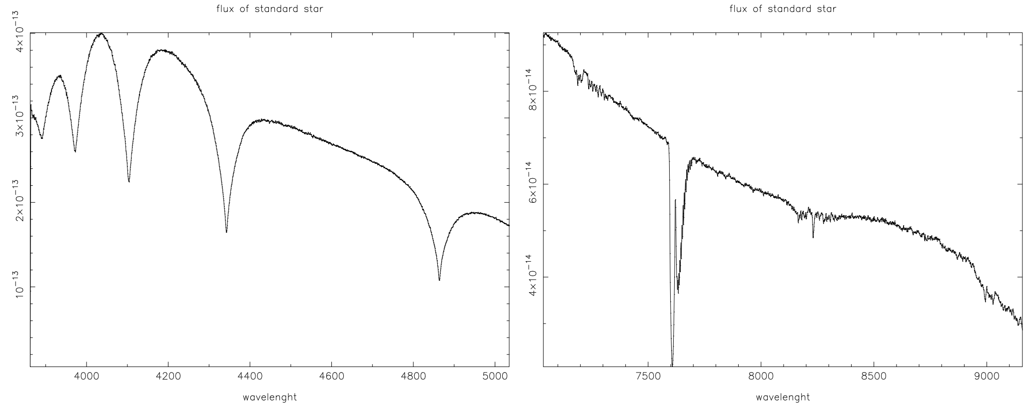

(c) Grism 1200B

(d) Grism 600I

Figure 4.4: The spectra of the standard star in four different grisms. These are used as reference for the flux calibration.

where F_{lambda}^{GRB} is the continuum flux of the GRB around 5300 Å, F_{lambda}^{Vega} is the flux of the star Vega which has a magnitude of approximately zero and therefore is used as calibration. V(mag) is the V-band magnitude of GRB 060526 at the time when the spectroscopic images were taken.

Combining

Since there are two frames in each grism, each pair is combined to improve the signal-to-noise (S/N). To do this, the task `Comb1Dspec` is suitable. The task takes the frames to be combined, each in the PyRAF multispec format, as input

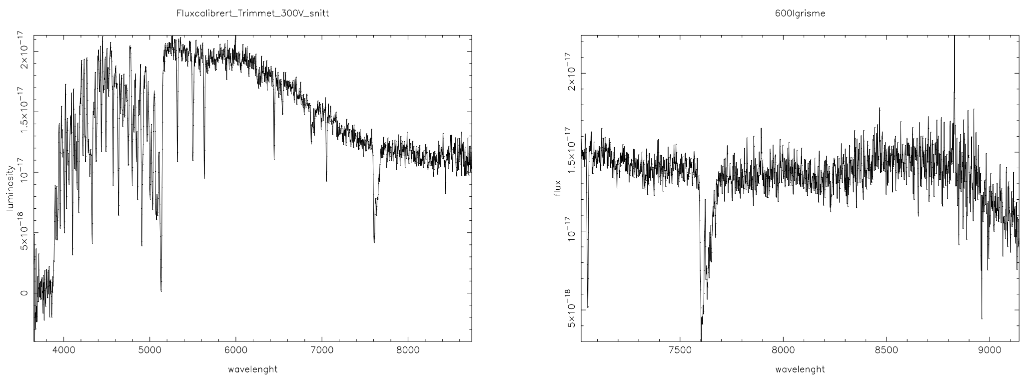

(a) The spectrum of grism 300V

(b) The spectrum of grism 600I

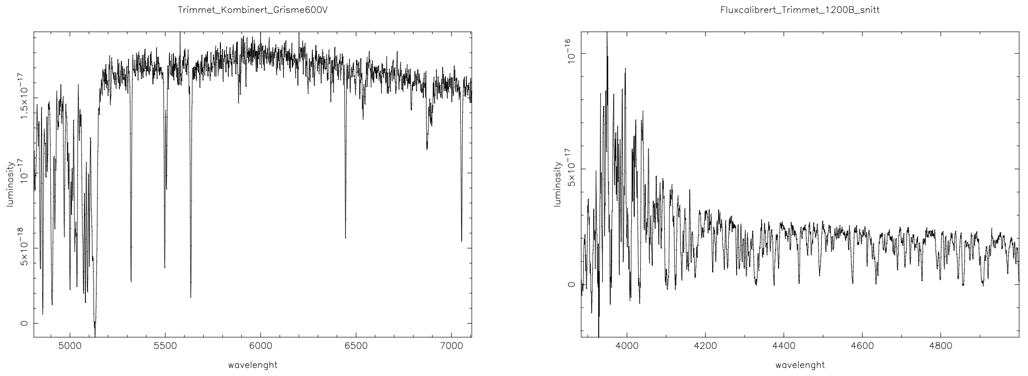

(c) The spectrum of grism 600V

(d) The spectrum of grism 1200B

Figure 4.5: The spectrum of GRB 060526 in four different grisms. In each grism, the spectra are preprocessed in IRAF. Each spectrum consists of two combined frames.

and as output, four separate images areg obtained. One is the combined spectra of the input, the second is the combined error spectrum, the third is the combined sky spectrum and the fourth is the combined signal-to-noise. All the frames are useful, for instance, the sky spectrum is a good place to check the wavelength calibration (with skylines, as described in Section 4.4.3), and both background and error spectrum are needed as input to VPguess/VPFIT. The task `Comb1Dspec` automatically absolute flux calibrates the frames. This is necessary to correct for flux variations in the time interval between the frames. As GRBs evolve quickly, such variations are naturally expected, but also for other objects the flux may vary depending on weather, atmospheric conditions and so on. The combined, flux -and wavelength calibrated spectra are shown in Figure 4.5.

Fitting the continuum

While it is not used to reduce the data, the task `continuum` allows a continuum to be fit to the input spectrum. The continuum is made by interactively fitting a function of optional order to the spectrum. The user may delete deviant pixels and visually decide which fit is the best. As a help, the root mean square (rms) is stated for each fit. The output spectrum may be simply the fit continuum, or it may be the ratio between the continuum and the input spectrum, or the difference between the two. In VPguess the fitted continuum is used as input. The ratio output has been valuable for determining equivalent widths and their errors. A low order continuum is fit to each of the spectra of GRB 060526, the resulting contina are shown in Figure 4.6.

4.4.4 Features not corrected for in the reduction

Reddening and extinction

Reddening corrections in general can be divided into galactic, intervening and host. Since the equivalent widths (EWs), are measured on very small scales, the spectra over those few Ångstrøms have in effect been multiplied by a constant. This does not change the EW, just as the EW is not changed when dividing through by a continuum. Therefore, host extinction is not a problem for abundances.

Heliocentric correction

The need for heliocentric correction arise from the Doppler shift due to the earth's motion around the sun. It is applied to transform measurements to correspond to what an observer at the center of the sun would measure, i.e. a correction for the 30 km/s orbital velocity of the earth. As this will be a small effect for the 600 grisms, possibly noticeable for the 1200B, which is not much used in the analysis because it covers the Lyα forest, heliocentric correction is not applied to the science frames in this thesis.

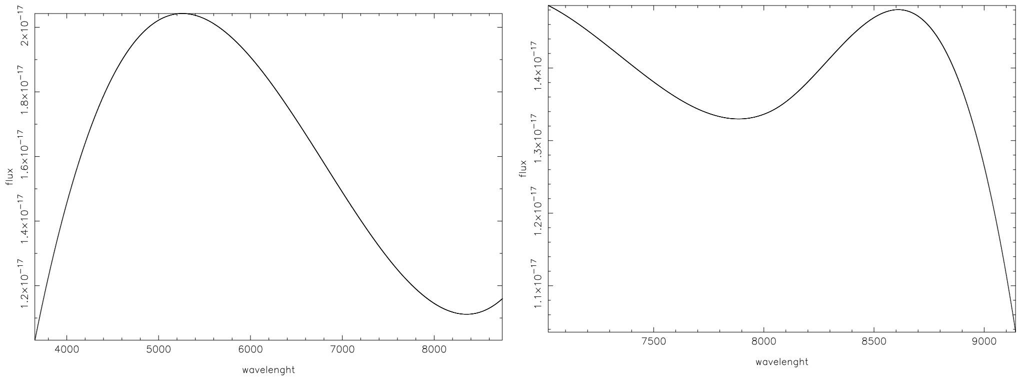

(a) Grism 300V

(b) Grism 600I

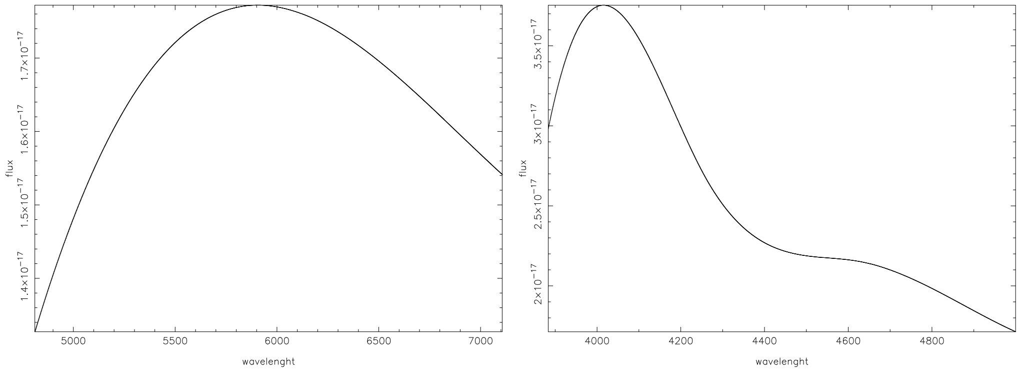

(c) Grism 600V

(d) Grism 1200B

Figure 4.6: The fit contina for the four grisms. All are a low order (~ 3) spline function. Note that the curvatures in these continuum fits look large because of the small y-scales on these plots, covering only $0.5 - 1.5 \cdot 10^{-17}$ ergs/cm^2/s.

Chapter 5

Analysis of the Spectra

This chapter presents the analysis of the preprosessed and combined spectra of GRB 060526 with four different grisms. Using various methods and programs for line identification, line fitting and equivalent width (EW) measurements, column densities, metallicities and equivalent widths are obtained for the elements detected. In Section 5.2, the identified lines and their measured equivalent widths are listed and Equation 3.1 is used to give a first crude estimate of the lower limit column density. Also included is a comment on each identified line, clarifying whether it is a clear or tentative detection, blended line, a possibly unsaturated line, a doublet and so on. These comments also work as a guide to which lines to use for further analysis; unblended and unsaturated lines are often the most valuable sources of information. Accurate column density estimates depend on the detection of unsaturated lines, preferably several from the same ion, something which is difficult to obtain with low resolution spectroscopy. The exception is H I, where the damped Lyα line at $z = 3.2216$, enables accurate measurements of the column density. In order to obtain as certain values as possible for the remaining elements, two different methods are used to estimate column densities. In Section 5.3 the programs VPguess and VPFIT are used to fit the absorption features and in Section 5.4, multi-ion single-component curve of growth (MISC-COG) analysis is applied. A common difficulty with these methods is to decide whether a line i saturated or not. Saturated lines will lead to smaller equivalent widths, which again will lead to lower column densities. Therefore, many of the derived column densities will only be lower limits.

5.1 The redshift of GRB060526

The redshift can be measured from the line center of the very prominent Lyα line in the 600V grism. The center is at approximately 5128.93 Å and we know that the rest frame wavelength of Lyα in vacuum is 1215.67 Å, per definition we then have: $z + 1 = \frac{\lambda_{obs}}{\lambda_{rest}} = 4.2216 \pm 0.0015$. The error corresponds to a 1σ difference in the fit, obtained using VPFIT. At the 1σ level, visual inspection easily reveal that the fit is poor and so, the adopted error is a conservative estimate. The column density obtained is in accordance with the value tabulated at the Swift home page, $z = 3.221$ and the value reported by Jakobsson et al. (2006), $z = 3.221 \pm 0.001$.

5.2 Line identification and equivalent widths

Below follow Tables 5.1, 5.2 and 5.3, one for each of the three grisms, 600V, 600I and 1200B, with all identified lines in the spectra of GRB 060526. Of the four different grisms, the wavelength ranges of 600V, 600I and 1200B are only slightly overlapping, while that of 300V is completely covered by the other grisms. It also has the poorest resolution. Therefore the equivalent width measurements will be based on the three higher resolution grisms.

Measurements of the equivalent widths are conducted in the following way; a continuum is fit to the original spectrum, typically with a low order spline function. The averaged and combined spectrum are then normalized by taking the ratio of the spectra to the continuum. This will force the continuum level to be set at one. The equivalent width is measured on the normalized spectrum using the 'e' option in PyRAF, from the point the line drops below one and up to the point where it again reaches one. If the line is not that well defined, one will have to make a guess, or, if the line is completely blended, give up the measurement. Before calculating the column density with the aid of Equation 3.1, the measured and averaged equivalent widths must be divided by the redshift, so it is the rest equivalent width which is actually used in the calculations. I stress that this calculation only gives a rough lower limit, as the lines are assumed to be optically thin and unsaturated. The wavelength referred to in the tables are the rest wavelengths of the ions. The best fit redshift for each specific line is displayed in the third column, marked 'z'. EW$_{rest}$ is an average of ten equivalent width measurements, divided by ($z + 1$). The σ_1 column is the standard deviation of the equivalent width measurements, i.e, it signifies the error made when measuring the equivalent width. A line with a small σ_1 is probably a well defined line, while a line with large σ_1 might be partly blended or otherwise difficult to define. The other error-measurement σ_2 is the sum of the normalized error spectrum over the same wavelength range as the individual lines. The combined error, $\sigma = \sqrt{\sigma_1^2 + \sigma_2^2}$, is used when estimating the significance of a line. Finally, f is the oscillator strength, a measure of the probability of a transition between two given levels, and $\log N$ is the logarithm of the column density. An equivalent width measurement is derived for all lines, provided that they are not too severely blended with other lines. However, it is the column densities derived from VPguess/VPFIT and curve of growth analysis that will generally be adopted and used for further analysis. All lines detected are significant to at least the 5σ level unless otherwise noted in these comments. The errors should be compared with the *measured* equivalent width, not the rest frame which is given in the tables. However, since I am interested in the ratio between the total error and the equivalent width, I divide the error by $(z+1)$, so that it can be compared directly with the rest frame equivalent width given in the Tables 5.1, 5.2 and 5.3.

Table 5.1: **Equivalent widths for lines in the 600I grism**

Ion	λ (Å)	z	EW_λ^{rest} (Å)	σ_1	σ_2	f	$\log N$
Al II . . .	1670.7890	3.2212	1.1447	0.0097	0.1735	1.88	13.4
Cr II . . .	2062.2340	3.2214	0.1076	0.0175	0.1335	0.121	13.4
Zn II . . .	2062.6600	3.2206	0.1076	0.0175	0.1335	0.202	13.15

Table 5.1: Equivalent widths and column densities for absorption lines in grism 600I.

Comments on lines in grism 600I

Al II(1670.7890) **–** A very strong, unblended line, also evident in grism 600V. It has a very large oscillator strength of $f = 1.88$. The line is very likely optically thick.

Cr II(2062.2340) **–** The Cr II line could be responsible for the small absorption feature at this wavelength, where it fits nicely. However, there are two other Cr II lines of similar oscillator strength in the wavelength range of grism 600I which do not fit any absorption feature. This makes the detection tentative; it is only significant to a level $< 1\sigma$.

Zn II(2062.6600) **–** The same comments as for Cr II. For Zn II it is the Zn II line with twice the oscillator strength at $\lambda = 2026.14$ which is not observed. Only significant to a level of $< 1\sigma$.

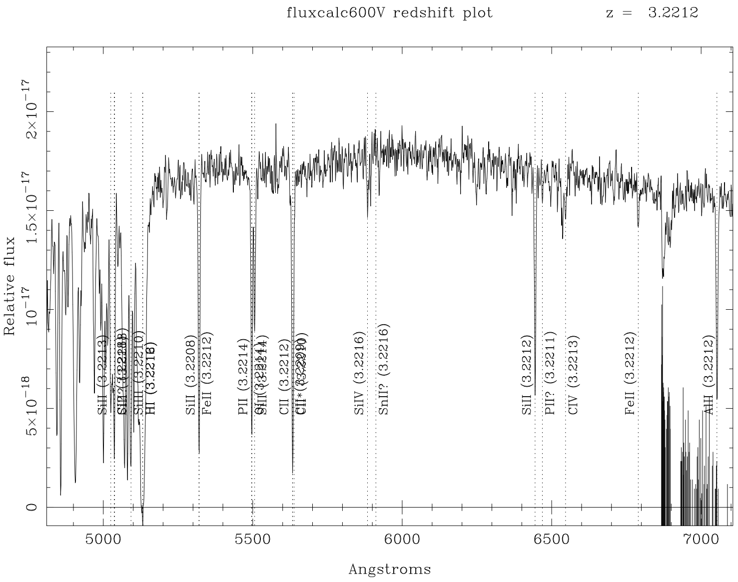

(a) Spectrum with absorption lines, grism 600V

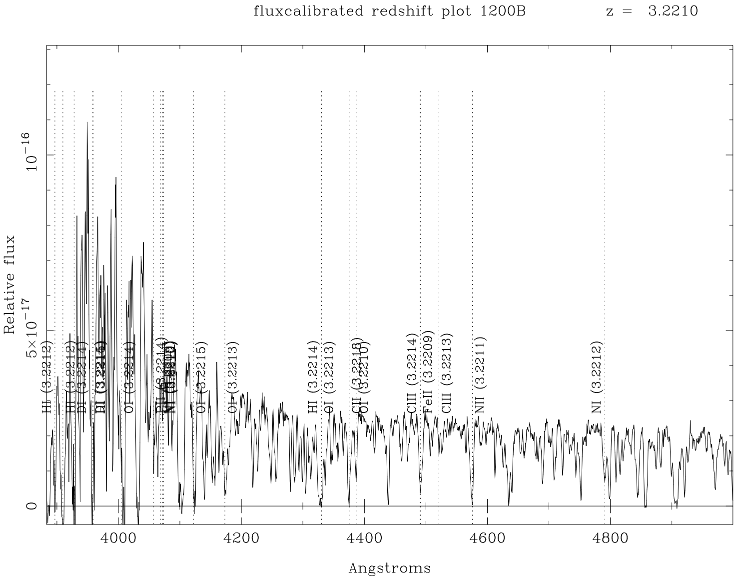

(b) Spectrum with absorption lines, grism 1200B

Figure 5.1: Line identification in the program AREDSHIFT. Clearly visible in a) is the Lyα absorption at ~ 5130 Å, the Lyα forest to the left and several other metal lines to the right. b) Grism 1200B covers the Lyα forest where the lines are very close, making the line identification difficult.

Table 5.2: **Absorption lines in grism 600V**

Ion	λ (Å)	z	EW_{λ}^{rest} (Å)	σ_1	σ_2	f	$\log N$
(1) H I	1215.67	3.2216	6.7887	0.1262	0.0510	4.16E-01	15.10
(1) Al II	1670.79	3.2215	1.0422	0.0032	0.0403	1.74E+00	13.38
(1) C II	1334.53	3.2212	1.6706	0.0282	0.0345	1.28E-01	14.76
C II*	1335.71	3.2210	a)	...	...	1.15E-01	...
	1335.66	3.2210	a)	...	...	1.28E-02	...
C IV	1550.78	3.2214	0.1726	0.0102	0.0269	9.48E-02	13.93
	1548.20	3.2219	0.2231	0.0191	0.0240	1.899E-01	13.74
Fe II	1611.20	3.2212	0.0184	0.0007	0.0199	1.38E-03	14.76
(1)	1608.45	3.2212	0.1822	0.0058	0.0320	5.77E-02	14.14
	1260.53	3.2212	a)	...	...	2.40E-02	...
	1144.94	3.2218	0.0760	0.0014	0.0296	8.30E-02	13.90
N I	1199.97	3.2212	a)	...	...	2.62E-01	...
Ni II	1502.15	3.2215	0.0118	0.0014	0.0239	1.33E-02	13.65
	1467.60	3.2214	0.0306	0.0059	0.0288	1.62E-02	14.17
	1393.32	3.2218	a)	...	...	1.01E-02	...
	1317.22	3.2210	0.0421	0.0026	0.0037	1.21E-01	13.33
O I	1355.60	3.221	0.0536	0.0032	0.0055	1.16E-06	18.45
(1)	1302.17	3.2212	1.1914	0.0285	0.0312	4.80E-02	15.22
P II	1532.53	3.2210	0.0834	0.0037	0.0249	3.03E-03	16.16
	1301.87	3.2215	a)	...	...	1.27E-02	...
S II	1259.52	3.2218	a)	...	...	1.66E-02	...
	1253.81	3.2218	0.0409	0.0010	0.0234	1.09E-02	14.43
	1250.58	3.2218	0.0181	0.0130	0.0236	5.43E-03	14.39
(1) Si II	1526.71	3.2211	0.9499	0.0088	0.0370	1.33E-01	14.54
(1)	1304.37	3.2212	0.6677	0.0393	0.0269	8.63E-02	14.71
(1)	1260.42	3.2215	1.3212 b)	0.0086	0.0383	1.18E+00	13.90
(1)	1193.29	3.2209	1.5468 b)	0.0935	0.0290	5.82E-01	14.32
(1)	1190.42	3.2212	1.1305 b)	0.1287	0.0325	2.92E-01	14.49
(1) Si II*	1533.43	3.2212	0.0176	0.0016	0.0213	1.33E-01	12.80
(1) Si III	1206.50	3.2210	1.3187	0.0379	0.0350	1.63E+00	13.80
Si IV	1402.77	3.2219	0.0966	0.0037	0.0270	2.54E-01	13.34
	1393.76	3.2216	0.1983	0.0113	0.0292	5.13E-01	13.35

Table 5.2: **Absorption lines in grism 600V**

Ion	λ (Å)	z	EW_{λ}^{rest} (Å)	σ_1	σ_2	f	$\log N$

Table 5.2: Absorption lines identified in the 600V grism for GRB 060526. The columns are (left to right): (i) Ion, (ii) rest wavelength of transition, (iii) redshift of the line, (iv) rest frame equivalent width, (v) error on the equivalent width measurement, (vi) error corresponding to the amount of noise in the spectrum at the wavelength range of the particular line, (vii) oscillator strengths and (viii) the logarithm of the column density assuming the optically thin case (Equation 3.1); in most cases this is a lower limit since the lines are generally saturated. $^{a)}$ refers to lines which are too heavily blended to measure equivalent width. $^{b)}$ refers to lines which are blended, but still have a measured equivalent width. $^{1)}$ refers to lines also identified by Jakobsson et al. (2006). Note that the continuum is adjusted for the two S II lines at λ 1250 and 1253. All oscillator strengths are taken from Morton (2003), with the exception of Si II* which is from Ralchenko (2005) and two Ni II lines from Morton et al. (1988).

Comments on the lines in grism 600V

H I(1215.67) – The Lyα line is, as expected, the strongest line in the spectrum. Because it is very heavily saturated, the wings can be fit and give an accurate value for the column density of H I (Petitjean, 1998). The value obtained from H I is very important, because the H I column density is used to express the metallicities of all other ions, see Equation 6.1. A fit of the line is shown in Figure 5.2(a).

Al II(1670.79) – A very strong line, also evident in grism 600I. It is unblended, but very likely highly saturated, and the column density derived from EW measurements is a lower limit.

C II(1334.53) – A strong line, blended with C II* on the red wing. C II is probably dominating the blend (judging from the shape of the line and the wavelengths of C II and C II*), and an attempt to measure the equivalent width and derive a value for the column density is made. However, this is a deep absorption feature which is almost certainly not optically thin, so the derived column density is only a lower limit.

C II*(1335.71, 1335.66) – A weak doublet, blended with C II. The 1335.71 line has an oscillator strength on order of magnitude higher than the 1335.66 line, but the absorption feature seems completely dominated by C II, and measurement of the EW is not obtained.

C IV(1550.77, 1548.20) – Two clearly distinct lines in a C IV doublet. The lines are apparently unblended and an EW measurement is obtainable. Both the relative strengths and redshifts of the two lines are in accordance with each other. These two lines are fit with VPFIT in Section 5.3 and the fits are shown in Figure 5.2(c).

Fe II(1608.45, 1611.20) – The first of the two is a fairly strong line, also detected by Jakobsson et al. (2006) in the same spectrum. Unfortunately, it appears to be mildly saturated and is therefore not an ideal line for column density estimates. The detection of the line 1611.20 is tentative because it is so weak (1σ significance), but if fits nicely in relative strength and redshift with the stronger line. In addition is its highly likely unsaturated and may therefore bee used in VPFIT.

Fe II(1260.53) – Probably part of a blend with Si II 1260.42, see comments on this line.

Fe II(1144.94) – This line lies at the very blue edge of the wavelength range of this grism and so lies in the Lyα forest. It is not included in the fit and two neighboring Fe II lines are not visible. Only significant to a level of approximately 2.5σ.

Ni II(1502.15) – A weak line, probably unblended, might be good for metallicity measurements. It has, however, a significance below 1σ, and so is unreliable.

Ni II(1467.60) – Really a blend of two Ni II lines, 1467.76 and 1467.26, both are very weak and can not be separated at this resolution. In Table 5.2 the weighted average (with respect to oscillator strength) of the wavelengths are given and so also the total oscillator strength and errors. The feature is only significant to a level less than 1σ. Because the lines are so weak they are possibly optically thin.

Ni II(1393.23) – A line comparable in strength to the other Ni II lines, but strongly blended with Si IV on the right wing. The whole absorption feature could be caused by Si IV, which is by far the strongest of the two.

Ni II(1370.13, 1317.22) – Two fairly weak lines, the first is too severely blended to obtain an equivalent width, the second is the only Ni II line detected above a significance of 5σ.

P II(1532.53) – P II is a trace element and therefore strong lines are not expected. The wavelength fit is reasonably good, closer inspection might reveal whether this absorption feature truly is due to P II or if it might be another unidentified ion.

P II(1301.87) **–** The line is clearly completely blended with O I(1302.17). Strong oxygen lines are expected, while P II typically has low abundances. I therefore assume that the O I line dominates the blend and will not attempt to get equivalent width measurements of P II from this absorption feature.

O I(1302.17) **–** Blended with the weaker P II(1301.87) line. This O I line is also detected by Jakobsson et al. (2006) and has a high oscillator strength. In addition to the (weak) blending, it is probably highly saturated, indicating that the column density resulting from EW measurements is a lower limit.

S II(1259.52, 1253.81, 1250.58) **–** The last two of these lines are very weak, and the first line is blended with Si II(1260.42), Fe II(1260.53) and possibly C I(1260.74) and C I*(1260.93). The second of the three lines, has a significance of 1.5σ, the last is only significant to $< 1\sigma$. However, all three lines match absorption features and the relative strength between the lines also fits the absorption features. The two unblended lines have potential for metallicity measurements since they are probably not saturated.

Si II(1304.37) **–** A strong line, blended with O I on one wing. The blend is not too severe and an EW measurement is easily obtained, resulting in a lower limit on the column density.

Si II(1260.42) **–** This is a complex absorption feature, likely a blend of Si II, Fe II, C I, C I* and S II. The Si II line at this wavelength has a large oscillator strength and comparing relative strength (in VPguess) with other Si II lines, it is clear that Si II is largely responsible for the absorption feature. However, comparing the relative strengths of Fe II lines in the spectrum indicate that also Fe II contributes to the absorption feature on the red wing. Also C I(1260.74) and C I*(1260.93) may contribute on the red wing. On the blue wing the line S II(1259.52) fits the absorption nicely. As previously mentioned, the detection of the S II line is made probable by the detection of two weaker S II lines close by. Because of the complex blend, EW measurements are highly uncertain, and it should be placed more confidence in the results from Si II(1304.37). As the Si II lines are probably all saturated, and therefore represent lower limits on the column density, Si II(1260.42) impose no further restrictions on the column density as the value is lower than that derived from other Si II lines. Jakobsson et al. (2006) report detection of Si II, not Fe II (or any other ion) at this wavelength.

Si II(1193.29, 1190.42) – Two clear, strong lines. All the strongest lines (highest oscillator strength) from Si II are detected and their relative oscillator strengths fit well. Both of these two Si II lines are also reported by Jakobsson et al. (2006) in the same spectrum.

Si II*(1533.43) – A very weak line, also detected by Jakobsson et al. (2006) in the same spectrum. However, the lack of detection of the stronger Si II* lines at ~ 1265 Å, makes the detection questionable. The line could potentially be important for column density calculations, and the ratio of Si II* to Si II may give information about the volume density of H I (Fynbo et al., 2006a; Silva & Viegas, 2002). The line is only significant to approximately 1σ.

Si III(1206.50) – A strong line, the wings on both sides are blended with two unidentified lines. The blend is not too severe and a column density measurement is obtained. It is the only Si III line within the wavelength range of the spectra. The line is also detected by Jakobsson et al. (2006).

Si IV(1402.77, 1393.29) – These lines are clear, but not very strong. The first is only significant to a level of 3σ. The other is approximately 5σ. There is a chance they are only very mildly saturated, and for this reason they are fitted, using VPguess/VPFIT in Figure 5.2(b). The first (1393 Å) could be blended with a weak Ni II line on the red wing, the second appears unblended. If the lines really are unsaturated, the column densities derived from EW measurements of the two lines should be in accordance with each other and with the results from VPFIT. The EW measurement of the two lines both give $\log N = 13.3$, while VPFIT gives $\log N = 13.5$. (see Table 5.2 and Section 5.3).

Table 5.3: **Absorption lines in grism 1200B**

Ion	λ (Å)	z	EW_{λ}^{rest} (Å)	σ_1	σ_2	f	log N (cm $^{-2}$)
H I	1025.72	3.2214	1.3234$^{b)}$	0.1027	0.0380	7.91E-02	15.25
	972.54	3.2210	$^{a)}$	· · ·	· · ·	2.901E-02	· · ·
	949.74	3.2209	$^{a)}$	· · ·	· · ·	1.395E-02	· · ·
	937.80	3.2215	0.4498$^{b)}$	0.0853	0.0744	7.80E-03	15.87
	930.75	3.2210	1.2886	0.1213	0.0352	4.82E-03	16.54
	926.23	3.2210	2.1674	0.2847	0.0570	3.19E-03	16.95
	923.15	3.2210	0.7833	0.0644	0.0507	2.22E-03	16.67
C II	1036.34	3.2218	1.0017	0.0063	0.1848	1.18E-01	14.95
C II*	1037.02	3.2214	$^{a)}$	· · ·	· · ·	1.18E-01	· · ·
C III	977.02	3.2219	$^{a)}$	· · ·	· · ·	7.57E-01	· · ·
Cl II	1063.83	3.2214	$^{a)}$	· · ·	· · ·	5.03E-03	· · ·
	1071.04	3.2220	0.1783	0.0112	0.0308	1.50E-02	15.07
Fe II	1063.97	3.2209	1.0942	0.0079	0.1516	4.75E-03	16.36
	1063.18	· · ·	$^{c)}$	· · ·	· · ·	5.47E-02	· · ·
	1144.94	· · ·	$^{c)}$	· · ·	· · ·	8.30E-02	· · ·
	1125.45	· · ·	$^{c)}$	· · ·	· · ·	1.56E-02	· · ·
	1096.88	· · ·	$^{c)}$	· · ·	· · ·	3.27E-02	· · ·
	1083.42	· · ·	$^{c)}$	· · ·	· · ·	2.80E-03	· · ·
N I	1134.66	3.2215	0.9367	0.0323	0.0351	8.49E-02	14.99
	965.04	3.2211	0.1604	0.1012	0.0277	3.86E-03	15.70
	964.63	3.2211	0.2941	0.1631	0.0340	7.90E-03	15.66
	963.99	3.2211	0.2921	0.1525	0.0371	1.24E-02	15.46
	954.10	3.2214	$^{a)}$	· · ·	· · ·	4.00E-03	· · ·
	953.77	3.2214	$^{a)}$	· · ·	· · ·	7.07E-02	· · ·
N II	1083.99	3.2211	0.9311	0.0140	0.0367	1.11E-01	14.91
O I	1039.23	3.2210	0.5561	0.0051	0.0353	9.07E-03	15.81
	1025.76	3.2213	$^{a)}$	· · ·	· · ·	0.19E-02	· · ·
	988.77	3.2213	$^{a)}$	· · ·	· · ·	4.65E-02	· · ·
	988.65	3.2213	$^{a)}$	· · ·	· · ·	8.30E-03	· · ·
	988.58	3.2213	$^{a)}$	· · ·	· · ·	5.53E-04	· · ·
	976.45	3.2215	0.7626$^{b)}$	0.1978	0.0416	3.31E-03	16.44
	971.73	3.2210	$^{a)}$	· · ·	· · ·	1.38E-02	· · ·
	950.89	3.2218	$^{a)}$	· · ·	· · ·	1.58E-03	· · ·
	948.69	3.2216	0.7511$^{b)}$	0.1100	0.0576	6.31E-03	16.16
	937.80	3.2218	$^{a)}$	· · ·	· · ·	8.77E-04	· · ·
	936.63	3.2218	$^{a)}$	· · ·	· · ·	3.65E-03	· · ·

Table 5.3: **Absorption lines in grism 1200B**

Ion	λ (Å)	z	EW_λ^{rest} (Å)	σ_1	σ_2	f	log N (cm $^{-2}$)
	930.26	3.2215	$^{a)}$	···	···	5.37E-04	···
	929.52	3.2215	$^{a)}$	···	···	2.29E-03	···
	925.45	3.2220	$^{a)}$	···	···	3.54E-04	···
	924.95	3.2220	$^{a)}$	···	···	1.54E-03	···
P II	963.80	3.2214	$^{a)}$	···	···	1.46E+00	···
	961.04	3.2214	0.3711	0.0853	0.0345	3.49E-01	14.11
Si II	1020.70	3.2218	0.2007$^{b)}$	0.0174	0.0221	1.68E-02	15.11
	989.87	3.2218	0.3959$^{b)}$	0.0306	0.0292	1.71E-01	14.43

Table 5.3: Absorption lines identified in the 1200B grism for GRB 060526. The columns are (left to right): (i) ion, (ii) rest wavelength of transition, (iii) redshift of the line, (iv) rest frame equivalent width, (v) error on the equivalent width measurement, (vi) error corresponding to the amount of noise in the spectrum at the wavelength range of the particular line, (vii) oscillator strengths and (viii) the logarithm of the column density assuming the optically thin case (Equation 3.1). $^{a)}$ refers to lines which are too heavily blended to measure equivalent width.$^{b)}$ refers to lines which are blended, but still have a measured equivalent width, $^{1)}$ refers to lines also identified by Jakobsson et al. (2006). At a redshift of $z = 3.221$, the 1200B grism covers the Lyman alpha forest, making equivalent width measurements and line identification difficult. All oscillator strengths are taken from Morton (2003).

Most lines are detected above 5σ significance. The exceptions are H I(937.80) at 2.8σ, C II(1036.34) at 1.5σ, Cl II(1071) at 4.2σ N I(956.04) at 1.2σ, N I(964.63), and N I(963.99) at 1.5σ, O I(976.45) at 3.2σ, and P II(961) at 3.1σ. However, as is reflected by the two separate error measurements in the table, most of these lines are poorly defined, causing a high σ_1. The detections themselves are therefore quite clear, but the column density will have large uncertainties.

Comments on the lines in grism 1200B

H I(1025.73) **–** The absorption feature is primarily due to the H I line, blended with two oxygen lines, O I(1025.76, 1026.47). The feature is very broad and other ions might also contribute. Saturation and heavy blending make it difficult to obtain accurate equivalent width measurements. However, the heavy saturation provides a more reliable column density, obtained from fitting the wings of H Iα. The short-coming of EW measurements of H I lines is clearly illustrated by comparing the value derived from EW measurements in Table 5.3 with the value obtained from H Iα fitting. As expected the EW based value is much too low and the same is true for the log N results derived EW measurements of H I(937.80), H I(926.23), and H I(930.75).

H I(972.53) **–** A deep absorption feature where the H I line is blended with O I(971.74) and at least one more component which is not identified. Accurate EW measurements are difficult to obtain for any of the involved transitions.

H I(949.74) **–** The H I absorption line is blended with O I on each wing. The feature is broad and has a bump in the center, exactly at the wavelength of the H I line. The blending makes it difficult to obtain an accurate equivalent width measurement for any of the involved transitions/lines.

H I(937.80, 930.74, 926.23, 923.15) **–** Four strong lines, all blended with O I at least on one wing. Measurements of EW have been attempted for H I(937.80, 926.23 and, 923.25). Of these, the two last are the weakest and least blended. They are, however, still saturated and the resulting log N are very much below the value obtained from Lyα.

C II(1036.34) **–** A strong line which might be blended with C II*(1037.02) on the red wing. There is only one other C II line in the spectra, which is also likely blended with C II*. This makes it difficult to determine whether the relative oscillator strengths of the two fit with the spectra, but it seems probable that C II dominates the blend.

C II*(1037.02) **–** Probably blended with C II. Since there is only one more C II* line and that line is also heavily blended, it is difficult to compare the relative oscillator strengths. However, both absorption features are a blend of the same ions (C II*, C II, O I), and from fitting in VPFIT, it seems that the C II* component is the weaker of the three. With the transitions of C II* and C II having about the same oscillator strength, the column density of C II* is most likely also lower. Since all the lines might be saturated, a fit will only be hinting the right relative abundances.

Fe II(1063.97, 1063.18) **–** A blend of singly ionized iron lines, probably also C II(1063.83). In general the Fe II lines do not look particularly good in the 1200B grism. Neither the relative strengths between individual lines nor the redshift fit match the spectrum. In such a poor fit, even the EW measurement of a line that actually fits will not be given much credit, so column density estimates based on the 1200B grism are highly uncertain.

Fe II(1083.42, 1096.88, 1125.45, 1144.94) – These are only a few of the Fe II absorption lines expected to bee seen in grism 1200B. There are indeed many additional absorption features which almost coincides with Fe II lines, but they will not match up completely. Since there are no skylines to check the wavelength calibration with at this wavelength range, I cannot exclude the possibility that the calibration is off, causing the discrepancies. However, several other absorption features of different ions fit nicely, reducing the likelihood of a miscalibration. More likely the observed lines are not due to Fe II, but other unidentified ions.

N I(1134.98, 1134.42, 1134.17) – The first line is a bit off the absorption feature, while the two others are a better, but not perfect, match. In relative strength they fit well with the N I$(953 - 954)$ Å lines. The lines are fairly strong and might be saturated, but an attempt on EW measurement on the strongest line in the blend N I(1134.98) gives a column density in accordance with values derived from weaker lines.

N I(965.04, 964.63, 963.99) – Very weak, blended lines. All three lines are only detected at a significance between 1σ and 2σ. The reason for this is their blending. The lines are measured separately, and it is difficult to define each line. The detection itself is, however, quite certain. This can be seen in Table 5.3 from σ_1 and σ_2. The profile of the absorption feature fits these lines reasonably well. However, in the spectrum the N I(964.63) is the deepest, but this is not in accordance with the oscillator strengths which are larger for N I(963.99) than N I(964.63). All three lines are - relative to their oscillator strength - deeper than the other absorption features of N I. This might be due to difficulties with assigning a continuum to the feature-rich Lyα forest or, since these three lines are amongst the N I lines with the lowest oscillator strengths, it might be a hint that the other N I lines are saturated. Another explanation might be that all lines are blended with some other ion. P II is a candidate for a blend with N I(963.99), but no other lines which could blend with N I(965) and N I(964) are identified.

N I(954.10, 953) – Relatively weak, but clear lines. The line N I(953) is really a blend of the closely spaced lines N I$(953.97, 953.65, 953.42)$. Also blended with some other unidentified line on the red side. Equivalent width measurements are easier on the N I$(963$ - $965)$ lines, as they are less blended. It is difficult to compare the relative strengths of these lines, as the two red-most lines seem completely blended with an unidentified feature.

N II(1083.99) – A strong line, blended with Fe II(1083.42). Because of the poor fit of Fe II lines and the lack of other N II lines, it is difficult to say what fraction of the absorption feature is due to N II.

***O I(1039.23)* –** A fairly strong unblended line, probably the best oxygen line for measuring equivalent width to get a reliable lower limit column density.

***O I(1025.76, 1026.47)* –** The absorption feature is due to a blend between the two oxygen lines and H I(1025.72), which makes it difficult to get an accurate equivalent width measurement. The feature is very broad and might also be a blend of other lines.

***O I(988.58, 988.65, 988.77)* –** These are strong lines, impossible to tell apart with this resolution. They are part of a larger absorption feature, which prevent measurements of the equivalent widths.

***O I(976.44)* –** A very strong, blended line. The blend (probably with C III(977.02)), makes it difficult to measure the equivalent width. The result of an attempt is given in Table 5.3. However the line O I(1039.23), has a much lower standard deviation and a more accurate EW measurement. The lower limit column density derived from O I(1039.23) should therefore be preferred.

***O I(971.73)* –** Consists in fact of three closely spaced O I lines, O I(971.737, 971.738, 971.93), which are inseparable at this resolution. The O I lines are part of a larger blend with H I, and difficult to use for EW measurements. The oscillator strength given in the table are the sum of the three individual oscillator strengths.

***O I(950.89)* –** Blended with H I, and difficult to use for EW measurements.

***O I(948.69)* –** The line is a blend with H I on the right wing, which makes it difficult to measure EW. I have tried and the result is given in Table 5.3. However, the line O I(1039.23), has a much lower standard deviation and a more accurate equivalent width measurement. The lower limit column density derived from O I(1039.23) should therefore be preferred.

***O I(937.80, 936.63, 930.26, 929.52, 925.45, 924.95)* –** The lines are blended with each other and with strong H I lines. Therefore, EW measurements will be highly uncertain and they are not used as column density estimates. However, all the lines are clearly detectable even with their low oscillator strength.

***P II(961.04, 963.80)* –** The blue-most line looks relatively strong and blended with an unidentified feature. The red-most line is blended with N I(963.99). Because of the blending it is difficult to say whether their relative strengths are compatible and even to determine whether it really is P II which is responsible for these two absorption features. Because of the blends, none of the lines are good for measuring EW, but the result of an estimate using P II(962.04) is given in Table 5.3.

Si II(989.87, 1020.70) – Two clear lines, the first lying on the red wing of O I(988.58), the second lying on the blue wing of an unidentified absorption feature. Their relative strengths and redshifts fit nicely with each other. Even though they are both blended on one wing, EW measurements seem fairly straight forward.

5.3 Models and column densities using VPFIT

VPFIT is a program to facilitate the fitting of multiple Voigt profiles to spectroscopic data. VPguess is a graphical interface, simplifying and guiding the first inputs. VPguess/VPFIT gives a range of opportunities to fit the different lines, parameterized by the column density, redshift and the Doppler parameter. Each of these three parameters can be tied to the same parameter of other ions, or set to be fixed at a chosen value. Since it is natural that, for instance, low ionization ions of different elements originate at the same localization, one can tie the redshift of these to each other, forcing it to be the same. The Doppler parameter, b, is the combined result of turbulence and temperature. When tying the b parameters every b parameter in the tie is calculated from

$$b^2 = v_{turb}^2 + f \cdot T/m\,,$$

where m is the element's atomic number and the constant $f = 2 \cdot k/u/10^{-6} = 0.0166$, k is Boltzmann's constant, u is atomic mass unit. As I wish use a range of different ions to decide the value of the b-parameter, all fits with tied b parameters of this section have the velocity due to turbulence, v_{turb}, set to zero and $T = 1$K. With these settings, the varying masses of the ions are negligible because of the low temperature. For all ions in the tie, m is then set to the atomic number of the reference ion. Note also that $v_{turb} = 0$ does not assign the value of zero to the turbulence. The notation only means that v_{turb} is free to be fit. The line lists used for this program has the oscillator strengths incorporated, and this allows a comparison of strengths between different lines of the same ion. As input, VPguess/VPFIT needs the spectrum and its associated error spectrum, continuum and sky spectrum. The error -and sky spectrum are two of the layers in the PyRAF multi-spec format, and are automatically combined and renamed when using the `Comb1Dspec` task in PyRAF (by Vreeswijk, see Section 4.4.3). The continuum can be fit in the PyRAF task `continuum`. One is also asked to supply the FWHM of the instrumental line spread function. This information can be estimated for example from the skylines by fitting a Gaussian to one of the skylines and reading of the GFWHM, see Table 4.5.

5.3.1 Fitting with VPFIT

Using VPFIT and VPguess, models based on the absorption features in the spectra are made and over-plotted on the actual spectra to visualize the fit. The best lines to fit are the very strong (highly saturated) and very weak (ideally optically thin, in practice slightly saturated). Only one line seems to be sufficiently saturated, namely Lyα. Ions responsible for the weak lines included in the fit are Si IV, C IV, Fe II, S II, Ni II, P II and O I. The fitted lines are listed in Table 5.4, from left to right the columns are (i) ion, (ii) rest wavelength, (iii) rest equivalent width, (iv) error measured from the error spectrum in IRAF, (v) the grism where it is detected. The three lines of Ni II where no equivalent width is listed are blended. a) signalizes that Ni II(1467.76) and Ni II(1467.26) are blended with each other, and the column density and error listed is the total of the two.

In the first fit, both the redshifts and the Doppler parameters are tied for the majority of ions. High ionization and low ionization ions are tied separately. H I is so highly saturated that it does not contain information on the Doppler parameter, no ties are laid on this ion. For Ni II and O I, only the Doppler parameter is tied to the other ions. Fe II is used as reference for the ties of the low ions, Si IV for the high ions. In the fit, each fitting-region is marked with a line above the spectrum. Some of the fits have continuum corrections which are marked by CC. In these cases, the dotted line represents the original continuum which is not a part of the actual fit. Figure 5.2 visualizes the fit, while Table 5.5 lists the corresponding parameters; from left to right: (i) ion, (ii) column density, (iii) redshift, (iv) Doppler parameter, (v) error on the logarithm of the column density, (vi) error on the redshift, (vii) error on the best fit Doppler parameter. Note that for ions tied in redshift or Doppler parameter, only the first ion in the tie will have error measurements.

When fitting the Lyα line of neutral hydrogen and very weak lines, the exact continuum level is of particular importance. Due to the Lyα forest on the blue side of this line, a low order continuum (dotted line) will drop off, resulting in a lower column density of H I. To obtain a more accurate continuum level, it was fitted interactively (solid line). The uncertainties introduced by the continuum level for H I is dealt with in Section 5.3.3.

The Si IV doublet in 5.2(b) and the C IV doublet in 5.2(c) are tied separately

Table 5.4: **Lines fit in VPFIT**

ion	λ_{rest} (Å)	W_{rest} (Å)	σ_2	grism
H I	1215.67	6.7887	0.0510	600V
C IV	1550.78	0.1726	0.0269	600V
	1548.20	0.2231	0.0240	600V
Fe II	1611.20	0.0184	0.0199	600V
	1608.45	0.1822	0.0320	600V
Ni II	1703.41	. . .	. . .	300V
	1709.60	0.1010	0.0508	300V
	1741.55	0.0547	0.0442	300V
	1751.92	. . .	. . .	300V
	1502.15	0.0118	0.0239	600V
	1467.76	0.0306	0.0288	600V
	1467.26	a)	a)	600V
	1393.32	. . .	. . .	300V
	1370.13	0.0365	0.0351	300V
	1317.22	0.0421	0.0115	600V
O I	1355.60	0.0536	0.0346	600V
P II	1532.53	0.0834	0.0234	600V
S II	1253.81	0.0369	0.0234	600V
	1250.58	0.0116	0.0236	600V
Si II* . . .	1533.43	0.0176	0.0213	600V
Si IV	1402.77	0.0966	0.0270	600V
	1393.76	0.1983	0.0292	600V

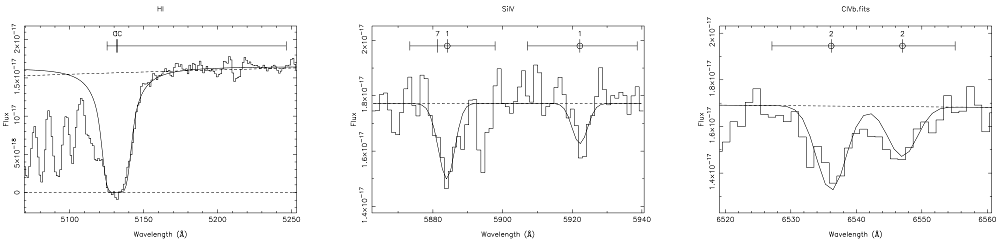

(a) H I with locally corrected continuum

(b) The Si IV doublet

(c) The C IV doublet

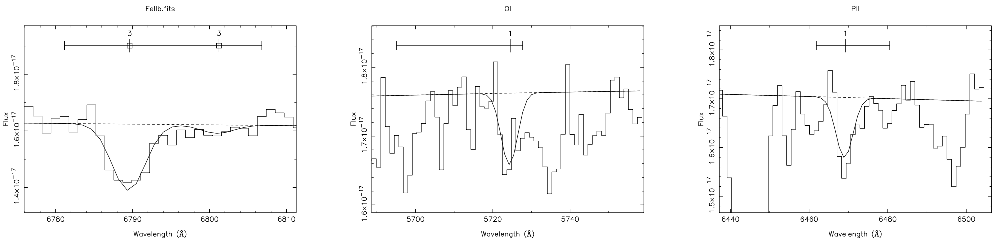

(d) Fe II(1608) and Fe II(1611)

(e) O I(1355)

(f) P II(1532)

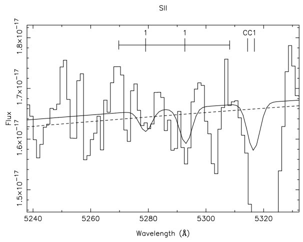

(g) S II(1251) and S II(1254) with locally corrected continuum

Figure 5.2: Lines fitted with VPFIT for a tied b parameter. Ni II has many weak lines and is fitted separately in Figure 5.3.

ion	log(N)	z	b (km/s)	log$N$ error	z error	b error (km/s)
Si IV	13.55	3.2218^a	20.5^c	0.14	0.0001^a	$7.77\ ^c$
C IV	14.20	3.2218^a	20.5^c	0.20	.......^{a}	.....^{c}
Fe II	14.93	3.2213^b	9.9^c	0.27	.......^{b}	.....^{d}
P II	15.51	3.2213^b	9.9^c	0.27	.......^{b}	.....^{d}
H I	20.01	3.2213	132.3	0.04	0.0004	11.02
Ni II	13.99	3.2214	9.9^d	0.16	0.0007	.....^{d}
S II	14.72	3.2213^b	9.9^d	0.23	.......^{b}	.....^{d}
O I	18.70	3.2225	9.9^d	0.23	0.0009	.....^{d}

Table 5.5: **Column densities from VPFIT.** a) symbolizes the redshift tie and c) the Doppler tie of the high ionization ions, Si IV and C IV. b) symbolizes the redshift tie and d) the Doppler tie of the low ionization ions. Only the ion to which the others are tied will have error estimates.

because they are highly-ionized and are likely to originate in different environments than low ionization ions. Both doublets fit the absorption features nicely and the resulting column densities are two of the most reliable, even though an error of respectively 0.14 dex and 0.2 dex are significant uncertainties. The column density of Fe II has large uncertainties, and it would have been beneficial to include other Fe II lines. Unfortunately, all but one of the other Fe II lines lie in the Lyα forest at this wavelength. The only other line with a higher wavelength, Fe II(1260) is heavily blended with Si II(1260). The Fe II(1608) line appears rather rounded in the bottom, and it is very sensitive to the value of the Doppler parameter. This is further discussed in Section 5.3.2. In total there are three P II lines in the wavelength range of the 600V grism. Only P II(1533) is possible to fit as the other lines are respectively blended with the 1301 (Å) absorption feature and in the Lyα forest. The column density of P II is suspiciously high, as phosphorus is a trace element, but again, there are no further lines available to get a more robust fit. In addition, the line might be blended with a fine structure line of silicon, Si II*(1533), and considering the very high column density for phosphorus resulting from this fit, the contribution of Si II* should be taken into consideration. This is done in a second run through VPFIT, see 5.6. Another likely possibility is that this line is not due to neither the P II nor the Si II* transition, but originates in another absorption system. The two weak sulphur lines, S II(1251, 1254) are fit with a continuum correction where the new level is set interactively. There is one additional line in the wavelength range of grism 600V, namely S II(1260). It is the strongest of the three, but also heavily blended and therefore not fitted. There are no other S II lines expected to be detected in the wavelength range of any of the

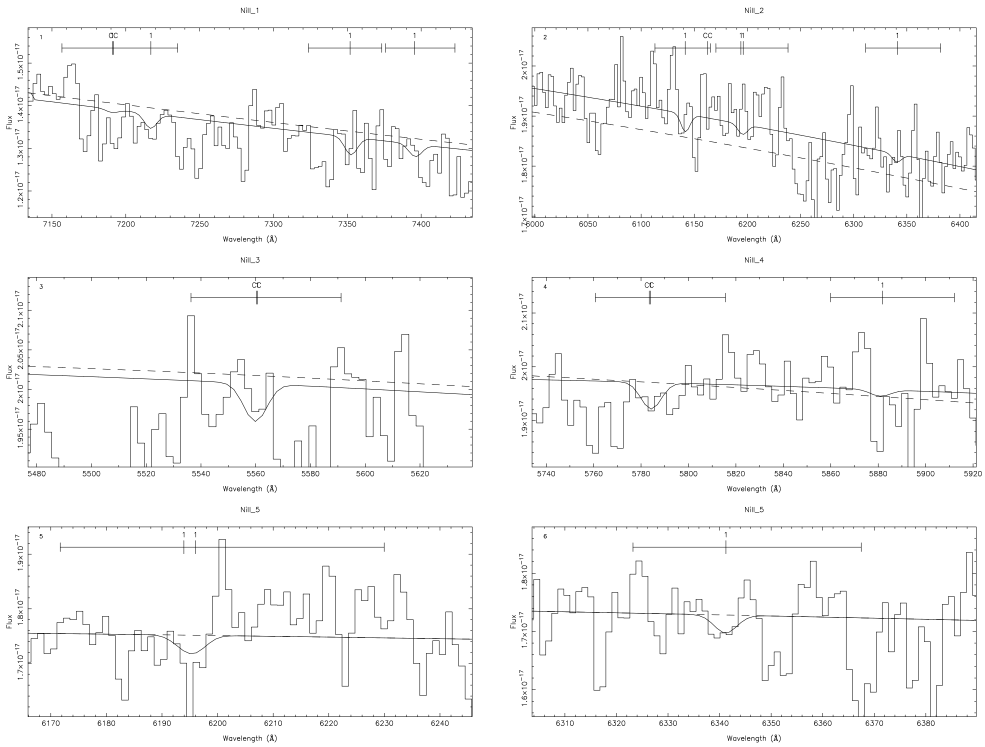

Figure 5.3: The fit of all Ni II lines with tied b parameter. From grism 300V, starting in the upper right corner: (i) Ni II($1703, 1710, 1742, 1752$), (ii) Ni II($1455, 1467.3, 1467.8, 1502$), (iii) Ni II($1317$), (iv) Ni II($1370, 1393$), from grism 600V: (vii) Ni II($1467.3, 1467.8$) and (viii) Ni II(1502).

grisms. All oxygen lines, except for O I(1355) which is plotted in Figure 5.3.1, are highly saturated, blended or both. Because of its weakness it is a potentially important line, since it has a very low oscillator strength and therefore might be optically thin. However, the fit is poor and the redshift is slightly off compared to the other ions, see (Table 5.5). As O I (and N I) have a neutral ionization potential, IP > 13.6 eV, they are expected to be found at the same redshift as singly ionized ions such as C II, Si II, S II, Fe II which have their first IP < 13.6 eV and second IP > 13.6 eV (Vladilo et al., 2001). In addition, the resulting oxygen column density is suspiciously high, suggesting that the continuum level might be too high, or that it is not an actual detection of O I, but rather a skyline or another system. In total there are eleven Ni II lines within the wavelength range of 300V, seven of these are also within the range of 600V, four within the range of grism 600I. Figure 5.3 shows the fit of some of these lines, which all are very weak. Ni II($1467.3, 1467.8, 1502$) are all good fits in grism 600V, but in grism 300V they

Ion	log$N$ (cm^{-2})	z	b (km/s)	log$N$ error	z error	b error (km/s)
Si IV	13.44	3.2218^{a}	40.0^{c}	0.0707	0.0002^{a}	…^{c}
C IV	14.00	3.2218^{a}	40.0^{c}	0.0505	…^{a}	…^{c}
Fe II	14.24	3.2213	40.0^{c}	0.0741	0.0003	…^{c}
P II	15.26	3.2216	40.0^{c}	0.1492	0.0006	…^{c}
Si II*	13.26	3.2195	40.0^{c}	3.2779	0.0053	…^{c}
Ni II	13.88	3.2219	40.0^{c}	0.2051	0.0008	…^{c}
S II	14.61	3.2213^{b}	40.0^{c}	0.1720	…^{b}	…^{c}
O I	18.82	3.2304	40.0^{c}	0.2123	0.0010	…^{c}

Table 5.6: **Column densities and errors from VPFIT, with b = 40 km/s.** a) the redshift tie of the two high ionization ions, b) a redshift tie on SII, c) fixed Doppler parameters, and correspondingly no errors on this value.

are not detected. The line Ni II(1317) looks very similar in both grisms and is a fairly good fit. Ni II(1370) is only detected in grism 300V and Ni II(1393) is blended with the C IV doublet. None of the four Ni II lines within grism 600I are convincingly detected. The column density of Ni II listed in Table 5.5 is the result of the combined fit of all lines in Figure 5.3. Four of the frames have been locally continuum-corrected. Since the lines are very weak and several lines show non-detection in at least one of the spectra, the column density is very uncertain and should probably be regarded as an upper limit. To further test this conclusion, the 3σ limit on the strongest undetected line is calculated and a limit of log $N(\mathrm{Ni\ II}) < 14.2$ is found. This is only 0.2 dex higher than the derived column density.

5.3.2 Variation of the Doppler parameter

In a second run through VPFIT the Doppler parameter is fixed at the best fit value ($b = 40$ km/s) obtained from the MISC-COG analysis (Section 5.4). The remaining parameters to be fitted in VPFIT are then redshift and column density. The resulting column densities tend to drop $0.05 - 0.2$ dex with respect to the first run. This is as expected since all the fit lines are slightly saturated and their column densities therefore do depend on the b-parameter (although the dependence is much less pronounced than for more saturated lines). If the lines were truly in the optically thin regime the column density would be independent of the Doppler parameter. There are, however, a few notable exceptions which vary more; the Fe II ion drops dramatically from $\log N(\mathrm{Fe}) = 14.99$ to $\log N(\mathrm{Fe}) = 14.24$, i.e. 0.75 dex. In the figures this is evident on the Fe II(1611) line; in Figure 5.2(d),

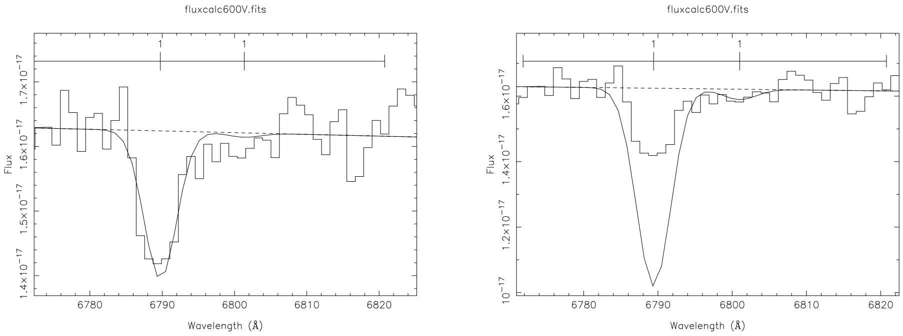

(a) The fit of Fe II for a fixed Doppler parameter.

(b) A fit of only the weakest Fe II line at $\lambda 1611$ Å

Figure 5.4: The column density obtained from this fit is 14.00 with an error of 0.25. The b-parameter is tied to 40 km/s and $\chi^2 = 0.33$.

the line is nicely fit, while in Figure 5.4(a) there is hardly any deviation from the continuum level at this wavelength. This means that the column density of the fit depends on the b parameter, which I interpret as a sign that the Fe II(1608) line is more saturated than the other weak lines used in the fit. In Figure 5.4(b) only the Fe II(1611) is fit, and the column density is in accordance with that of the first fit with b-parameters tied to each other. This is the column density which is adopted for Fe. Another notable discrepancy is the redshift and column density of neutral oxygen. The column density is 0.2 dex higher and the redshift is significantly higher (0.01) than in the first run. The reason for this is that in the absence of redshift ties, VPFIT choose to fit the neighboring (and larger) absorption feature. Fixing the redshift - to make sure that the correct absorption feature is fitted, and the Doppler parameter at 40 km/s, the results are very much the same as in Figure 5.3.1 where the Doppler parameter is approximately 10 km/s. However, the detection of this line was questioned already from the first fit in VPFIT, and the fitting problems now further reduce its credibility. The line is included in the COG analysis, but will not be used for further analysis as it might be due to noise or an unidentified absorption feature.

In this run I also included Si II*(1533), which is a tentative detection and it blends in with P II(1533). However, as there are no other unblended detected lines of any of the ions, a fit in VPFIT proves itself difficult and inaccurate. This applies to Si II* in particular, which is the weaker of the two blended absorption features. If the Si II* line is to fit the nearby stronger absorption feature (previously assumed due to P II), it must have a redshift of approximately $z = 3.218$. At the column density obtained for such a fit, the lack of detection of the stronger Si II* lines (particularly Si II*(1265)) is striking and therefore the lines are not likely to be due to Si II*. I therefore choose to use the measurement of Si II* only as an upper limit on the column density. As it is unlikely that either P II(1533) or Si II*(1533) is responsible for this absorption feature, it might be an unidentified line, possibly from an intervening system. The fit of Ni II is carried out on the exact same lines and continuum levels as when b was tied. The only variation is that b now is fixed at $40\mathrm{km/s}$.

5.3.3 The uncertainty of the neutral hydrogen column density

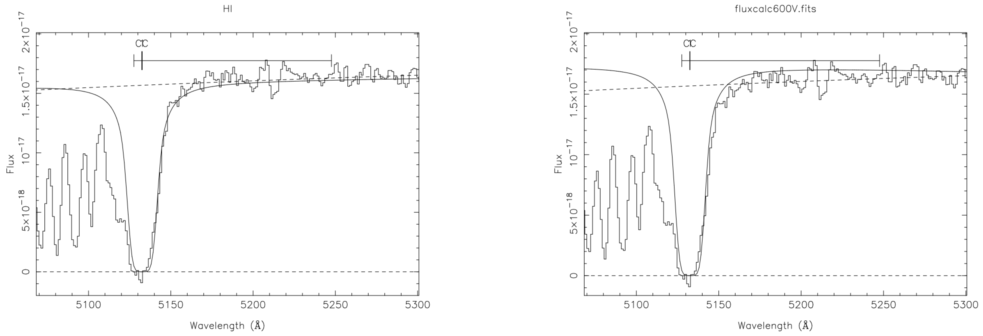

(a) A low continuum fit gives the lowest possible column density, $N(\mathrm{H\ I}) = 19.77$

(b) A high continuum fit gives a higher column density, $N(\mathrm{H\ I}) = 20.09$

Figure 5.5: Illustration of the adopted errors in column density of neutral hydrogen. Over a wavelength range as large as that covered by the Lyα, the uncertainty of fitting the continuum is larger than the uncertainty of fitting the curve in VPFIT.

For very wide absorption features such as H I α, the continuum level will have a significant influence on the resulting column density. This uncertainty is not taken into account in the errors obtained directly from VPFIT. I therefore treat these uncertainties separately by interactively fitting the continuum level. From the resulting variations of the continuum it is evident that the highest likely column density is approximately $\log N(\mathrm{H\ I}) = 20.1$, (Figure 5.5(b)), while the lowest likely column density is $\log N(\mathrm{H\ I}) = 19.8$, (Figure 5.5(a)). These values are respectively 0.1 and 0.2 dex off the adopted value of $\log N(\mathrm{H\ I}) = 20.0$. As this is much larger than the curve fitting error obtained in VPFIT, 0.15 dex is adopted as the uncertainty in $\log N(\text{H I})$. For the other absorption lines which cover a much smaller wavelength range than Lyα, the uncertainties in the curve fitting will likely dominate over continuum uncertainties. For these lines the uncertainties are therefore adopted directly from Table 5.5.

5.4 COG analysis

The dataset analyzed in this thesis has relatively low resolution and high signal-to-noise, see Table 4.5. At this resolution, the lines are not resolved and abundance analysis must therefore be performed on the equivalent width measurements of unresolved metal line transitions. A common way to do this is by performing a multi-ion single-component curve-of-growth (MISC-COG) analysis (Spitzer, 1978). In this analysis one derives an effective Doppler parameter b_{eff} and constrains the column density with the weak, but still potentially saturated transitions. In Section 3.2, the relation between the equivalent width and the column density of an optically thin line was given. Without any a priori assumptions on the optical depth of the line, the relation can be expressed as follows,

$$W_\lambda = \frac{2bF(\tau_0)\lambda}{c},$$

where b is the Doppler parameter, c is the speed of light in vacuum, λ is the rest wavelength. The line center's optical depth, τ_0, and the function, F are given by

$$\tau_0 = \pi^{1/2} e^2 \frac{f\lambda N}{bm_e c} = 1.496 \cdot 10^{-15} \frac{f\lambda N}{b}$$

and

$$F(\tau_0) = \int_0^\infty \big(1 - \exp(-\tau_0 e^{-x^2})\big) dx\,,$$

where f is oscillator strength, N is column density and m_e is the electron mass. The integral was evaluated with QROMO in IDL and plotted with logarithm of W_r/λ against the logarithm of $Nf\lambda$, see Figure 5.6. The degree of curvature of the plotted curve depends on the Doppler parameter, and was fitted to match the observed ions as well as possible. The best fit Doppler parameter is $b = 40 \pm 6$ km/s, where the error corresponds to a difference of unity in χ^2. All error bars are obtained from adding the two reported errors, σ_1 and σ_2, see Tables 5.2 and 5.3. The weakest lines have relatively large error-bars, as evident in Figure 5.6. This is due to the logarithmic nature of the plot, while the errors vary in a more linear manner. The three N I lines are fairly strong, but their error-bars are greatly enlarged by the fact that the lines are poorly defined. This is not surprising as they are located in the Lyα forest. In addition to the N I lines, all but two of the other lines used for the COG analysis are taken with grism 600V. All lines used in the analysis is given in Figure 5.7. As before, the two Ni II lines at λ 1467 Å, are blended and the values given are the total of the two lines.

Table 5.7: **Lines used in the COG analysis**

ion	λ_{rest} (Å)	W_{rest} (Å)	σ_2	grism
Al II	1670.79	1.0422	0.0403	600V
C IV	1550.78	0.1726	0.0269	600V
	1548.20	0.2231	0.0240	600V
C II	1036.34	0.2900	0.1848	1200B
Fe II	1611.20	0.0184	0.0199	600V
	1608.45	0.1822	0.0320	600V
N I	965.04	0.1604	0.0277	1200B
	964.63	0.2941	0.0340	1200B
	963.99	0.2921	0.1525	1200B
Ni II	1502.15	0.0118	0.0239	600V
	1467.76	0.0306	0.0288	600V
	1467.26	a)	a)	600V
	1317.22	0.0421	0.0115	600V
O I	1355.60	0.0536	0.0346	600V
	1039.23	0.5561	0.0353	1200B
S II	1253.81	0.0369	0.0234	600V
	1250.58	0.0116	0.0236	600V
Si II	1526.71	0.9499	0.0370	600V
	1304.37	0.6677	0.0269	600V
	1193.29	1.5468	0.0290	600V
Si II* . . .	1533.43	0.0176	0.0213	600V
Si IV	1402.77	0.0966	0.0270	600V
	1393.76	0.1983	0.0292	600V

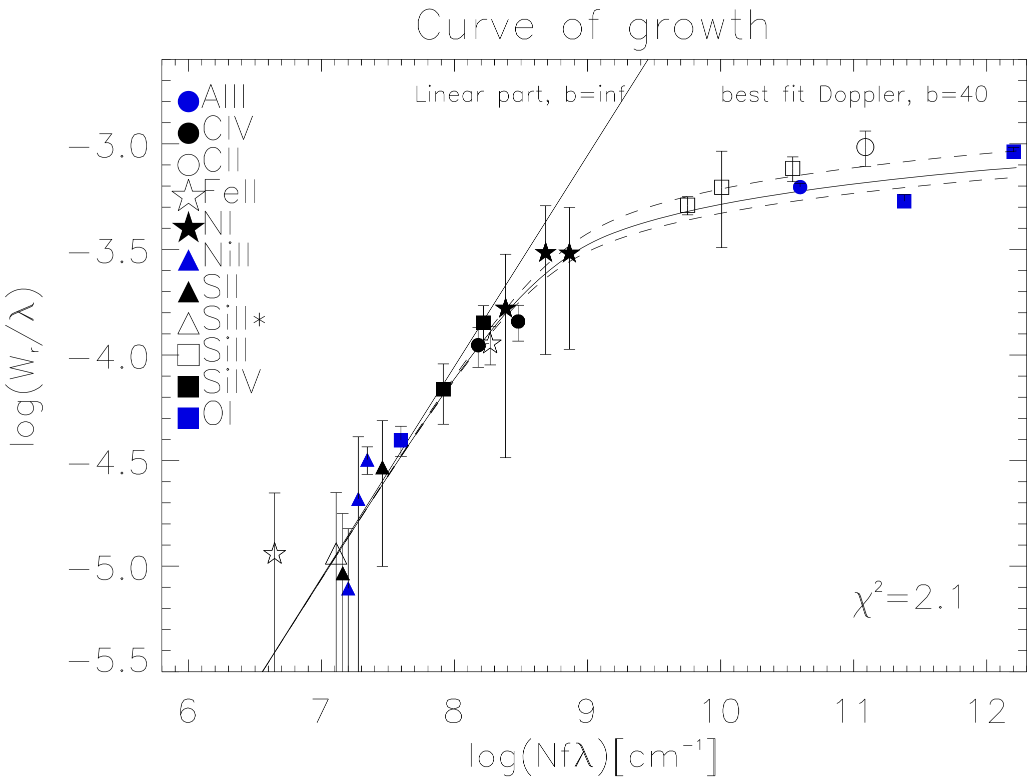

Figure 5.6: MISC-COG analysis of the ions in the ISM of GRB 060526. The symbols are plotted for the best fit column density of that ion, as reported in Table 5.8, b is the best fit effective Doppler parameter in kms^{-1}.

I find that the lines of S II, Ni II and Si II* are well-described by the linear part of the COG, which is to say they are possibly in the optically thin regime. Lines of Fe II, Si IV, C IV and N I are mildly saturated, while most lines of Si II, O I, C II and Al II lie on the flat portion of the COG, i.e. likely in the optically thick regime. In the analysis a single b value is assumed. The derived column densities are listed in Table 5.8.

Recently Prochaska (2006) has looked into the reliability of column densities derived from COG analysis. The gravest point of concern appears to be that for COG analysis with very large b_{eff} values, the technique models transitions with very large equivalent width measurements as being optically thin and adopts the lowest column density conceivable. The result likely underestimates column densities of all of such ions. The effective Doppler parameter in the COG analysis carried out here, is 40 km/s. According to Prochaska (2006) any single component COG analysis with $b_{eff} > 20$ km/s is a sign that the column densities are underestimated. This is because GRB sight lines break into individual components with Doppler parameters < 20 km/s. If one then adopt $b_{eff} \gg 20$ km/s, one will calculate column densities for weaker transitions in the optically thin limit even if these transitions are actually saturated. This is because the b parameter will be given the 'responsibility' for the large equivalent width indicating a smaller column density than what is actually the case. A second signature is that the reduced χ^2 is large. The third and most important signature is that the equivalent widths of weak ions are much smaller in the model than in the measurements. While the reduced χ^2 of the analysis carried out here is not particularly large ($\chi^2 \approx 2.1$), and the only weak ion which has a significantly smaller equivalent width in the model is Fe II, the uncertainties of the derived column densities are still large.

5.5 Adopted column densities

In Table 5.8, I state the adopted column densities, and with the perils of COG analysis in mind, the results from VPFIT with the tied, best fit Doppler parameter are given most weight. Still, the uncertainties of the column densities are significant and this must be kept in mind when deriving and analyzing the results in the upcoming chapter 6.

H I

H I is obtained exclusively from the Lyα line using VPFIT with both the Doppler parameter and the redshift allowed to vary. The uncertainties are discussed in Section 5.3.3.

Al II

The Al II line does not seem to be blended, it is clearly defined and very likely to be saturated. A lower Doppler parameter than the one obtained with this COG analysis will only work to drive the Al II column density to even higher values. However, to obtain lower limits from saturated lines, it is better to use Eq. 3.1 directly, rather than to try a fit, because when fitting you can not be sure that the fit corresponds to the optically thin regime. The COG should in principle also give a lower limit, but as the value obtained is above solar, the 'safer' lower limit given by Eq. 3.1 is adopted.

C II

The COG analysis gives very large column densities for this ion. The solar abundance of C is log $N(\mathrm{C}) = 16.4$, and a value of ~ 18 is therefore very unlikely. The

Table 5.8: **Adopted column densities**

ion	COG	VPFIT(tied b)	VPFIT ($b = 40$)	Eq. 3.1	adopted log N
H I	…	20.01	…	…	20.01 ± 0.15
Al II	15.1	…	…	13.38	> 13.4
Fe II	14.3	14.93 ± 0.47	14.24 ± 0.07	14.14/14.76	14.9 ± 0.5
C II	$\sim$18	…	…	14.76	> 14.76
C IV	14.0	14.20 ± 0.20	14.00 ± 0.05	14.03/13.37	14.2 ± 0.2
N I	15.7	…	…	14.99-15.70	15.7 ± 1.0
Ni II	13.9	13.99 ± 0.16	13.88 ± 0.13	13.33-14.17	<14.0 ± 0.2
P II	…	15.50 ± 0.27	15.26 ± 0.15	16.16	…
O I	18.4	18.64 ± 0.28	18.82 ± 0.21	15.22-18.45	>15.22, <18.6
S II	14.5	14.72 ± 0.23	14.63 ± 0.29	14.39/14.43	14.7 ± 0.3
Si II	15.7	…	…	13.90/14.71	>14.7
Si II*	12.8	…	13.3	…	<12.8
Si IV	13.4	13.56 ± 0.14	13.44 ± 0.07	13.34/13.35	13.5 ± 0.2
Al III	…	…	…	…	<12.8
Zn II	…	…	…	…	<13.2
Cr II	…	…	…	…	<14.0
Mg II	…	…	…	…	<15.9

line C II(1334) is blended with C II*, but only on the wing, and even the very smallest likely EW gives large column densities. The absorption feature might be blended with an unidentified line.

C IV

Values obtained with the different methods are in fairly good agreement with each other. The COG analysis indicate that both lines are slightly saturated and an increase of the Doppler parameter in VPFIT lowers the column density by 0.2 dex. As I am inclined to believe that the Doppler parameter derived in the COG analysis is too high, and therefore view the result as a lower limit. Instead the fit with tied b will be the decisive estimate when adopting a column density.

Fe II

Regarding the Fe II lines where the weaker line did not match the model well, the same inconsistency is found when fitting in VPFIT, see Figure 5.4. I choose to interpret this as a more pronounced saturation in the strongest of the two lines. Again, as the Doppler parameter from the COG analysis likely is too high and the column density derived from COG does not fit for the weakest line. In VPFIT, the weak line gives the same column density regardless of the Doppler parameter and the column density derived from the fit with the lower Doppler parameter is adopted.

N I

In COG the neutral nitrogen lines seem moderately saturated, and the weakest line gives a limit of $\log N(\mathrm{N\ I}) = 15.7$, in accordance with the value derived in the COG analysis. However, the three lines of N I are measured in the 1200B grism and lies in the Lyα forest. Their wings are blended, and equivalent width measurements are uncertain. I have estimated a very large uncertainty of 1 dex, which corresponds to a difference of $\chi^2 = 1$ in the COG analysis.

Ni II

The column densities from the different methods are in good agreement, but as the lines are very weak and many detected only in one of the grisms where they should be visible, the resulting column density must be interpreted as an upper limit. This conclusion is strengthened by the non- detection of Ni II (1742), which at the 3σ level gives $\log N(\mathrm{Ni\ II}) < 14.2$.

P II

As previously mentioned, the column density of P II seems unrealistically large, and the absorption feature is probably due to an intervening system. Therefore, no value is adopted for the column density of P II.

O I

The single line of O I fit in VPFIT did not seem convincing and the other O I lines are in general saturated and blended. The value obtained is regarded as an upper limit. To obtain a lower limit from saturated lines, Eq. 3.1 is used directly, rather than a fit, because when fitting you can not be sure that the fit corresponds to the optically thin regime.

S II

The fits from VPFIT give the same column density regardless of the value of the Doppler parameter. In COG, the S II-ions lie on the linear part of COG and the small variations resulting from changing Doppler parameter in VPFIT also indicate that the lines are not saturated. As usual, the tied-b-run through VPFIT is ascribed most weight when deciding the adopted column density.

Si II

As all lines of Si II are saturated, no value is obtained from VPFIT. As the value obtained from COG is only based on these saturated lines it is rather uncertain. The column density assuming the optically thin regime is therefore adopted as the lower limit column density of Si II.

S II*

As noted in Section 5.2, the column density resulting from VPFIT is not possible to use. The line is blended, making equivalent width measurements difficult, therefore the column density from COG analysis is also very uncertain. The best fit column density from the COG analysis is equal to the column density resulting from Eq. 3.1. As the detection is very uncertain, this is regarded as an upper limit.

Si IV

The COG analysis indicates that the lines are only slightly saturated. The difference of 0.15 dex arising when varying the Doppler parameter in VPFIT, supports this notion. The values from all methods are generally in good agreement with each other.

Al III, Mg II, Cr II and Zn II

Upper limits were calculated from the non-detection of the lines to a level of 3σ, using the lines with the highest oscillator strengths within the spectrum. This is Al III(1855), Zn II(2026), Cr II($2056, 2066$) and Mg II($1240.4, 1239.9$). σ is the error spectrum taken at the same wavelength range. The lines Zn II(2062) and Cr II(2062) were not used as they are blended with each other. Unfortunately, none of the upper limits on Mg II, Cr II or Zn II give good constraints on the abundances because they correspond to super-solar abundances in the ISM of GRB 060526 which is highly unlikely. The limit on Al III, however, is low and can give good constraints on the ratio of Al II/Al III which may be used as an indicator of ionization in the ISM.

Chapter 6

Results

In this chapter we will make use of the column densities obtained in Chapter 5 to derive various properties of the ISM in the host galaxy. We first take a closer look at the H I column density and compare the value from GRB 060526 with other GRB host galaxies. Assuming excitation by collision, the obtained H I column density and the ratio between silicon lines and silicon fine structure lines can in principle be used to estimate the H I volume density (Silva & Viegas, 2002). In these spectra the derived column densities of Si II* and Si II are not accurate enough to give an exact value, but an upper limit is obtained in Section 6.2. In Section 6.3 the observed depletion is compared to familiar depletion patterns in the Milky Way. However, with the few column densities found in Chapter 5, we can not expect to reach any firm conclusions. Using known depletion patterns as comparison, dust depletion corrected metallicity estimates and gas-to-metal ratios may also be derived. Section 6.4 is devoted to extract information from the abundance ratios between various elements, while in Section 6.5 a limit on the star formation rate is derived using the non-detection of Lyα in emission. The last section of this chapter, Section 6.6, deals with possible ionization-effects.

6.1 H I column density

At column densities, $N_{HI} > 10^{20}\mathrm{cm}^{-2}$, the damping wings of the line-profile are well resolved even with a moderate resolution spectrum (FWHM < 5) such as that provided by the 600V grism (Prochaska et al., 2007a). Most GRB absorption systems have very high column densities which are best determined through Voigt profile fitting of the Lyα line of H I at $\lambda 1215$ Å. For GRB 060526, such a fit results in a neutral hydrogen column density of $\log N(\mathrm{HI}) = 20.0 \pm 0.15$. This is in accordance with Jakobsson et al. (2006) who have obtained the same value. GRB060526 therefore does not appear to be a damped Lyα system (DLA), which by definition has $\log N(\mathrm{HI}) > 20.3$. In this manner, GRB 060526 distincts itself from the majority of GRBs which are DLA systems with very high N(H I) values, even compared to QSO-DLAs (Prochaska et al., 2007a). Only a few GRBs have been detected with column densities lower than GRB 060526. According to Jakobsson et al. (2006) there is a clear trend for GRBs with the smallest N(H I) to exhibit very weak (or non-existing) low-ionization lines (e.g. Si II, C II and Fe II) while displaying strong absorption of e.g. Si IV and C IV (GRB 021004, GRB 060607, GRB 060124; Möller et al., 2002; Ledoux et al., 2006; Prochaska, 2006, respectively). However, GRB 060526 has a H I column density comparable to the above mentioned GRBs, but at the same time the spectra show detections of strong Si II and C II lines and intermediate Fe II lines. Si IV and C IV lines are also detected, but these are much weaker than the low-ionization lines. Therefore, while the absorption profiles of e.g. GRB 021004, GRB 060607 and GRB 060124 may lend support to the high-ionization scenario for low N(H I) systems (Jakobsson et al., 2006), GRB 060526 does not seem to fit in with this picture. The high-ionization, low N(H I) scenario is one of the suggestions to explain an over-abundance of low N(H I) GRB systems compared to molecular clouds (Jakobsson et al., 2006) (recall that GRBs are believed to originate in molecular clouds, see Section 2.4). Figure 6.1 illustrates the column density distribution in GRBs and molecular clouds. In this theory, the N(H I) is low because many atoms are ionized into H II. As the column density of H I usually is measured from Lyα, the ionized hydrogen ions will not contribute to the column density. With a large fraction of hydrogen in the ionized state, the gas will become more transparent to photons with energies above 13.6 eV. Therefore higher ionized states of the gas will be more populated. A high N(H I) value may on the contrary suggest that little of the present hydrogen is ionized, and the neutral H I will effectively shield other ions, such as Si II and C II from further ionization. Alternative explanations which do not put direct restrictions on the ionization state of the ISM are that some GRBs are formed by massive runaway stars (Hammer & Flores, 2006), which could explode in regions of relatively low N(H I) or that a significant part of the star formation in molecular clouds takes place at their outer edges (White et al., 1999; Vreeswijk et al., 2006a; Jakobsson et al., 2006).

However, it might not be the origin cloud of the GRB which is responsible for the absorption. Estimates of the distance between the GRB and the absorbers (Vreeswijk et al., 2006a; Prochaska, 2006; Chen et al., 2006) result in a value of order 1 kpc. This is interpreted as the distance where neutral gas can exist without being ionized by the GRB progenitor. The consequence is that any neutral cloud with atomic species typical of the neutral ISM (H I, Fe II, Si II, Zn II etc.) present at less than this distance will likely be ionized into higher ionization stages. As such high ionization stages are not extensively measured, it seems like the cir-

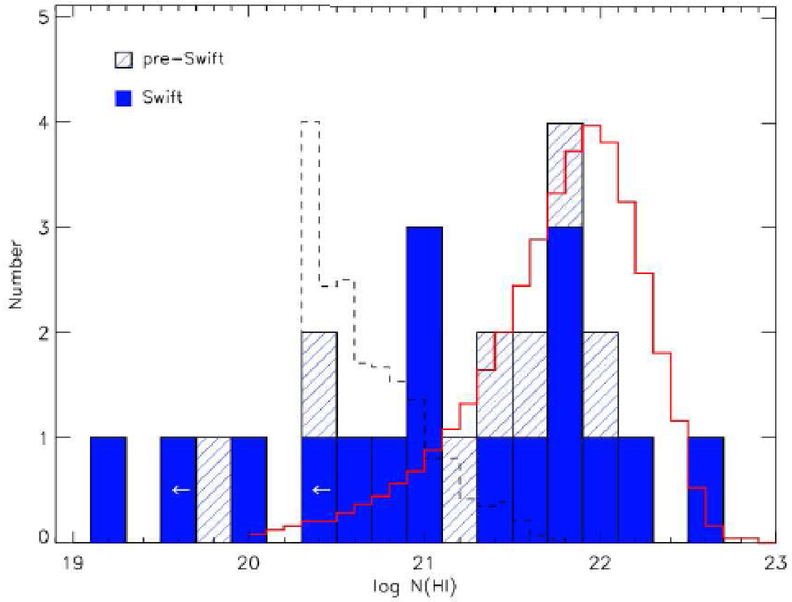

Figure 6.1: H I column densities for the GRB sample (filled histogram) with the predicted distribution if GRBs occurred in galactic molecular clouds (solid histogram). The dashed histogram illustrates the column density in QSO-DLA systems are significantly lower than in GRBs. The figure is taken from Jakobsson et al. (2006).

cumstellar environment around the progenitor does not contribute greatly to the observed absorption lines. The medium responsible for the absorption could either be part of a giant star-forming region in which the GRB was born, H I clouds in the foreground (Vreeswijk et al., 2006a) or generally the ISM of the host galaxy (Prochaska et al., 2007a). Lack of detection of molecular hydrogen also supports this conclusion; the association of GRBs with star- forming regions makes it likely that a large fraction of the gas in the GRB absorption systems is molecular. H_2 give rise to lines in the wavelength range observable for GRBs at $z \gtrsim 2$. In GRB 060526 these lines are located in the Lyα forest which makes it difficult to obtain even upper limits.

6.2 H I volume density

The population of the fine-structure levels is a function of the density of the absorbing medium and the ambient photon-flux intensity (Vreeswijk et al., 2004). The ratio between fine structure lines and 'normal' transitions of the same ion may be used to estimate H I volume density (Silva & Viegas, 2002). However, this calculation rests on several assumptions; first an electron fraction and a temperature must be inferred or assumed. Second, and most questionable, one must assume that the electrons responsible for the fine structures are excited through collisions. There are at least three different mechanisms which can lead to such excitation; collisional excitation, direct excitations by infra-red photons, and fluorescence following excitation by ultraviolet photons, i.e. absorption of a UV photon to an upper level followed by the spontaneous decay to an excited lower level. If the latter mechanism is at work, we cannot use the fine structure abundances to gather information about the temperature and density of a gas, but only the strength of the radiation field (D'Elia et al., 2006). In fact, recent articles by Vreeswijk et al. (2006b) and Prochaska et al. (2006), argue that the UV pumping model is the most important mechanism to excite fine structure lines. For sight lines exhibiting Fe II* absorption, they claim that UV pumping is likely the only mechanism at work.

I will follow through with the H I volume density calculation, but it will only serve as an illustration because even though GRB 060526 has no detected Fe II* lines, the assumption that collisions are responsible for Si II* is likely erroneous. In addition the column density measurements for Si II* and Si II are only limits. I will assume an electron fraction of n_e $10^{-4}n_{HI}$, as this may be expected for a neutral medium in which the electrons primarily come from low-ionization species with an abundance relative to hydrogen of $\approx 10^{-4}$ (Berger et al., 2006b). A temperature of 10^3 K is assumed, as this is also a typical temperature for a neutral medium. The ratio between column density resulting from the fine structure silicon lines and the regular silicon lines - using the upper and lower limits on Si II* and Si II, respectively – becomes

$$\mathrm{SiII}^*/\mathrm{SiII} < 10^{12.80}/10^{14.7} \approx 0.01\,.$$

This is small compared to typical values of $0.1 - 0.2$ (e.g. Berger et al., 2006b; Fynbo et al., 2006a), due to the low abundance of Si II* compared to these papers. A low value of Si II*/Si II indicates a low volume density of H I. Using the estimate from Silva & Viegas (2002, fig.8), $n_{H_0} \approx 10^3\mathrm{cm}^{-3}$ is found. With this value for the H I volume density, the size of the absorbing medium may be estimated by dividing the column density by the volume density to obtain an order of magnitude estimate of the size (diameter) of the absorbing region (Vreeswijk et al., 2004)

$$\begin{aligned} l_{SiII*} &\sim \frac{N(\mathrm{HI})}{n_{\mathrm{HI}}} = \frac{10^{20.0}\mathrm{cm}^{-2}}{10^3\mathrm{cm}^{-3}} \\ l_{SiII*} &\sim 10^{17}\mathrm{cm} = 3.2 \cdot 10^{-2}\mathrm{pc}\,. \end{aligned}$$

The mass of the absorbing cloud may also be estimated (Silva & Viegas, 2002) giving

$$\begin{aligned} M &= m_p N(\mathrm{HI}) l_{SiII*}^2 \\ M &\sim 1.67 \cdot 10^{-27} \cdot 10^{20} \cdot (10^{17})^2 \\ M &\sim 1.67 \cdot 10^{27}\mathrm{kg} = 8.4 \cdot 10^{-4} M_\odot\,, \end{aligned}$$

where m_p is the proton mass, and l_{SiII*} is the diameter of the Si II* absorbing region. Due to the low column density of hydrogen, the mass is orders of magnitudes smaller than those calculated in e.g. Berger et al. (2006b) and Fynbo et al. (2006a). As the Si II*/Si II ratio is an upper limit, so will in principle these values be, but if the Si II* ions are only partly associated with the entire H I and Si II column, the size and mass estimates would be pushed to higher values (Vreeswijk et al., 2004). Again, I remind the reader that these calculations are not valid if UV pumping is alone responsible for the excitations of the Si II* lines. If a combination of effects are responsible, the derived values are upper limits.

Table 6.1: **[M/H] ratios for GRB 060526**

Element		Equation 6.1		Abundance
[Si/H]	>	$14.7 - 20.01 - 7.51 + 12.00$	=	-0.82
[Fe/H]	=	$14.9 - 20.01 - 7.45 + 12.00$	=	-0.56 ± 0.5
[S/H]	=	$14.7 - 20.01 - 7.14 + 12.00$	=	-0.45 ± 0.3
[Ni/H]	<	$14.0 - 20.01 - 6.23 + 12.00$	=	-0.24
[Zn/H]	<	$13.2 - 20.01 - 4.65 + 12.00$	=	0.54
[Al/H]	>	$13.4 - 20.01 - 6.37 + 12.00$	=	-0.98
[Cr/H]	<	$14.0 - 20.01 - 5.64 + 12.00$	=	0.35
[Mg/H]	<	$15.9 - 20.01 - 7.53 + 12.00$	=	0.36

6.3 Metallicity and dust depletion correction

Metallicity is a measure of the amount of metals (as astronomers define metals) [1] in an object of study. The metallicity of the sun is approximately 1.6 percent by mass. For other stars, the metallicity is often expressed as [M/H], which represents the logarithm of the ratio of a star's abundance of the metal M compared to that of the sun. The formula for the logarithm is expressed thus

$$[\mathrm{M/H}] = \log N(\mathrm{M})/N(\mathrm{H}) - \log N(\mathrm{M})_\odot/N(\mathrm{H})_\odot\,. \tag{6.1}$$

It is usual to assume that the higher ionization states of hydrogen are negligible, i.e. $\log N(\mathrm{H}) \approx \log N(\mathrm{HI})$. Table 6.1 shows the abundances, [M/H], of the absorption system around GRB 060526 calculated from the adopted column densities in Table 5.8. The values adopted as solar abundances (third term in Eq. 6.1) are taken from Asplund et al. (2005). As a simple measure of metallicity, [Fe/H], [S/H] or [Zn/H] is often used. The advantage of using zinc rather than iron is that while iron is known to be heavily depleted onto dust, zinc tends to stay in the gas-phase. Dust does not contribute to the observed column density, and metallicities based on iron may therefore be under-estimated. However, as zinc has an unclear nucleosynthetic origin (Hoffman et al., 1996), it should be treated with caution and in any case the data from GRB 060526 give no adequate constraints on the zinc abundance. As can be seen, the upper limit on the zinc abundance corresponds to a metallicity above solar and therefore constrains the metallicity poorly. Sulpher is only mildly depleted onto dust and can therefore be a good alternative.

---

[1] All elements heavier than helium are defined as metals in astronomy. The differing origin of the elements give rise to this division line; hydrogen and helium were created in the Big Bang, while all heavier elements have been created inside stars and then ejected into space.

Using sulphur and iron abundances, respectively, we calculate the first metallicity estimates,

$$Z/Z_{\odot} = 10^{-0.45}/10^{0} = 0.35 \tag{6.2}$$
$$Z/Z_{\odot} = 10^{-0.56}/10^{0} = 0.28\,. \tag{6.3}$$

However, to obtain a more thorough measurement of metallicity, one should consider all detected heavy elements and correct for dust depletion affects. Dust may cause any measurement to underestimate the true number of atoms. This may effect various elements differently, since they do not all condense onto dust grains at the same temperature. While e.g. Fe, Cr and Ni easily condense into dust (are depleted), O, P, Ar, S, Si and Zn are only mildly depleted. The question then is whether the measured abundances of elements in high redshift GRB host galaxies also have been modified by differential dust depletion. Assuming particular depletion patterns can in turn be used to correct the measured gas-phase abundances (Savaglio et al., 2000). To obtain accurate estimates with this method, more than the two elements obtained for GRB 060526 should be used. In addition, the errors on Fe and S (see Table 5.8) are large, and Si only has a lower limit. Therefore for the analysis of GRB 060526, there is not enough well determined data points to properly fit a depletion pattern. Too few and inaccurate abundance measurements are prevalent problems with low resolution data. However, I will use the existing values on Fe and S, and assume a value of Si II of 15 to illustrate the method. This leads to the abundances used in Figure 6.2, [-0.45, -0.52 ,-0.56] for S, Si, and Fe, respectively.

The mean abundance ratios in GRB host galaxies are similar to those of warm halo clouds and Small Magelanic Cloud (SMC) absorbers, i.e. fairly low metallicities and modest depletion (Welty et al., 1997). Therefore the prevailing conditions in GRB host galaxies and those in warm halo clouds and SMC absorbers cannot be very dissimilar. As depletion patterns for the SMC are not well determined, Savaglio et al. (2000) have used the depletion patterns identified for the Milky Way and applied these on DLA systems. I will apply the same depletion patterns on GRB 060526. The identified patterns are: warm halo (WH), warm halo + disk (WDH), warm disk (WD), and cool disk (CD) clouds (Savage & Sembach, 1996). The dust-to-metal ratio may be different from the Milky Way, and this ratio is therefore modified to obtain the best match to observations. Using the relation (6.1) for the elements, Fe, Si, and S (see Table 6.1 for values), four different depletion patterns are fit. The calculations follow the method outlined by Savaglio et al. (2000). For each detected element, X_i, for which a robust column density is measured, two quantities are considered,

$$\delta x_i = [X/H]_{GRB} - log\left(\frac{Z_{GRB}}{Z_\odot}\right) \tag{6.4}$$

$$\delta y_i = log\left(1 + \frac{k_{GRB}}{k_J}(10^{\delta x_i^J} - 1)\right), \tag{6.5}$$

where J denotes the different depletion patterns WH, WDH, WD, and CD, [X/H] is calculated from the observed column densities and Eq 6.1 and $\delta x_i^J = [\mathrm{X/H}]_J$ is the observed depletion of element X_i in the specific cloud J. The two unknowns are the GRB metallicity compared with solar, $Z_{GRB}/Z_\odot$, and the dust-to-metals ratio compared with that of the J-type clouds, k_{GRB}/k_J. To fit the depletion pattern to the observed abundances, the abundances must be collectively modified up to the solar abundance levels (Eq. 6.4). At the same time, each depletion pattern is modified to allow a different dust-to-gas ratio in the GRB (Eq. 6.5). The values of $Z_{GRB}/Z_\odot$ and k_{GRB}/k_J that minimize the reduced χ^2,

$$\frac{\chi^2}{dof} = \frac{1}{N-2}\sum\left(\frac{\delta x_i - \delta y_i}{\log X_i}\right)^2, \tag{6.6}$$

give the best solution to the problem. Here $N - 2$ is the number of degrees of freedom (dof) and $\sigma(\log X_i)$ is the error on the measured column density. It is worth noting that this makes χ^2 very sensitive to the column density errors. If the GRB has two or less elements, χ^2 cannot be calculated as there are two degrees of freedom in the equation set. The abundance measurements, [X/H], in WH, WDH, WD, and CD are taken from Savage & Sembach (1996). Figure 6.2 shows the best fits of the various depletion patterns for the three elements measured in GRB 060526. Metallicities and dust-to-metal ratios are fit interactively. The sensitivity of χ^2 to the errors on column density leads to a small χ^2 even if the depletion pattern is not a very good fit to the data points. This usually implies that the errors are overestimated. To obtain good constraints, accurate column densities of NiII and preferably some of the other ions, Cr, Mn or Mg are essential. The upper limits on Cr and Mg obtained for GRB 060526 are not very useful as they correspond to abundance ratios, [M/H], of 0.35 and 0.36 respectively - i.e. much higher than solar. In the spectra reduced for GRB 060526 the only Mn lines lie in the Lyα forest, which makes it impossible to obtain even upper limits. As there are so few data points and large uncertainties, it is not really possible to conclude which depletion pattern is the best fit to the data. With the abundances used, the CD depletion pattern is clearly the worst fit, while the WH is marginally better than the WDH pattern. But I stress that slight variations in the abundances, well within the error estimates, are sufficient to change these fits significantly. It can

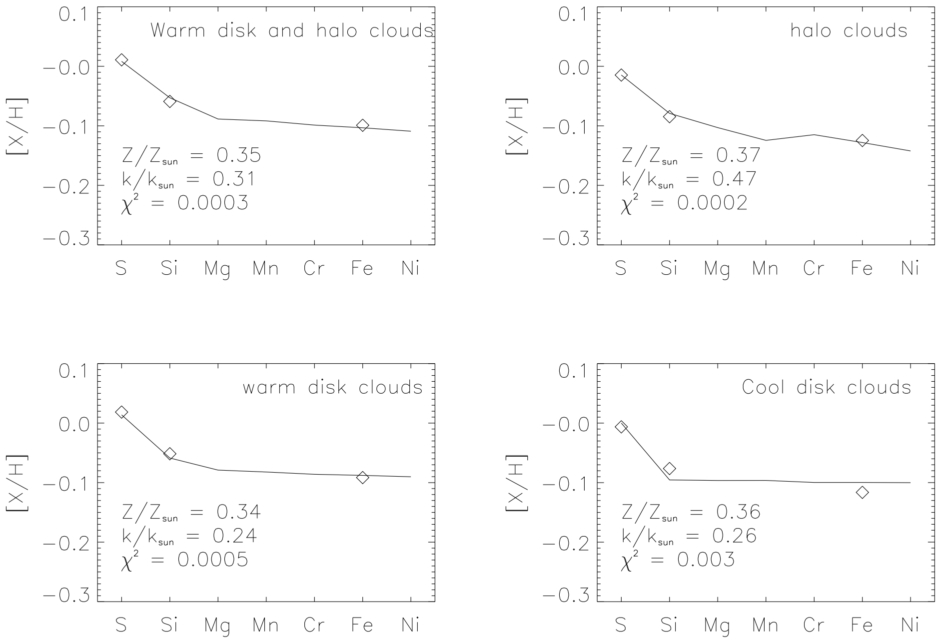

Figure 6.2: Depletion pattern for the host galaxy of GRB 060526 using the inferred columns of sulfur, silicon, and iron. The metallicity, dust-to-metal ratio, and the best-fit χ^2 are also given.

be mentioned that the warm halo (WH) depletion pattern is often found to be the best fit to data (GRB00926, GRB990123 and GRB010222; Savaglio et al., 2000), while the CD depletion pattern the poorest (Berger et al., 2006b; Savaglio et al., 2000). Even if no specific depletion pattern can be established, a general picture of the metallicity and dust to gas ratio emerges. The metallicity of the four models only ranges from $Z/Z_{\odot} = 0.34 - 0.37$, the WH pattern gives $Z/Z_{\odot} = 0.37$. Only using iron and sulphur as indicators of metallicity, without taking dust-depletion into account, we get for iron $Z = 0.28 Z_{\odot}$ for $\log N(\mathrm{Fe}) = 14.9$ which is clearly lower than the estimate obtained in the fit. This is as expected, since dust depletion would tend to lower the metallicity when using iron, while it is accounted for in the dust-depletion corrected estimate, see Figure 6.2. For sulphur the metallicity estimate gave $Z/Z_{\odot} = 0.35$, only slightly less than the metallicity found with depeltion-correction as sulpur is only mildly depleted onto dust grains. The metallicity is high compared to other GRBs at similar redshift, see Table 6.2. The dust to metal ratio varies from $k/k_J = 0.24 - 0.47$, with the best fit depletion pattern, WH, representing the largest estimate. Still, these are all low ratios, indicating little dust depletion. If the tentative detection of a high Ni II abundance is real, this would confirm the small dust depletion effects, as it is easily depleted onto dust grains.

Knowing the dust-to-gas ratio and the metallicity, one can estimate the obscuration of the GRB due to dust distributed along the line of sight, following the calculations of Savaglio et al. (2003) and Berger et al. (2006b). I will use the dust-to-gas ratio (k/k_{WH}) and metallicity (Z/Z_{WH}) of the best fit depletion pattern, WH, but keep in mind that these are rough estimates based on an assumed abundance of silicon. The amount of extinction varies as a function of wavelength such that it is highest at short wavelengths and lowest at longer wavelengths. The extinction in the V-band, due to dust, can be approximated by (Savaglio et al., 2003)

$$A_V = A_{V_{\odot}} \frac{k}{k_{WH}} \frac{Z}{Z_{\odot}} \frac{N(\mathrm{H\,I})}{10^{21}\mathrm{cm}^{-2}}\,, \tag{6.7}$$

where A_V is the extinction in the V-band and $A_{V_{\odot}}$ is the typical extinction value in the solar neighborhood for a column density of $\log N(\mathrm{H\,I}) = 20.0$. The solar extinction can be estimated through relation (6.8), obtained from studies using ultraviolet spectroscopy of reddened stars and X-ray scattering halos in the Milky Way

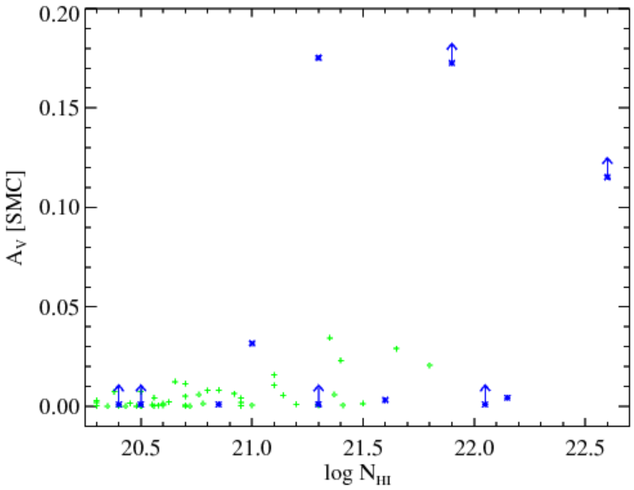

Figure 6.3: Visual extinctions, A_V for GRB-DLA (blue) and QSO-DLA (green) sightlines as calculated by Prochaska et al. (2007b).

$$\begin{aligned} \frac{N_H}{A_{V_\odot}} &\approx 1.8 \cdot 10^{21} \text{atomscm}^{-2}\text{mag}^{-1} \\ A_{V_\odot} &\approx \frac{10^{20.01}}{1.8 \cdot 10^{21}} \text{mag} \\ A_{V_\odot} &\approx 0.06 \text{mag}\,. \end{aligned} \tag{6.8}$$

When substituting $A_{V_\odot}$ from Eq. 6.8 into Eq. 6.7 and using the metallicity and dust-to-metals ratio from the WH depletion pattern, we get

$$\begin{aligned} A_V &\approx 0.06 \cdot 0.47 \cdot 0.3 \cdot \frac{10^{20.01}}{10^{21}} \text{mag} \\ A_V &\approx 8.7 \cdot 10^{-4} \text{mag}\,. \end{aligned} \tag{6.9}$$

In short, the extinction depends on the metallicity, dust depletion and H I column density. The resulting extinction for GRB 060526 is low. As Figure 6.3 shows, low extinctions are common both in QSO-DLA sightlines and in GRB-DLAs, but GRB-DLAs seem to have a more bimodal population with several extinction values approaching $A_V = 0.2$ mag.

Metallicity

The possible metallicity-bias in GRBs is a hot subject of debate. The value of $Z = -0.45 \pm 0.3$ (based on the S II abundance) estimated for GRB 060526 is among the higher values reported, particularity taking its high redshift into account. Note that this metallicity is in accordance with the value obtained using the Fe II abundance instead of S II. However, a few GRBs are reported with up to twice this metallicity (in percent of solar), see Table 6.2. At a metallicity of $Z/Z_{\odot} \approx 0.35$, GRB 060526 balances the theoretical upper limit set on the progenitor metallicity at $Z/Z_{\odot} = 0.3$ from calculations by Woosley & Heger (2006). However, several different metallicity limits have been set, from about one fifth solar (Stanek et al., 2006; Yoon & Langer, 2005) and up to one half solar (Wolf & Podsiadlowski, 2007). The latter finds that using the luminosity-metallicity $(L - Z)$ relation, GRB models requiring less than $\sim$ 0.5 $Z_{\odot}$ are ruled out because they require fainter hosts than what is observed. In addition several GRBs have been measured to have metallicities above the $0.3Z_{\odot}$ limit and the need for such low metallicities might therefore be a weakness of the WR -progenitor model. On the other hand, recent papers (Vreeswijk et al., 2006a; Prochaska et al., 2007a; Watson et al., 2007) find evidence that the abundances measured from absorption lines in afterglow spectra do not origin at the GRB birth place, but $\sim$kilo-parsecs away in foreground clouds and the ISM. The metallicity measured from the absorption spectra would then not be directly representative for the environment immediately surrounding the GRB progenitor. This may seem like an opportunity for progenitors requiring low metallicities to evade the high metallicity observations, but currently there is no reason to expect that the ISM value would systematically overestimate the GRB progenitor metallicity (Prochaska et al., 2007b). Observationally, it is clear that if a metallcity-bias does exist, it is only of importance in low redshift hosts where metals are more abundant; while the hosts of GRBs at $z < 0.2$ appear to have metallicities at the low end of the distribution for local galaxies (Stanek et al., 2006), at least some GRBs at $z \sim 2$ occur in the most metal-enriched galaxies at that redshift (Berger et al., 2006a).

In the case of GRB 060526, conclusions regarding metallicity should not be drawn too decisively. Lower column densities of the Fe II and S II ions can be found if one chooses to lower the continuum level slightly or to give more weight to the abundances found using COG analysis. This would then lead to lower metallicities which would not be in conflict with the $0.3Z_{\odot}$ limit. On the other hand, dust extinction might be more severe than the estimate used in this thesis, and in that case the intrinsic metallicity could be higher than the value adopted here.

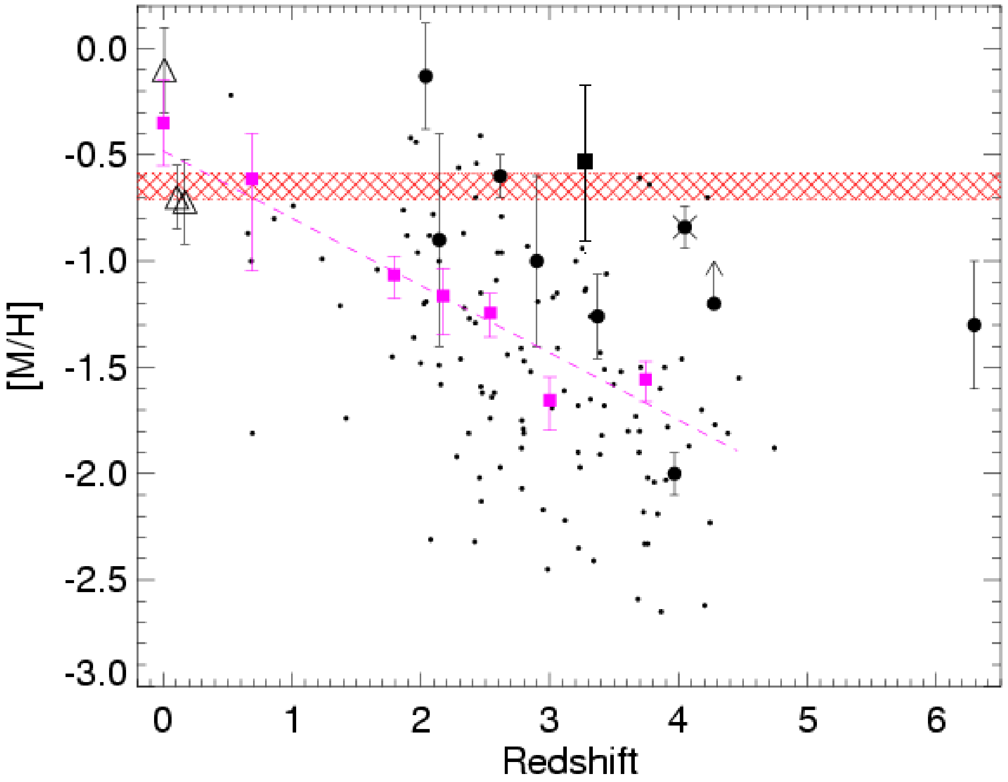

Figure 6.4: Metallicity as a function of redshift for different classes of objects. The black circles are the measurements for GRBs from Table 2. The open triangles show the metallicity of three low-z GRB host galaxies (Sollerman et al. 2005). The squares and the dashed line represent the column density weighted metallicity evolution derived by Zwaan et al. (2005, Fig.22). The small dots with no error-bars are measurements for 121 DLAs from Prochaska et al.(2003). The hatched region indicates the metallicity above which GRBs cannot form in the collapsar models (Woosley, 2005). The metallicity obtained for the ISM around GRB 060526, represented by the black square, is relatively high. The uncertainty is calculated from $\sigma = \sqrt{\sigma_S^2 + \sigma_H^2} = \pm 0.34$. The values of σ_S and σ_{HI} are found in Table 5.8. This figure is taken from Fynbo et al. (2006a).

GRB		Metallicity	$\log N(\mathrm{H\ I})$	z	Ref.
980425	...	$= -0.10$	...	0.0085	11
000926	[Zn/H]	$= -0.13 \pm 0.25$	≈ 21.3	2.038	1,15
011211	[Si/H]	$= -0.90 \pm 0.5$	20.4 ± 0.2	2.142	2
020127	...	$=\approx -0.30$	...	≈ 1.9	12
030323	[S/H]	$= -1.26 \pm 0.2$	21.90 ± 0.07	3.372	3
050401	[Zn/H]	$= -1.0 \pm 0.4$	22.6	2.899	4
050505	[S/H]	> -1.2	22.05 ± 0.10	4.275	5
050730	[S/H]	$= -2.0 \pm 0.2$	22.1 ± 0.1	3.968	6,7
050820	[Si/H]	$= -0.6 \pm 0.1$	21.0	2.615	8
050904	[S/H]	$= -1.3 \pm 0.3$	...	6.295	9
060206	[S/H]	$= -0.84 \pm 0.10$	20.9 ± 0.1	4.048	10
060526	[S/H]	$= -0.45 \pm 0.3$	20.0 ± 0.15	3.2216	13
060526	[Fe/H]	$= -0.56 \pm 0.5$	20.0 ± 0.15	3.2216	13
060714	[Si/H]	> -1.35	21.8 ± 0.1	2.71	14

Table 6.2: **GRB metallicities from the literature.** References in the table are [1] Savaglio et al. (2003), [2] Vreeswijk et al. (2006a), [3] Vreeswijk et al. (2004), [4] Watson et al. (2006), [5] Berger et al. (2006b), [6] Starling et al. (2005), [7] Chen et al. (2005), [8] Ledoux et al. (2005), [9] Kawai et al. (2005), [10] Fynbo et al. (2006a). [11] Sollerman et al. (2005), [12] Berger et al. (2006b) [13] this work, [14] Jakobsson et al. (2005), [15] Fynbo et al. (2001).

6.4 Relative abundances

Relative abundances are measured by comparing the gas-phase column densities of pairs of low-ions under the assumption that ionization corrections are small,

$$[\mathrm{X/Y}] = logN_{x_i} - logN_{Y_i} - log(X/Y)_{\odot}\,. \tag{6.10}$$

This assumption is further discussed in Section 6.6, but for now it suffices to say that low ionization ions and high ionization ions (typically triple or higher ionization stages) are thought to origin at different places. Low ionized ions are expected in H I regions (Vladilo et al., 2001), while higher ionization stages, such as Si IV and C IV may originate closer to the progenitor. Because the observed ratios represent gas-phase abundances, the values reflect a combination of the underlying nucleosynthetic pattern and the effects of differential depletion onto dust grains.

6.4.1 α/Fe ratio

The α-element, (Ne, Mg, S, Si, Ca, Ti, Ar and O) are synthesized by α-capture in SNeII and the abundances of such elements in the ISM are indicators of the enrichment history of the medium. Type II supernovae create large amounts of the alpha elements with respect to iron (e.g. Woosley & Weaver, 1995), while Type Ia supernovae create mostly Fe-peak elements (Cr, Mn, Fe, Co, Ni, and Zn). As SNe Type Ia work on a longer time-scale than SNe Type II, the α to Fe-peak ratio is expected to rapidly attain super-solar values in a chemically less mature system. This ratio should decrease as cosmic time proceeds (e.g. Prochaska et al., 2007a). In GRB 060526, the ratio can be subject to dust depletion effects. Unfortunately, there is no element in the Fe peak which is non-refractory. [2] As zinc tends to stay in the gas phase, it is often used instead of iron, but the nucleosynthetic origin of zinc is uncertain (Hoffman et al., 1996), and the exchange could therefore cause large systematic errors (Prochaska et al., 2007a). No exact column density is obtained on zinc in the ISM of GRB 060526, and as there seems to be very little dust depletion in this system, iron will be used. As there are no Mg or Ar lines in the spectrum of GRB 060526, and O I and Si II only have limits, S is adopted as reference for α,

$$[\mathrm{S/Fe}] = 14.7 - 14.9 - 7.14 + 7.45 = 0.11\,. \tag{6.11}$$

---

[2] A refractory element is any element which condenses from a gas at high temperatures. A non-refractory elements is in this context an element which stay in gas form – i.e. do not condense onto dust grains – even at relatively low temperatures.

This is a low α/Fe ratio compared to other GRBs, see e.g. Prochaska et al. (Fig. 5 2007b). However, note that the GRBs displayed are DLA-GRBs and in general have much larger column densities than GRB 060526. From the nucleosynthetic viewpoint, one expects enhanced α/Fe in GRB host galaxies because the high specific star formation rates of these galaxies imply ages that are young compared to the time-scales for Type Ia enrichmenta and therefore less iron has been supplied to the ISM (Prochaska et al., 2007a). In addition, there might be dust depletion, enhancing the ratio further. As we have looked at in Section 6.3, GRB 060526 seems to have little dust depletion, with a dust-to-gas ratio of only $\sim 0.3k_J$. The [α/H] ratio is high, [S/H] = -0.45, and indicates a relatively evolved system and thus, possibly longer time-scales allowing significant amounts of iron-peak elements too have formed. The low α/Fe ratio also signalizes that the nucleosynthetic enhancement by massive stars is relatively low compared to other GRBs, and a lower specific star formation rate than typical GRB hosts might be expected.

6.4.2 The N/α ratio

Another abundance ratio of particular interest in terms of nucleosynthesis is N/α. N is believed to be produced primarily by intermediate mass stars when they reach the astymptotical giant brach (AGB) after their time at the main sequence is over (Meynet & Maeder, 2002). The N/α ratio provides a diagnostic of the star formation history of the galaxy, especially at early times. N is a non-refractory element and the only serious systematic uncertainty is the ionization corrections. No particular trend has been found amongst GRBs so far, indicating that the host galaxies have experienced a diverse range of star formation (Prochaska et al., 2007a). Chemical evolution models predict the production of nitrogen in the CNO cycle in stellar interiors to have two different origins: While primary N is produced in intermediate-mass stars $(3 - 8M_{\odot})$, without dependence on the initial metal content, secondary nitrogen is also produced in stars of any mass but with an initial supply of heavy elements. The net result is that the N/O ratio should be independent of O/H for primary N while N/O $\sim$ O/H for secondary N (Lopez et al., 2002; Lu et al., 1998). It is also possible to use the ratios of N/S or N/Si instead of O (Lopez et al., 2002). Unfortunately, the column density of N I measured for the ISM around GRB 060526 is very uncertain and can not be used to constrain nucleosynthetic patterns.

6.4.3 Atomic carbon

In the galaxy, atomic carbon (C) is a good tracer of cold, dense gas. As carbon has a first ionization potential below 13.6 eV, it is generally found in the first ionized state, C II. However, in cold and dense regions, the recombination rate is large enough that cold clouds frequently show detectable absorption from C I regions (e.g. Prochaska et al., 2007a). For standard galactic ISM conditions, the C I/C II ratio is $\approx 10^{-2}$ in the cold neutral medium, and decreases to $\approx 10^{-4}$ in the warm neutral medium (Prochaska et al., 2007a). Generally, very low C I/C II ratios imply gas with density less than 10 particles per cm^3. For GRB 060526, C I is not detected, and therefore only an upper limit can be obtained; $N(\mathrm{C\,I}) < 4.0 \cdot 10^{13}\mathrm{cm}^{-2}$. In most GRBs the C II transitions are too saturated to provide even a valuable lower limit, which also seems to be the case here. Following Prochaska et al. (2007a), an approximation to C II is therefore inferred from the α/H abundance and $N_{H\ I}$ value,

$$\begin{aligned}\log N(\mathrm{C\,II}) &= [\alpha/\mathrm{H}] + \log N_{H\ I} - 12 + 8.1\\ &= -0.45 + 20.01 - 4\\ &= 15.66\,.\end{aligned}$$

The assumed enhancement of α elements relative to C, α/C, should be added on the right hand side of the equation. In Section 6.4.1 a modest α enhancement was inferred for GRB 060526, only ~ 0.1 dex - giving 8.1 instead of 8. The upper limit on the C I/C II ratio then becomes

$$\mathrm{C\,I/C\,II} < \frac{4 \cdot 10^{13}}{10^{15.66}} = 9 \cdot 10^{-3}\,. \tag{6.12}$$

This value is only slightly less than in standard galactic ISM conditions, which is about the upper limit of expected values, see Figure 6.5 Since C I has many fairly strong lines in the range of the 600V grism and none of these are detected, I suspect that the value for C I is in fact quite a bit smaller than the upper limit given.

6.4.4 The odd-even effect

The odd-even effect refers to the under-abundance of odd-Z elements relative to even-Z elements of the same nucleosynthetic origin. The effect is used to discriminate between dust depletion and pure SN Type II enrichment. Two good elements to use are iron (Fe) and manganese (Mn) since iron is more prone to dust depletion than manganese in a variety of ISM environments. However, Mn is not detected in the spectra of GRB 060526 and as the only line in the wavelength range are in the Lyα forest no upper limit is obtained.

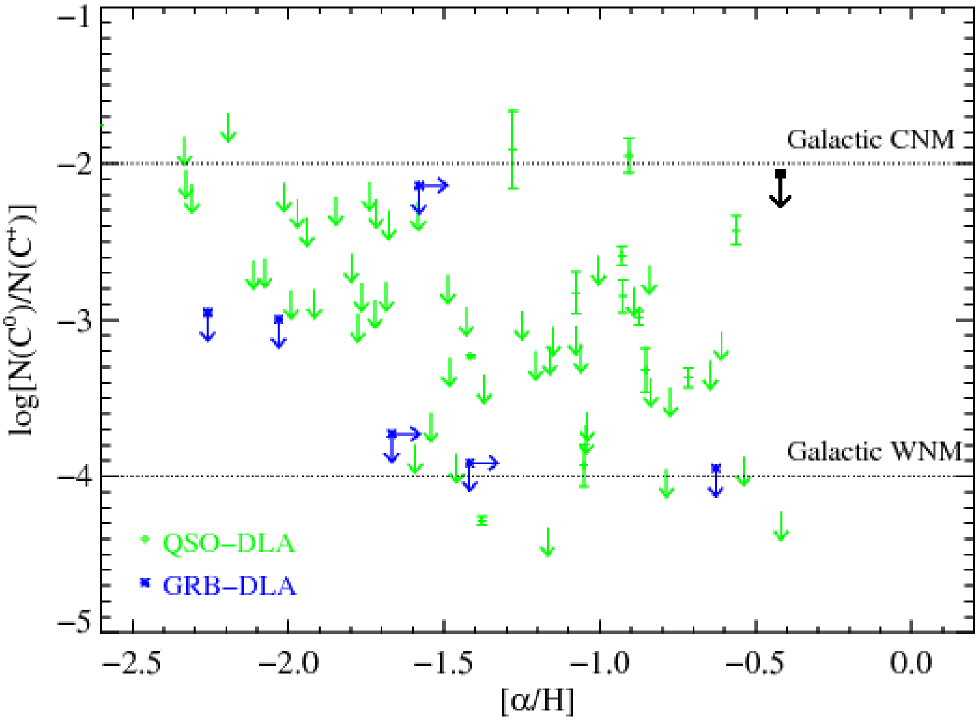

Figure 6.5: The C I/C II ratio plotted against metallicity for QSO-DLAs, GRB-DLAs, and GRB 060526 (black square). The C I/C II ratio of GRB 060526 is just below that of the galactic cold neutral medium, but note that this is only an upper limit. The figure is taken from (Prochaska et al., 2007b).

6.4.5 Si IV and C IV

While the observed column densities of low ionized ions typically originate at a distance from the GRB progenitor, highly ionized ions such as Si IV and C IV are more likely to originate in the circumstellar medium of the progenitor. Circumstellar absorption lines in GRB afterglow spectra may allow determination of the main properties of the Wolf-Rayet star progenitors (van Marle et al., 2005). This may be done by comparing detailed simulations with spectra showing resolved velocity components. Both Si IV and C IV are clearly detected in the spectrum of GRB 060526 (although significantly weaker than the singly ionized states of the same ions). These absorption features are best fitted at a redshift of $z = 3.2217$, i.e. a slightly higher redshift fit than for the low ionization ions at $z = 3.2213$.

Calculations of stellar winds from massive stars done by Leitherer & Lamers (1991) show that while strong C IV is almost always present, the presence of Si IV lines depend sensitively on the star's mass and metallicity. Thus, increasing metallicity shows itself by an increased Si IV abundance and a higher ratio of the EWs of Si IV and C IV. Note that for this ratio to be reliable, the saturation effects on the lines must be small. Whether this conditions is satisfied for the lines detected here is not certain. The Si IV absorption in GRB 060526 is relatively strong compared to the C IV absorption, supporting the impression of a high metallicity environment also in the immediate environment around the progenitor.

$$EW(Si\ IV)/EW(C\ IV) \approx 0.3/0.4 = 0.75\,.$$

For comparison, analysis of GRB 050505 by Berger et al. (2006a) yields a EW ratio of < 0.1, from which they infer a metallicity (using Leitherer & Lamers, 1991, Figure 10,12) of $Z \lesssim 0.1 Z_\odot$. The high ratio found for GRB 060526 signifies both a higher metallicity and higher mass than the progenitor of GRB 050505. However, this result is only valid provided that the Si IV and C IV lines are not heavily saturated. The COG analysis imply a mild saturation on these lines, but to what extent this affects the EW ratio we cannot predict.

6.5 Limits on star formation

An estimate on the star formation in the host galaxy can be obtained from recombination lines. Kennicutt (1998) shows that the most dramatic change in the spectrum with galaxy type is a rapid increase in the strengths of the emission lines. Only stars with masses of $M_\odot > 10$ and lifetimes greater than 20 Myr contribute significantly to the ionizing flux, so the emission lines provide a nearly instantaneous measure of the SFR, independent of the previous star formation history. The conversion between flux and star formation rate is given by Kennicutt (1998)

$$SFR(M_\odot yr^{-1}) = L(H\alpha) \cdot 7.9 \cdot 10^{-42} \text{ergs/s}\,, \tag{6.13}$$

where SFR is the star formation rate in solar masses per year, L(Hα) is the emitted luminosity in Hα, and the last constant is the conversion factor. Knowing the redshift of the burst, the flux can be converted into luminosity using the luminosity-distance relation

$$L_e = \Psi_0 \cdot 4\pi d_L^2 = \Psi_0 \cdot 4\pi d_{prop}^2 (1+z)^2,$$

where L_e is the emitted luminosity, Ψ_0 is the flux, and the luminosity distance d_L equals the proper distance d_{prop} times $(1+z)$. The limit on the flux obtained for GRB 060526, steams from the non-detection of Lyα in emission at approximately 1215 Å e.i. at the bottom of the H Iα. Recall from Section 4.4.3 that the spectra needed to be renormalized to obtain an accurate flux calibration. After this renormalization, the continuum was raised by 76 %. As the signal-to-noise is assumed to be unchanged, the error-spectrum should also rise by 76%. Therefore, the same rise is applied to the detection limit of the flux (which is as usual measured from the error-spectrum) used for the SFR-calculations of this section. Measuring over two resolution elements gives a flux limit of $3.9 \cdot 10^{-18}$ ergs. Using standard cosmology with $H_o = 72$ km/s/Mpc, $\Omega_m = 0.7$ and $\Omega_\Lambda = 0.3$, this may be written as

$$d_{prop} = \frac{c}{H_0} \int_0^z \frac{dz'}{\sqrt{\Omega_{m0}(1+z')^3 + 1 - \Omega_{m0}}}\,, \tag{6.14}$$

giving a proper distance of $2.0 \cdot 10^{26}$ m. The flux then corresponds to a luminosity of

$$\begin{aligned} L_e &= 3.9 \cdot 10^{-18} \cdot 10^4 \cdot 4\pi (2.0 \cdot 10^{26} \cdot 4.221)^2 \text{ergs/s} \\ &= 3.5 \cdot 10^{41} \text{ergs/s}\,. \end{aligned}$$

Inserting this in Equation 6.13 we get

$$\begin{aligned} SFR(\mathrm{M_\odot yr^{-1}}) &< 3.5 \cdot 10^{41} \cdot 7.9 \cdot 10^{-42} \mathrm{M_\odot yr^{-1}} \\ &< 2.8 \mathrm{M_\odot yr^{-1}}\,. \end{aligned} \tag{6.15}$$

The limit obtained, SRF $< 2.8 M_{\odot} \mathrm{yr}^{-1}$, is similar to that derived by Berger et al. (2006b) for GRB 050505 and by Penprase et al. (2006) for GRB 051111. However, it is approximately three times as high as the value derived by Vreeswijk et al. (2004) for GRB 030323, and significantly lower than the value of SFR ≈ 11 measured for GRB 021004 (Fynbo et al., 2005). In fact, it is growing evidence that the majority of GRB host galaxies are Lyα emitters with star formation rates between 1 and 11 $M_{\odot}/year$. (Hammer & Flores, 2006; Fynbo et al., 2003; Jakobsson et al., 2005). In nearly every GRB host where Lyα emission can be detected, is has been detected (Jakobsson et al. 2005). Note that the lack of Lyα emission may still accommodate a star formation rate higher than the limit, since the Lyα photons are easily destroyed by scattering in the presence of dust (Berger et al., 2006b). Thus, even for a fairly low dust content, like GRB 060526 show indications of, it is possible that the star formation rate is in fact higher than the limit provided above. A more accurate value/limit of the star formation rate requires near-IR spectroscopy of the host galaxy for detection of Hα at 3.46μm and/or O II $\lambda 3727$ at 1.97μm (Berger et al., 2006b).

6.6 Ionization

As DLAs, GRBs are used to trace the evolution of elemental abundances, typically achieved by comparing the measured column density of a single ion of a given element, X^i, with that of neutral hydrogen, H I. The assumption is then made that the unobserved ionization stages make negligible contributions and $N(X^i)/N(\mathrm{H}^0) \approx N(\mathrm{X})/N(\mathrm{H})$ (Howk & Sembach, 1999). This is also an underlying assumption in the derived abundance ratios and calculations of this chapter. However, the validity of this approximation is questionable. Particularly when deriving conclusions on the nucleosynthetic processes, which require fine tuning of the relative abundances, it is important to account for both dust depletion and ionization effects. Unfortunately, the severity of ionization effects is still a debated issue; Lopez et al. (2002) claim that their ionization simulation demonstrates that their abundances are not affected by undetected ionized atoms. Howk & Sembach (1999) and Vladilo et al. (2001) argue for intermediate to small ionization corrections, typically in the order of 0.1 dex, while Izotov et al. (2001) predict large ionization corrections. This makes it difficult to account for ionization effects in a given set of abundances. In the following I will briefly introduce the issue of ionization corrections and use the H I column density and the ratio of N(Al II)/N(Al III) to discuss the ionization effects in the absorption system of GRB 060526.

From galactic interstellar studies it is known that the dominant ionization state in H I regions is the neutral one for elements with first ionization stage, IP > 13.6

eV (e.g. O I, N I) and the singly ionized one for elements with first IP < 13.6 eV and second IP > 13.6 eV (e.g. C II, Mg II, Al II, Si II, S II, Cr II, Mn II, Fe II, and Zn II). The reason for this is that most of the H I gas is self-shielded from $h\nu > 13.6$ eV, but transparent to $h\nu < 13.6$ eV photons. This is why it was expected that ionization did not play an important role for the low ions used in abundance determinations. This belief was supported by the first studies on ionization balance in DLAs (Viegas, 1995). However, the presence of Al III in DLAs has changed the picture and suggests that ionization corrections may be important after all (Vladilo et al., 2001). The aluminum ionization potentials of IP(Al I) $= 5.99$ eV and IP(Al II) $= 18.83$ eV, give reason to expect lack of Al III detection in H I regions. Observations from a large DLA sample show that this is not the case; Al II is present at the same radial velocity as low ions, but at a different radial velocity than high ions (Lu et al., 1995). Al III is therefore a tracer of moderately ionized gas, and the Al III/Al II ratio should give information on the effects of ionization on the derived abundances. Since no Al III is detected in the ISM of GRB 060526, an upper limit of 12.8 is obtained, see Section 5.5. The only line of Al II is saturated, but a lower limit of $\log N(\mathrm{Al\ II}) = 13.4$ is obtained. This gives a lower limit on the Al II/Al III ratio of

$$N(Al\ II)/N(Al\ III) > 10^{13.4}/10^{12.8} \approx 4\,.$$

Although this ratio is not very high, the column density of Al II is a strict lower limit. The COG analysis suggested a column density of $N(\mathrm{Al\ II}) = 15.1$. This would give a ratio of ≈ 200, which is a very high ratio indicating that very little aluminum in the doubly ionized state is present, and therefore that undetected ionization states are of little importance. In addition, the abundance obtained for Al III is an upper limit. However, if the ratio in fact is closer to 4 this would imply a significant degree of ionizaion.

Another general trend is that large column densities imply small ionization corrections. This is true in both of the two models treated by for instance Howk & Sembach (1999), Vladilo et al. (2001), and Lopez et al. (2002). In the first model, the Al III ordinates in the same H I region as the bulk of the low-ionization lines. In the second model, the Al III originates in a region distinct from, but physically connected to, the H I region where the bulk of singly ionized ions resides. In the first model, high neutral hydrogen column density leads to increased self shielding. In the second model, a larger amount of H I and singly ionized ions will dominate over the highly ionized ions. In addition to this, the absorbing systems are usually not made up of one single cloud, but rather several clouds, each then with a lower column density than the total (Lopez et al., 2002) - potentially increasing the importance of ionization further. As the column density of the GRB 060526 absorbing system is low compared to other DLAs and GRB-DLAs, this indicates that ionization may affect the derived abundances. However, Lopez et al. (2002) conclude that the mild influence of ionization abundance ratios of integrated column densities in DLAs (Vladilo et al., 2001; Howk & Sembach, 1999) can be extended to much lower column densities and thus suggesting self-shielding also in lower column density systems (the DLA treated by Lopez et al. (2002) has $\log N(\mathrm{HI}) = 20.7$). The situation then is that the low column density of the GRB 060526 absorption system indicate that ionization effects may be present, while it is difficult to draw conclusions from the limit on the ratio of N(Al II)/N(Al III). According to Vladilo et al. (2001) the N(H I) and N(Al II)/N(Al III) ratio should point in the same direction regarding ionization effects, as an anti-correlation between log N(H I) and the ratio N(Al III)/N(Al II) for DLAs is reported. As it is, no firm conclusion may be drawn about the ionization-assumption and whether it is a good approximation for the absoprtion system around GRB 060526 or not.

Chapter 7

Summary and outlook

We analyze low-resolution spectroscopic VLT data of the optical afterglow of GRB 060526. The wavelength of the Lyα line corresponds to a redshift of $z = 3.2216 \pm 0.0015$, and a range of metal absorption lines from Al II, C II, C IV, Si II, Si IV, S II, Fe II, Ni II, N I and, O I is found at approximately the same redshift. The absorption system at this redshift is interpreted as the host galaxy of the GRB. To obtain reliable column densities of as many of these elements as possible, we apply curve of growth analysis (COG) and fitting of absorption profiles using the program VPFIT. This results in reliable column densities of H I, Si IV and C IV; less accurate determinations for Fe II, S II and limits on Si II, C II (upper limits), Ni II, Al III, Co II, Zn II, Mg II, Si II* and Cr II (lower limits). A neutral hydrogen column density of $\log N(\mathrm{H~I}) = 20.01 \pm 0.15$ is found from fitting the broad wings of the Lyα absorption feature. As opposed to the majority of GRB absorption system, this is not a damped Lyα absorption system (DLA). The reason why such low N(H I) out-liers exist is not known and possible explanations, such as the so called 'high-ionization low N(H I)' scenario (Jakobsson et al., 2006), are discussed. However, GRB 060526 does not seem to fit with this scenario, but may rather be in agreement with GRBs being formed from massive runaway stars (Hammer & Flores, 2006) or a significant part of the star formation taking place in the outer edges of the molecular clouds (Jakobsson et al., 2006). Note also that recent results (Prochaska, 2006; Vreeswijk et al., 2006a; Watson et al., 2007) suggest that the absorption system is at $\sim$kpc distances from the progenitor. In this case the metallicity derived from the absorption system would not be directly representative for the progenitor metallicity. Possible ionization effects are discussed and a low column density of neutral hydrogen is often taken to imply less self shielding and a high ionization fraction. The obtained lower limit on the Al II/Al III ratio gives 4, but as the Al II column density is a very conservative lower limit, and the Al III is an upper limit, the true ratio is likly higher than this. However, the obtained ratio is not accurate enough to constrain the ionization-conditions any further.

The metallicity of the absorption system around GRB 060526 is approximately $0.35Z_\odot$ when attempting to account for dust depletion, or [S/H] $= -0.45 \pm 0.3$ or [Fe/H] $= -0.56 \pm 0.5$, i.e. respectively $0.35Z_\odot$ and $0.28Z_\odot$, when the abundances are not corrected for dust depletion. The difference between the dust-depletion corrected estimate and the uncorrected estimate indicates that the system is only mildly affected by dust –in the order of $0.3 - 0.5k_J$. The metallicity is amongst the higher values in the current GRB sample, especially if the relatively high redshift is taken into account. The metallicity lies at the limit of what is expected theoretically for Wolf-Rayet progenitor stars ($0.3Z_\odot$), while it is below the observational cut-off value at $0.5Z_\odot$ found by Wolf & Podsiadlowski (2007) . However, this picture could change drastically if the column density of iron is overestimated in VPFIT and the true column density lies closer to that obtained in the COG analysis. Although the abundance of sulphur is more certain, lowering the continuum could give a significantly smaller abundance also for this element. In this case the metallicity would be reduced and a more severe dust depletion would be likely, as iron would be under-abundant compared to sulphur.

The upper limit on the ratio of Si II* to Si II is calculated in an attempt to constrain the H I volume density and the mass and size of the absorbing region. This gives a low H I volume density, a low absorbing mass and small size of the cloud. As the column density obtained for Si II* is an upper limit and that of Si II is a lower limit, the ratio should be a relatively tight upper limit. This calculation is based on the assumption that collisions are responsible for the population of Si II* levels, which may well be incorrect. In the likely situation that UV pumping is in fact the responsible mechanism, no conclusion can be drawn on the H I volume density.

A limit on the SFR in the host galaxy of GRB 060526 is obtained from the lack of Lyα in emission. The limit obtained, SRF $< 2.8M_\odot\mathrm{yr}^{-1}$ is similar to that derived for GRB 050505 (Berger et al., 2006b) and GRB 051111 (Penprase et al., 2006). However, it is approximately three times as high as the value derived by Vreeswijk et al. (2004) for GRB 030323, and significantly lower than the value of SFR ≈ 11 measured for GRB 021004 (Fynbo et al., 2005).

To truly unveil the chemical composition of the interstellar medium (ISM) and the circumstellar medium (CMS) of the progenitor star of the GRB and draw conclusions about nucleosynthetic patterns, high resolution spectra are needed. While several abundance ratios, such as α/Fe-peak, N/α, C I/C II and Si IV/C IV are calculated, this merely shows that more accurate - and more numerous - column densities must be obtained to constrain nucleosynthetic patterns. Higher resolution data are also needed to resolve the detailed kinematic signatures and population ratios of excited ions. Such data do exist already, represented for example by data from the UV-Visual Echelle Spectrograph (UVES) at the VLT. The problem with such high resolution observations ($R \sim 30000$, equivalent to 10 km/s) is that they require relatively bright sources, typically in the order of 19 magnitudes or brighter. As the GRBs detected by Swift are to a large extent at high redshift, (and these are also the most interesting for cosmological purposes) they are also quite faint. Therefore only a few high resolution spectra of high redshift bursts have been obtained so far; GRB 060607 Ledoux et al. (2006), GRB 060418, Vreeswijk et al. (2006b), GRB 050730, D'Elia et al. (2006) and GRB 050922C D'Elia et al. (2007). A few more UVES spectra have been obtained for closer bursts. High resolution and thereby accurate knowledge about the metallicity in the CMS will also provide important clues on the nature of the progenitors of GRBs. This may provide a test of the metallicity-dependence of the progenitor models (Woosley, 2005).

Another problem is to detect the very faintest (i.e. possibly very high redshift) bursts. Even with low resolution data the bursts may be at so high redshift, or so heavily obscured, that no optical afterglow can be detected. To observe these bursts, exposures in the infrared are necessary. As of today the highest redshift detected for a GRB is $z = 6.29$ for GRB 050904 (Kawai et al., 2005), but Gamma-ray Bursts are expected to exist at higher redshifts than this. An upcoming instrument, which may contribute to detect these fainter afterglows, is the X-shooter at the VLT, which is scheduled to start operating in 2009. The resolution of $R = 4000 - 14000$, is slightly better than that provided by FORS1 ($R \lesssim 1500$), but most importantly, X-shooter will cover the spectral range from UV to the K' band, and therefore provide good cover in the infrared which is essential for high redshift bursts (as their Lyα absorptions features are substantially shifted). Detection of very high redshift burst would give opportunities to search for the Gunn-Peterson effect, which is of great importance for studies of the reionization epoch (Barkana R. & Loeb, 2001).

Another crucial condition for further progress is a more complete sample of GRBs. Although the SFR - or an upper limit on the SFR – in an individual GRB host galaxy may be inferred directly, the question is whether the host galaxies are representative for the star forming galaxies at their redshift. As of today the potential of GRBs to improve our knowledge about star formation is not fully exploited because possible biases, such as metallicity or dust, are not yet settled (Fynbo et al., 2007). The differing rates of star formation provide clues about the physical circumstances and the galaxies in which star birth takes place. The rate at which stars were made is intimately related to how the galaxies were formed. Therefore detailed knowledge about the early SFR may help to explain the evolution of the young universe.

Appendix A

Spectroscopic reductions in PyRAF

This is the ’recipe’ for spectroscopic reductions of FORS data using the `forslongslit` task made my Paul Vreeswijk. The recipe is originally written by Pall Jakobsson and then slightly modified by me.

1. In a unix-terminal, write:
   headinfo1 (for FORS1)
   headinfo2 (for FORS2)
   This creates a file head.info, which is a short log of the files. It contains information which we will later need to make a list of files with the right parameters. Specifically we use it in the next step when making a list of the frames which ’belong’ together, in this case by grism-selection. The keyword in head.info is chosen from the header, and is e.g. the size (naxis1, naxis2), grism (ins.optic5.name), filter (ins.optic7.name), readout mode (det.read.clock), exposuretime and image-type (det.type). The first part of the ’id’ refers to e.g. det -> detector and ins-> instrument. There might be slight variations from header to header (e.g. some grisms are named in ins.optic6.name instead of ins.optic5.name).

   ---

2. On a unix-terminal, execute `makelist.s` this is a script which makes different lists which are later used as input into other IRAF scripts. For every new grism to reduce, simply change the grism-name in ’| grep grismname’ and separate lists of bias-, GRB- and flats-frames for the grism will appear.

   ---

3. To clean cosmics from science (and standard) images, we have used a task called lacos-spec.cl. Simply type

   ```
   cl> lacos_spec input.fits output.fits mask.pl
   ```

   or

```
cl> epar lacos$_$spec
```

if you prefer to see all the parameters. we have used the prefix ccr (cleaning of cosmic rays) to signify that the pictures have been cleaned. This task task a bit of time but is really worth while! We have used four iterations, which usually leaves just a couple of cosmic rays in the forth iteration. When the task has finished, it is convenient to save input.fits as something else (e.g. original before the picture name), and copy outfit.fits to the initial name. This is because of the way the `forslongslit` script is written. You also need the gain and readout noise for the instrument which has taken your frames.

parameters	FORS1	FORS2
$xorder =$	9	9
$yorder =$	25	25
$niter =$	4	4
$gain =$	1.4	0.7
$readn =$	5.6	2.9

4. Bias-subtraction and flat-fielding of the images is done though the `forslongslit` task which utilize the standard IRAF task `ccdproc`. From `apextract` it takes for instance dispersion-line, which is a parameter that varies between FORS1 and FORS2. It is therefore important to first edit the parameters in apextract without executing. FORS1 uses dispersion-line (1), FORS2 uses dispersion-column (2), which is default.

```
cl> epar apextract

cl> epar forslongslit

(objectl=         grb.list) list object spectra
(standar=                 ) list standard spectra
(arclist=    wave.lss.list) list arc spectra
(flatlis=    flat.lss.list) list flat spectra



(biassub=         no) bias image already
                      subtracted?
(dobias =        yes) subtract overscan from
                      images?
(biassec=[280:1820,1030:1031])
                      overscan section?
(doflat =        yes) flat-field images?
(flatsec= [*,20:220]) flat response section
(extrdis=         no) extract and
                      dispersion-correct?
(optext =         no) optimally-extract spectra?
(trace  =         no) trace spectrum?
(line   =       1104) dispersion line
(fluxcal=         no) flux calibrate spectra?
```

The lists, 'grb.list', 'wave.lss.list' and 'flat.lss.list' are the lists made by the script `makelist.cl`, which is executed under step two. To make the optimal extraction work, the frames are trimmed in both x and y directions, to make sure there are no other objects on the slit and to cut away the overscan section. Note that the overscan is different for FORS1 and FORS2, in pixels it is, respectively $[2:15, 50:2000]$ and $[280:1820, 990:1020]$.

When running this script use order 10 or similar for overscan region, the lowest value which gives a reasonably good fit is fine. For the data analyzed in this thesis, order 5 was used. Use a high order for the flat response, typically ~ 100. Bias-subtraction appends 'b' to the output images, while flatfielding will append 'c'. This part of forslongslit mostly uses the 'inbuilt' IRAF task `ccdproc` to preprocess the images. `ccdproc` processes CCD images to correct and calibrate for detector defects, readout bias, zero level bias, dark counts, response, illumination, and fringing. It can also trim unwanted lines and columns and changes the pixel datatype. Of course, not all these steps are necessary for all data.

---

5. Do the same for standard star:

```
cl> forslongslit

(objectl=               ) list object spectra
(standar= std.most.list) list standard spectra
(arclist= wave.mos.list) list arc spectra
(flatlis= flat.mos.list) list lamp-flat spectra
```

Probably change "flatsec" and "biassec" (at least for FORS1). These are found by studying the images for instance with the program 'ds9'.

To extract the spectra of the images, the main task used by forslongslit is `apall`. This task provides functions for defining, modifying, tracing, and extracting apertures from two dimensional spectra. The functions desired are normally selected using switch parameters, in this case through `forslongslit`. This reduced the user's control of some of the parameters, but are easier to operate. You can however choose whether you want interactivity or not through `forslongslit`; when the task is run interactively, queries are made at each step allowing additional control of the operations performed on each input image. So, `apall` extracts the spectra, and the task `identify` (also through `forslongslit`) allows you to manually enter the known wavelengths of the lines in the arcspectrum (which is extracted with the science-frame aperture as reference) and play with these until you get a good fit. Typically that means, with a Legendre function of order six, an $RMSof \sim 0.15$ or lower. For the next step, the wavelength solution, IRAF has to know which wavelength solution to use. For this purpose the task `hedit` is run for the object spectrum with the arc spectrum as a reference. This is done automatically with `forslongslit`. Then finally, `dispcor` makes the actual dispersion corrections and out comes a (hopefully) beautiful, wavelength calibrated object spectrum.

6. Time to extract:

```
cl> forslongslit

(objectl=      grb.list) list object spectra
(standar=              ) list standard spectra
(arclist= wave.lss.list) list arc spectra
(flatlis=              ) list lamp-flat spectra
(doflat =            no) flat-field images?
(extrdis=           yes) extract and
                         dispersion-correct?
(optext =           yes) optimally-extract
                         spectra?
(trace  =           yes) trace spectrum?
(line   =          1104) dispersion line
(backsam= -25:-12,12:25) background sample region
(linelis=   mylines.dat) file with lamp lines
```

When running this script:

- Type ’d’ to delete an aperture and ’m’ to mark another one.
- Type ’b’ to look at background. To change sampling: e.g. ": $sample - 20 : -10, 10 : 20$". Or type ’t’ and ’s’ to select sample.
- When tracing: change order to ":order 2". Instead of deleting points, one can define a sample with ’s’ (twice).
- Type ’f’ to redo fit.
- Lamp spectrum: download FORS manual, page 63, to ID lines.

Usually, 20-30 lines and order $= 6$ gives an root mean square $RMSof \sim 0.15$. Wavelength solution, Å/pixel, is added to header. The spectra are converted to e- (from ADU). This is because it can happen that the standard star is obtained with a different gain –> messes up the flux calibration using ADUs. This will append "dispcor" to the files.

————————-

7. Extract the standard star:

```
cl> forslongslit

(objectl=              ) list with object spectra
(standar=  std.mos.list) list with standard spectra
(arclist= wave.mos.list) list with arc spectra
```

When running this script:

- Change the aperture size, something like 15 pixels on either side.
- Change background.

---

8. Flux calibrate:

```
cl> forslongslit

(objectl=     grb.list) list with object spectra
(standar= std.mos.list) list with standard spectra
(extrdis=           no) extract and dispersion-correct?
(fluxcal=          yes) flux calibrate spectra?
(calibdi=           ./) directory with standards
```

Get the standard star files at http://www.eso.org/observing/standards/spectra/ or other similar pages. Flux-calibration is done when switching on the 'fluxcal' option in `forslonglist`. When running this part:

- A bit tricky, possibly delete points at the starting wavelength, but also delete obvious atmospheric sky lines (e.g. 6850 AA, 7600 AA).
- High polynomial fit, e.g. ":order 13".

This will append "fluxcal" to the files.

---

9. Combine the 1D spectra: A separate task, `comb1Dspec` is used for this purpose. Create a list of the spectra that is to be combined by typing

```
ls fluxcalcFORS2_LSS* > fluxcal.list$

cl> comb1Dspec

(inputli=  fluxcal.list) list with multispec spectra
(outspec=   fluxcal.ave) output average spectrum
(outerro=   fluxcal.err) output error spectrum
(outs2n =   fluxcal.s2n) output S/N spectrum
```

From this task, three spectra are obtained; the total flux calibrated spectrum, the total error spectrum and the total signal-to-noise spectrum.

Appendix B

The script written for the COG analysis

I wrote this script to perform the curve of growth analysis on the unblended absorption lines found in the spectroscopic data of GRB 060526.

```
pro cog4

c = 3E5 ; [km/s]
Nfl = dblarr(1,100)
itau = dblarr(1,100)
W_lambda = dblarr(1,100)
Nfl = 10.^(findgen(100)/15+14.4)

;------------------ b = 'infinity' -----------------------------------
```

$b = \infty$ creates a straight line through the plot, which is nice to have as comparison for the curved line corresponding to a finite b-parameter. $b = 100000$ as is used here is a good enough approximation to infinity, while it is still easy to handle for the integral.

```
b=100000

itau = 1.496E-15*Nfl/b
Fout = cFtau(itau)
i = 0

while Fout(i) eq 0 do begin
i = i+1
endwhile

if Fout(i) ne 0 then begin
W_lambda = 2*b*Fout/c
i = i+1
endif

;tar vare paa variablene i andre navn
Nfl_b2 = Nfl
W_lambda_b2 = W_lambda

plot, alog10(Nfl_b2*1E-8), alog10(W_lambda_b2),
```

```
yrange = [-5.5,-2.6], xrange = [5.8,13], $
xtitle = 'log (Nf!7k!3)[cm!E-1!N]', $
ytitle = 'log (W!Ir!N/!7k!3)', $
title  = 'Curve of growth',/xstyle,/ystyle,charsize=1.5

; ----------------------------------------------------------------------
```

Fout calls the function cFtau which handles the integration. The integral itself is given in the function Ftau.

```
function cFtau, itau
common FF, tau
Fout=itau
for i=0,n_elements(itau)-1 do begin
   tau=itau[i]
   Fout[i]=QROMO('Ftau',0.0,/midexp)
endfor
return,Fout
end

function Ftau, X
common FF
return, 1-exp(-tau*exp(-X^2))
end
```

For each element, information about the number of lines, equivalent widths, wavelengths, oscillator strengths and errors are given. Here I only display the code for Al II, it is similar for other ions. The column density is set at an initial guessed value. Each element is also plotted on to the COG plot in this step.

```
;------------------- FOR AlII -------------------------------------

j=1
f_ion = fltarr(1,j)
eqw_ion = fltarr(1,j)
logNflambda_ion = fltarr(1,j)
wlambda_ion = fltarr(1,j)
yerr1_ion = fltarr(1,j)
yerr2_ion = fltarr(1,j)


logN_ion = 15.1
N_ion = 10.^logN_ion
lambda_ion = [1670.79]
f_ion = [1.88]
eqw_ion = [1.0422]
error_ion = [0.0435]
i = 0

while i lt j do begin
    if error_ion(i) gt eqw_ion(i) then error_ion(i) = eqw_ion(i) - 0.001
    logNflambda_ion(i) = logN_ion + alog10(lambda_ion(i)*10.^(-8)*f_ion(i))
    wlambda_ion(i) = eqw_ion(i)/lambda_ion(i)
    yerr1_ion(i) = alog10((eqw_ion(i) - error_ion(i))/lambda_ion(i))
    - alog10(eqw_ion(i)/lambda_ion(i))
    yerr2_ion(i) = alog10((eqw_ion(i) + error_ion(i))/lambda_ion(i))
    - alog10(eqw_ion(i)/lambda_ion(i))
    i=i+1
endwhile
```

```
plotsym, 0,1.5, /fill, color=225
oploterror, logNflambda_ion, alog10(wlambda_ion), yerr1_ion, Psym= 8, /lobar
oploterror, logNflambda_ion, alog10(wlambda_ion), yerr2_ion, Psym= 8, /hibar


;lagrer verdiene i egne variabler
logN_AlII = logN_ion
lambda_AlII = lambda_ion
f_AlII = f_ion
eqw_AlII = eqw_ion
logNflambda_AlII = logNflambda_ion
wlambda_AlII = wlambda_ion
yerr1_AlII = yerr1_ion
yerr2_AlII = yerr2_ion
error_AlII = error_ion


;------------------- Fitting ---------------------------------------
```

Information about all other ions are treated similarly to Al II. Below two vectors containing the $\log Nf\lambda$ and EW/λ values of all lines are defined and a curve is fit to these data-points.

```
X = [logNflambda_FeII(0),logNflambda_NiII(2), $
     logNflambda_SII(1), logNflambda_NiII(0), $
     logNflambda_NiII(1),logNflambda_SiIIf(0),$
     logNflambda_SII(0), logNflambda_OI(0),   $
     logNflambda_PII(0), logNflambda_SiIV(0), $
     logNflambda_FeII(1),logNflambda_SiIV(1), $
     logNflambda_NI(0),  logNflambda_CIV(0),  $
     logNflambda_CIV(1), logNflambda_ClII(0), $
     logNflambda_AlII(0),logNflambda_SiII(1), $
     logNflambda_SiII(2),logNflambda_SiII(0), $
     logNflambda_OI(1),  logNflambda_CII(0),  $
     logNflambda_CII(1)]+8)

Y = [wlambda_FeII(0),wlambda_NiII(2), $
     wlambda_SII(1), wlambda_NiII(0), $
     wlambda_NiII(1),wlambda_SiIIf(0),$
     wlambda_SII(0), wlambda_PII(0),  $
     wlambda_SiIV(0),wlambda_FeII(1), $
     wlambda_SiIV(1),wlambda_NI(0),   $
     wlambda_CIV(0), wlambda_CIV(1),  $
     wlambda_ClII(0),wlambda_AlII(0), $
     wlambda_OI(1),  wlambda_SiII(1), $
     wlambda_SiII(2),wlambda_SiII(0), $
     wlambda_OI(0),  wlambda_CII(0),  $
     wlambda_CII(1)]

if n_elements(Y) ne n_elements(X) then begin
    print, 'ikke like mange elementer i X og Y'
    print, 'antall elementer i X:'
    print, n_elements(X)
    print, 'antall elementer i Y:'
    print, n_elements(Y)
endif

A = double(50)
w = Y/Y
yfit = curvefit(X,Y,w,A,sigma,function_name='cogf',/noder, iter=niter,itmax=100,
       chi2=chi2,chisq=chisq,status=status)
xyouts,10,-2.8,'best fit Doppler, b='+string(A),charsize=1.5,/data
```

Curvefit calls the function ’cogf’ which is displayed below. ’cogf’ calls the ’cFtau’ function displayed above. The best fit Doppler parameter, A, is the outcome.

```
pro cogf, X, A, F

itau = 1.496E-15*X/A
Fout = cFtau(itau)

F = 2/(3E5)*Fout*A

END


;------------ plotting the new cog, now with the best fit Doppler parameter ---------
```

The resulting best fit is then plotted

```
itau = 1.496E-15*Nfl/A(0)
Fout = cFtau(itau)

i = 0
while Fout(i) eq 0 do begin
i = i+1
endwhile

if Fout(i) ne 0 then begin
W_lambda = 2*A(0)*Fout/c
i = i+1
endif

W_lambda_A = W_lambda

oplot, alog10(Nfl*1E-8), alog10(W_lambda)


;-------------------- finding chi squared --------------------------------
```

The value for χ^2 is found by adding up the standard deviation between each line and the best fit COG. Only Al II is shown here too reduce the length of this appendix. The code is the same for all ions. The 3 χ limits on A are found by testing. For each A the functions above, cFtau and Ftau are evaluated with respect to this specific A value.

```
chi_sq = 0

;---- AlII ----------------------------------------------------------
x = 10.^([logNflambda_AlII(0)]+8)
itau = 1.496E-15*x/A
Fout = cFtau(itau)
W_lambda = 2*Fout/c*A
i = 0
while i lt 1 do begin
    chi_sq = chi_sq + ((wlambda_AlII(i) - W_lambda(i))*lambda_AlII(i))^2 $
      /error_AlII(i)^2
    i = i+1
endwhile
```

```
;------------------ plotting 3 chi limits on b ------------------------
       A = 46

       itau = 1.496E-15*Nfl/A(0)
       Fout = cFtau(itau)

       i = 0
       while Fout(i) eq 0 do begin
       i = i+1
       endwhile

       if Fout(i) ne 0 then begin
       W_lambda = 2*A(0)*Fout/c
       i = i+1
       endif

       W_lambda_Ahigh = W_lambda

       oplot, alog10(Nfl*1E-8), alog10(W_lambda_Ahigh),linestyle=2

      ;------------------------------
       A = 34
       itau = 1.496E-15*Nfl/A(0)
       Fout = cFtau(itau)

       i = 0
       while Fout(i) eq 0 do begin
       i = i+1
       endwhile

       if Fout(i) ne 0 then begin
       W_lambda = 2*A(0)*Fout/c
       i = i+1
       endif

       W_lambda_Alow = W_lambda

       oplot, alog10(Nfl*1E-8), alog10(W_lambda_Alow), linestyle=2


;---------------- plotting legends and comments --------------------

xyouts,7.7,-2.8,'Linear part, b=inf',charsize=1.5,/data
;xyouts,10,-2.8,'best fit Doppler, b=42',charsize=1.5,/data

xyouts,6.1,-2.83,'AlII',charsize=1.5,/data
plotsym,0,1.5,/fill,color=225
oplot, [6.0],[-2.8],psym=8
```

... and so forth for the rest of the ions.

Appendix C

The script written for the dust-depletion correction

I wrote this script to achieve an improved estimate of the metallicity and dust-to-gas ratio of the GRB in Section 6.3. Three points are given by the observed abundances in GRB 060526, the metallicities derived from each of these elements are given in the a-vector, their corresponding errors in the error-vector. The four depletion patterns are then applied to see which fit the data best. A range of different dust-to-gas ratios, k, are fitted, and for each k, a range of metallicities, Z, values are fitted. The combination giving the lowest χ^2 for each depletion pattern is saved and plotted.

```
pro dust

x = [0,1,5]
a = [-0.45, -0.52, -0.56]

error = fltarr(3)
error = [0.3, 0.5, 0.5]

!p.multi = [0,2,2]


;------------------ Halo -----------------------------------
```

’kappa’ is the dust-to-gas ratio of GRB to the clouds, the appendix (halo, dh, wd or cd) giving the specific cloud type. ’Z’ is the ratio of GRB metallicity to sun metallicity, again, the appendix revealing which is the assumed depletion pattern.

```
Z_halo= fltarr(300)
Z_halo = findgen(300)*0.003+0.01

dep_halo = [-0.04,-0.28,-0.42,-0.60,-0.51,-0.64,-0.84]
el_halo=['S','Si','Mg','Mn','Cr','Fe','Ni']
xpunkt = findgen(7)
plotverdi_halo = fltarr(7)
bestplotverdi_halo = fltarr(7)

kappa_halo = findgen(300)*0.003+0.01
plotverdi_halochi = fltarr(4)
chi_halo = fltarr(300)
```

```
chi_halominst = 1000

l=0
while l lt 300 do begin
    k = 0
    while k lt 300 do begin
        i = 0
        while i lt 7 do begin
            plotverdi_halo(i) = alog10(1+kappa_halo(k))*(10.^dep_halo(i) -1)
            i = i+1
        endwhile

        plotverdi_halochi(0) = plotverdi_halo(0)
        plotverdi_halochi(1) = plotverdi_halo(1)
        plotverdi_halochi(2) = plotverdi_halo(5)
        ;plotverdi_halochi(3) = plotverdi_halo(6)

        j = 0
        chi_haloj=0
        while j lt 3 do begin
            chi_haloj = chi_haloj + (((a(j)-alog10(Z_halo(l)))
                        - plotverdi_halochi(j))/error(j))^2
            j = j+1
        endwhile


        chi_halo(k) = chi_haloj

        if chi_halo(k) lt chi_halominst then begin
            chi_halominst = chi_halo(k)
            kappa_halominst = kappa_halo(k)
            Z_halominst = Z_halo(l)
            y_halo = a-alog10(Z_halo(l))
            bestplotverdi_halo=plotverdi_halo
        endif

        k = k+1
    endwhile

    l = l+1
endwhile


;------------------- Disk+Halo ------------------------------------
Z_dh = fltarr(300)
Z_dh = findgen(300)*0.003+0.01

dep_dh = [0.03,-0.26,-0.61,-0.66,-0.80,-0.92,-1.15]
el_dh=['S','Si','Mg','Mn','Cr','Fe','Ni']
xpunkt = findgen(7)
plotverdi_dh = fltarr(7)
bestplotverdi_dh = fltarr(7)

kappa_dh = findgen(300)*0.003+0.01
plotverdi_dhchi = fltarr(4)
chi_dh = fltarr(300)
chi_dhminst = 1000

l=0
while l lt 300 do begin
    k = 0
```

```
    while k lt 300 do begin
        i = 0
        while i lt 7 do begin
            plotverdi_dh(i) = alog10(1+kappa_dh(k))*(10.^dep_dh(i) -1)
            i = i+1
        endwhile

        plotverdi_dhchi(0) = plotverdi_dh(0)
        plotverdi_dhchi(1) = plotverdi_dh(1)
        plotverdi_dhchi(2) = plotverdi_dh(5)
        ;plotverdi_dhchi(3) = plotverdi_dh(6)

        chi_dhj = 0
        j = 0
        while j lt 3 do begin
            chi_dhj = chi_dhj + (((a(j)-alog10(Z_dh(l)))
                      - plotverdi_dhchi(j))/error(j))^2
            j = j+1
        endwhile

        chi_dh(k) = chi_dhj

        if chi_dh(k) lt chi_dhminst then begin
            chi_dhminst = chi_dh(k)
            kappa_dhminst = kappa_dh(k)
            Z_dhminst = Z_dh(l)
            y_dh = a-alog10(Z_dh(l))
            bestplotverdi_dh=plotverdi_dh
        endif

        k = k+1
    endwhile

    l = l+1
endwhile

;------------------ Warm disk ---------------------------------------
Z_wd = fltarr(300)
Z_wd = findgen(300)*0.01+0.01

dep_wd = [0.06,-0.43,-0.81,-0.92,-1.10,-1.22,-1.46]
el_wd=['S','Si','Mg','Mn','Cr','Fe','Ni']

xpunkt = findgen(7)
plotverdi_wd = fltarr(7)
bestplotverdi_wd = fltarr(7)

kappa_wd = findgen(300)*0.01+0.01
plotverdi_wdchi = fltarr(4)
chi_wd = fltarr(300)
chi_wdminst = 1000

l=0
while l lt 300 do begin
    k = 0
    while k lt 300 do begin
        i = 0
        while i lt 7 do begin
            plotverdi_wd(i) = alog10(1+kappa_wd(k))*(10.^dep_wd(i) -1)
            i = i+1
        endwhile
```

```
        plotverdi_wdchi(0) = plotverdi_wd(0)
        plotverdi_wdchi(1) = plotverdi_wd(1)
        plotverdi_wdchi(2) = plotverdi_wd(5)
        ;plotverdi_wdchi(3) = plotverdi_wd(6)

        chi_wdj = 0
        j = 0
        while j lt 3 do begin
            chi_wdj = chi_wdj + (((a(j)-alog10(Z_wd(l)))
                    - plotverdi_wdchi(j))/error(j))^2
            j = j+1
        endwhile

        chi_wd(k) = chi_wdj

        if chi_wd(k) lt chi_wdminst then begin
            chi_wdminst = chi_wd(k)
            kappa_wdminst = kappa_wd(k)
            Z_wdminst = Z_wd(l)
            y_wd = a-alog10(Z_wd(l))
            bestplotverdi_wd=plotverdi_wd
        endif

        k = k+1
    endwhile

    l = l+1
endwhile

;-------------------- Cool disk ----------------------------------------

Z_cd = fltarr(300)
Z_cd = findgen(300)*0.01+0.01

dep_cd = [0.0,-1.31,-1.40,-1.39,-2.18,-2.18,-2.6]
el_cd =['S','Si','Mg','Mn','Cr','Fe','Ni']


xpunkt = findgen(7)
plotverdi_cd = fltarr(7)
bestplotverdi_cd = fltarr(7)

kappa_cd = findgen(300)*0.01+0.01
plotverdi_cdchi = fltarr(4)
chi_cd = fltarr(300)
chi_cdminst = 1000

l=0
while l lt 300 do begin
    k = 0
    while k lt 300 do begin
        i = 0
        while i lt 7 do begin
            plotverdi_cd(i) = alog10(1+kappa_cd(k))*(10.^dep_cd(i) -1)
            i = i+1
        endwhile

        plotverdi_cdchi(0) = plotverdi_cd(0)
        plotverdi_cdchi(1) = plotverdi_cd(1)
        plotverdi_cdchi(2) = plotverdi_cd(5)
        ;plotverdi_cdchi(3) = plotverdi_cd(6)
```

```
        chi_cdj = 0
        j = 0
        while j lt 3 do begin
            chi_cdj = chi_cdj + (((a(j)-alog10(Z_cd(l)))
                      -plotverdi_cdchi(j))/error(j))^2
            j = j+1
        endwhile

        chi_cd(k) = chi_cdj

        if chi_cd(k) lt chi_cdminst then begin
            chi_cdminst = chi_cd(k)
            kappa_cdminst = kappa_cd(k)
            Z_cdminst = Z_cd(l)
            y_cd = a-alog10(Z_cd(l))
            bestplotverdi_cd=plotverdi_cd
        endif

        k = k+1
    endwhile

    l = l+1
endwhile

;--------------------- plotting --------------------------------------------

plot, xpunkt, bestplotverdi_dh, xticks = 6, yrange=[-0.3,0.1],$
xtickname = el_dh, xtickv = xpunkt, xrange = [-0.5, 6.5],ytitle= '[X/H]'
xyouts, 2,0.06,'Warm disk and halo clouds'
xyouts, 0,-0.16, 'Z/Z!Isun!N = 0.35'
xyouts, 0,-0.20, 'k/k!Isun!N = 0.31'
xyouts, 0,-0.24, '!7v!3!E2!N = 0.0003'
oplot, x,y_dh, psym=4
```

.... and similar for all four depletion patterns.

Bibliography

Asplund, M., Grevesse, N., and Sauval, A. J. (2005). The Solar Chemical Composition. In Barnes, III, T. G. and Bash, F. N., editors, *ASP Conf. Ser. 336: Cosmic Abundances as Records of Stellar Evolution and Nucleosynthesis*, pages 25–+.

Barkana R. & Loeb (2001). In the beginning: the first sources of light and the reionization of the universe. *physrep*, 349:125–238.

Berger, E., Fox, D. B., Kulkarni, S. R., Frail, D. A., and Djorgovski, S. G. (2006a). The ERO Host Galaxy of GRB 020127: Implications for the Metallicity of GRB Progenitors. *ArXiv Astrophysics e-prints*.

Berger, E., Penprase, B. E., Cenko, S. B., Kulkarni, S. R., Fox, D. B., Steidel, C. C., and Reddy, N. A. (2006b). Spectroscopy of GRB 050505 at z = 4.275: A logN(H I) = 22.1 DLA Host Galaxy and the Nature of the Progenitor. *The Astrophysical Journal*, 642:979–988.

Bradley & Dale (1996). *An introduction to modern astrophysics*. Addison-Wesley Publixhing Company, Inc ISBN 0-321-21030-1.

Campana, S., Barthelmy, S. D., Boyd, P. T., Brown, P. J., Burrows, D. N., Cummings, J. R., Guidorzi, C. G., Holland, S. T., Kennea, J. A., Markwardt, C. B., Marshall, F. E., Moretti, A., Page, K. L., Stamatikos, M., Tagliaferri, G., and vanden Berk, D. E. (2006a). GRB 060526: Swift detection of a burst with X-ray and optical afterglow. *GRB Coordinates Network*, 5162:1–+.

Campana, S., Mangano, V., Blustin, A. J., and Brown, P. (2006b). The association of GRB 060218 with a supernova and the evolution of the shock wave. *Nature*, 442:1008–1010.

Castro-Tirado, A. J., Gorosabel, J., Guziy, S., Reverte, D., and Castro Cerón, J. M. (2003). GRB 030227: The first multiwavelength afterglow of an INTEGRAL GRB. *Astronomy and Astrophysics*, 411:L315–L319.

Chen, H.-W., Prochaska, J. X., Bloom, J. S., and Thompson, I. B. (2005). Echelle Spectroscopy of a Gamma-Ray Burst Afterglow at z = 3.969: A New Probe of the Interstellar and Intergalactic Media in the Young Universe. *The Astrophysical Journal, Letters*, 634:L25–L28.

Chen, H.-W., Prochaska, J. X., Ramirez-Ruiz, E., Bloom, J. S., Dessauges-Zavadsky, M., and Foley, R. J. (2006). On the absence of Wind Signatures in GRB Afterglow Spectra: Constraints on the Wolf-Rayet Winds of GRB Progenitors. *ArXiv Astrophysics e-prints*.

Conselice, C., Vreeswijk, P., Fruchter, A., and Levan, A. (2005). Grb-selected high z galaxies. *The Astrophysical Journal*, 633:29:40.

Cusumano, G., Mangano, V., Chincarini, G., and Panaitescu, A. (2006). Gamma-ray bursts: Huge explosion in the early Universe. *Nature*, 440:164–+.

Dai, Z. G., Zhang, B., and Liang, E. W. (2006). GRB 060218/SN 2006aj: Prompt Emission from Inverse-Compton Scattering of Shock Breakout Thermal Photons. *ArXiv Astrophysics e-prints*.

D'Elia, V., Fiore, F., Meurs, E., Chincarini, G., Melandri, A., and Norci, L. (2006). UVES/VLT high resolution spectroscopy of GRB 050730 afterglow: probing the features of the GRB environment. *ArXiv Astrophysics e-prints*.

D'Elia, V., Piranomonte, S., Ward, P., Fiore, F., Meurs, E. J. A., Norci, L., and Vergani, S. D. (2007). UVES - VLT High Resolution Spectroscopy of GRB Afterglows. *ArXiv Astrophysics e-prints*.

Emerson, D. (1996). *Interpreting Astronomical Spectra*. Interpreting Astronomical Spectra, by D. Emerson, pp. 472. ISBN 0-471-94176-X. Wiley-VCH , June 1996.

Freedman, W. L., Madore, B. F., Gibson, B. K., Ferrarese, L., Kelson, D. D., Sakai, S., Mould, J. R., Kennicutt, Jr., R. C., Ford, H. C., Graham, J. A., Huchra, J. P., Hughes, S. M. G., Illingworth, G. D., Macri, L. M., and Stetson, P. B. (2001). Final Results from the Hubble Space Telescope Key Project to Measure the Hubble Constant. *The Astrophysical Journal*, 553:47–72.

Fruchter, A. S., Levan, A. J., Strolger, L., Vreeswijk, P. M., Thorsett, S. E., Bersier, D., Burud, I., Castro Cerón, J. M., Castro-Tirado, A. J., Conselice, C., Dahlen, T., Ferguson, H. C., Fynbo, J. P. U., Garnavich, P. M., Gibbons, R. A., Gorosabel, J., Gull, T. R., Hjorth, J., Holland, S. T., Kouveliotou, C., Levay, Z., Livio, M., Metzger, M. R., Nugent, P. E., Petro, L., Pian, E., Rhoads, J. E., Riess, A. G., Sahu, K. C., Smette, A., Tanvir, N. R., Wijers, R. A. M. J., and

Woosley, S. E. (2006). Long γ-ray bursts and core-collapse supernovae have different environments. *Nature*, 441:463–468.

Fruchter, A. S., Thorsett, S. E., Metzger, M. R., Sahu, K. C., and Petro, L. (1999). Hubble Space Telescope and Palomar Imaging of GRB 990123: Implications for the Nature of Gamma-Ray Bursts and Their Hosts. *The Astrophysical Journal, Letters*, 519:L13–L16.

Fryer, C. L., Mazzali, P. A., Prochaska, J., Cappellaro, E., Panaitescu, A., Berger, E., van Putten, M., van den Heuvel, E. P. J., Young, P., Hungerford, A., Rockefeller, G., Yoon, S. ., Podsiadlowski, P., Nomoto, K., Chevalier, R., Schmidt, B., and Kulkarni, S. (2007). Constraints on Type Ib/c and GRB Progenitors. *ArXiv Astrophysics e-prints*.

Fynbo, J. P. U., Gorosabel, J., Smette, A., Fruchter, A., Hjorth, J., Pedersen, K., Levan, A., Burud, I., Sahu, K., Vreeswijk, P. M., Bergeron, E., Kouveliotou, C., Tanvir, N., Thorsett, S. E., Wijers, R. A. M. J., Castro Cerón, J. M., Castro-Tirado, A., Garnavich, P., Holland, S. T., Jakobsson, P., Møller, P., Nugent, P., Pian, E., Rhoads, J., Thomsen, B., Watson, D., and Woosley, S. (2005). On the Afterglow and Host Galaxy of GRB 021004: A Comprehensive Study with the Hubble Space Telescope. *The Astrophysical Journal*, 633:317–327.

Fynbo, J. P. U., Hjorth, J., Malesani, D., Sollerman, J., Watson, D., Jakobsson, P., Gorosabel, J., and Jaunsen, A. O. (2007). Gamma-ray burst host galaxies and the link to star-formation. *ArXiv Astrophysics e-prints*.

Fynbo, J. P. U., Jakobsson, P., Möller, P., and Hjorth, J. (2003). On the Lyalpha emission from gamma-ray burst host galaxies: Evidence for low metallicities. *Astronomy and Astrophysics*, 406:L63–L66.

Fynbo, J. P. U., Starling, R. L. C., Ledoux, C., Wiersema, K., Thöne, C. C., Sollerman, J., Jakobsson, P., Hjorth, J., Watson, D., and Vreeswijk, P. M. (2006a). Probing cosmic chemical evolution with gamma-ray bursts: GRB 060206 at z = 4.048. *Astronomy and Astrophysics*, 451:L47–L50.

Fynbo, J. P. U., Watson, D., and Thöne, C. C. (2006b). No supernovae associated with two long-duration γ-ray bursts. *Nature*, 444:1047–1049.

Fynbo, J. U., Gorosabel, J., Dall, T. H., Hjorth, J., Pedersen, H., Andersen, M. I., Møller, P., Holland, S., Smail, I., Kobayashi, N., Rol, E., Vreeswijk, P., Burud, I., Jensen, B. L., Thomsen, B., Henden, A., Vrba, F., Canzian, B., Castro Cerón, J. M., Castro-Tirado, A. J., Cline, T., Goto, M., Greiner, J., Hanski, M. T., Hurley, K., Lund, N., Pursimo, T., Østensen, R., Solheim, J., Tanvir, N., and

Terada, H. (2001). The optical afterglow and host galaxy of GRB 000926. *Astronomy and Astrophysics*, 373:796–804.

Gehrels, N., Norris, J. P., and Barthelmy, S. D. (2006). A new γ-ray burst classification scheme from GRB060614. *Nature*, 444:1044–1046.

Ghirlanda, G., Ghisellini, G., and Lazzati, D. (2004). The Collimation-corrected Gamma-Ray Burst Energies Correlate with the Peak Energy of Their νF_ν Spectrum. *The Astrophysical Journal*, 616:331–338.

Hammer & Flores (2006). Detection of wolf-rayet star in host galaxies of grbs: are grbs produced by runaway massive stars ejected from high stellar density regions? *Astronnomy and Astrophysics*, April:11.

Harrison, F. A., Yost, S. A., Sari, R., and Berger, E. (2001). Broadband Observations of the Afterglow of GRB 000926: Observing the Effect of Inverse Compton Scattering. *The Astrophysical Journal*, 559:123–130.

Hirschi, R., Meynet, G., and Maeder, A. (2005). Stellar evolution with rotation. XIII. Predicted GRB rates at various Z. *Astronomy and Astrophysics*, 443:581–591.

Hjorth, J., Sollerman, J., Møller, P., Fynbo, J. P. U., Woosley, S. E., Kouveliotou, C., Tanvir, N. R., Greiner, J., Andersen, M. I., Castro-Tirado, A. J., Castro Cerón, J. M., Fruchter, A. S., Gorosabel, J., Jakobsson, P., Kaper, L., Klose, S., Masetti, N., Pedersen, H., Pedersen, K., Pian, E., Palazzi, E., Rhoads, J. E., Rol, E., van den Heuvel, E. P. J., Vreeswijk, P. M., Watson, D., and Wijers, R. A. M. J. (2003). A very energetic supernova associated with the γ-ray burst of 29 March 2003. *Nature*, 423:847–850.

Hjorth, J., Watson, D., Fynbo, J. P. U., Price, P. A., Jensen, B. L., Jørgensen, U. G., Kubas, D., Gorosabel, J., Jakobsson, P., Sollerman, J., Pedersen, K., and Kouveliotou, C. (2005). The optical afterglow of the short γ-ray burst GRB 050709. *Nature*, 437:859–861.

Hoffman, R. D., Woosley, S. E., Fuller, G. M., and Meyer, B. S. (1996). Production of the Light p-Process Nuclei in Neutrino-driven Winds. *The Astrophysical Journal*, 460:478–+.

Howk & Sembach (1999). Ionized Gas in Damped Lyman-alpha Systems and Its Effects on Elemental Abundance Studies. In *Bulletin of the American Astronomical Society*, pages 1452–+.

Izotov, Y., Schaerer, D., and Charbonnel, C. (2001). On ionization effects and abundance ratios in damped ly$alpha$ systems. *The Astrophysical Journal*.

Jakobsson, P., Björnsson, G., Fynbo, J. P. U., Jóhannesson, G., Hjorth, J., Thomsen, B., Møller, P., Watson, D., Jensen, B. L., Östlin, G., Gorosabel, J., and Gudmundsson, E. H. (2005). Ly-α and ultraviolet emission from high-redshift gamma-ray burst hosts: to what extent do gamma-ray bursts trace star formation? *Memoirs of the RAS*, 362:245–251.

Jakobsson, P., Fynbo, J. P. U., Ledoux, C., and Vreeswijk, P. (2006). H I column densities of z $>$ 2 Swift gamma-ray bursts. *Astronomy and Astrophysics*, 460:L13–L17.

Jakobsson, P., Hjorth, J., Fynbo, J. P. U., Watson, D., Pedersen, K., Björnsson, G., and Gorosabel, J. (2004). Swift Identification of Dark Gamma-Ray Bursts. *The Astrophysical Journal, Letters*, 617:L21–L24.

Kawai, N., Kosugi, G., Aoki, K., Yamada, T., Totani, T., Ohta, K., Iye, M., Hattori, T., Aoki, W., Furusawa, H., Hurley, K., Kawabata, K., Kobayashi, N., Komiyama, Y., Mizumoto, Y., Nomoto, K., Noumaru, J., Ogasawara, R., Sato, R., Sekiguchi, K., Shirasaki, Y., Suzuki, M., Takata, T., Tamagawa, T., Terada, H., Watanabe, J., Yatsu, Y., and Yoshida, A. (2005). Afterglow spectrum of a gamma-ray burst with the highest known redshift z=6.295. *ArXiv Astrophysics e-prints*.

Kennicutt, Jr., R. C. (1998). Star Formation in Galaxies Along the Hubble Sequence. *ARAA*, 36:189–232.

Kobulnicky & Kewley (2004). Metallicities of 0.3 < z < 1.0 galaxies in the goods-north field. *The Astrophysical Journal*, 617:240–261.

Kouveliotou, C., Meegan, C. A., Fishman, G. J., Bhat, N. P., Briggs, M. S., Koshut, T. M., Paciesas, W. S., and Pendleton, G. N. (1993). Identification of two classes of gamma-ray bursts. *The Astrophysical Journal Letters*, 413:L101–L104.

Lamb & Reichart (2000). Gamma-Ray Bursts as a Probe of the Very High Redshift Universe. *The Astrophysical Journal*, 536:1–18.

Ledoux, C., Vreeswijk, P., Ellison, S., Jaunsen, A., Smette, A., Fynbo, J., Moller, P., Kaufer, A., Andersen, M., Wijers, R., and Page, M. J. (2005). VLT/UVES spectroscopy of GRB050820. *GRB Coordinates Network*, 3860:1–+.

Ledoux, C., Vreeswijk, P., Smette, A., Jaunsen, A., and Kaufer, A. (2006). VLT/UVES observations of GRB 060607. *GRB Coordinates Network*, 5237:1–+.

Leitherer & Lamers (1991). Si IV and C IV resonance lines as indicators of massive stars in starburst galaxies. *The Astrophysical Journal*, 373:89–99.

Levan, A. J., Osborne, J. P., Tanvir, N. R., Page, K. L., Rol, E., Zhang, B., and Goad, M. R. (2006). The First Swift X-Ray Flash: The Faint Afterglow of XRF 050215B. *The Astrophysical Journal*, 648:1132–1138.

Loeb, A. (2002). Novel Ways to Probe the Universe with Gamma-Ray Bursts and Quasars. In Gilfanov, M., Sunyeav, R., and Churazov, E., editors, *Lighthouses of the Universe: The Most Luminous Celestial Objects and Their Use for Cosmology: Proceedings of the MPA/ESO/MPE/USM Joint Astronomy Conference Held in Garching, Germany, 6-10 August 2001, ESO ASTROPHYSICS SYMPOSIA. ISBN 3-540-43769-X. Edited by M. Gilfanov, R. Sunyaev, and E. Churazov. Springer-Verlag, 2002, p. 137*, pages 137–+.

Lopez, S., Reimers, D., D'Odorico, S., and Prochaska, J. X. (2002). Metal abundances and ionization conditions in a possibly dust-free damped Lyalpha system at z=2.3. *Astronomy and Astrophysics*, 385:778–792.

Lu, L., Sargent, W. L. W., and Barlow, T. A. (1998). The N/Si abundance ratio in 15 damped Ly-alpha galaxies - Implications for the origin of nitrogen. *The Astronomical Journal*, 115:55–+.

Lu, L., Savage, B. D., Tripp, T. M., and Meyer, D. M. (1995). Metal Abundances and Physical Conditions in Two Damped LY alpha Systems toward HS 1946+7658. *The Astrophysical Journal*, 447:597–+.

Mészáros, A., Bagoly, Z., Klose, S., Ryde, F., Balázs, S. L. L. G., Horváth, I., and Borgonovo, L. (2005). On the origin of the dark gamma-ray bursts. *Nuovo Cimento C Geophysics Space Physics C*, 28:311–+.

Meynet & Maeder (2002). Stellar evolution with rotation. VIII. Models at $Z = 10^{-5}$ and CNO yields for early galactic evolution. *Astronomy and Astrophysics*, 390:561–583.

Möller, P., Fynbo, J. P. U., Hjorth, J., Thomsen, B., Egholm, M. P., Andersen, M. I., Gorosabel, J., Holland, S. T., Jakobsson, P., Jensen, B. L., Pedersen, H., Pedersen, K., and Weidinger, M. (2002). Absorption systems in the spectrum of GRB 021004. *Astronomy and Astrophysics*, 396:L21–L24.

Morton, D. C. (2003). Atomic Data for Resonance Absorption Lines. III. Wavelengths Long ard of the Lyman Limit for the Elements Hydrogen to Gallium. *The Astorphysical Journal Supplements*, 149:205–238.

Morton, E., York, E., and Jenkins (1988). A search list of lines for quasi-stellar object absorbtion systems. *The Astrophysical Journal Supplement Series*, 68:449–461.

Nakar, E. (2007). Short-hard gamma-ray bursts. *Physrep*, 442:166–236.

O'Brien & Willingale (2007). Using Swift observations of prompt and afterglow emission to classify GRBs. *ArXiv Astrophysics e-prints*.

Penprase, B. E., Berger, E., Fox, D. B., Kulkarni, S. R., Kadish, S., Kerber, L., Ofek, E., Kasliwal, M., Hill, G., Schaefer, B., and Reed, M. (2006). Spectroscopy of GRB 051111 at z = 1.54948: Kinematics and Elemental Abundances of the GRB Environment and Host Galaxy. *The Astrophysical Journal*, 646:358–368.

Petitjean, P. (1998). Lecture 15, qso absorbtion line systems.

Pian, E., Mazzali, P. A., Masetti, N., Ferrero, P., Klose, S., Palazzi, E., Ramirez-Ruiz, E., Woosley, S. E., Kouveliotou, C., Deng, J., Filippenko, A. V., Foley, R. J., Fynbo, J. P. U., Kann, D. A., Li, W., Hjorth, J., Nomoto, K., Patat, F., Sauer, D. N., Sollerman, J., Vreeswijk, P. M., and Guenther, E. W. (2006). An optical supernova associated with the X-ray flash XRF 060218. *Nature*, 442:1011–1013.

Piran, T. (2005). The physics of gamma-ray bursts. *Reviews of Modern Physics*, 76:1143–1210.

Prochaska, J. (2006). On the perils of curve-of growth analysis: systematic abundance underestimates for the gas in gamma-ray bursts host galaxies. *The Astrophysical Journal*, 650:272–280.

Prochaska, J. X., Chen, H.-W., and Bloom, J. S. (2006). Dissecting the Circumstellar Environment of γ-Ray Burst Progenitors. *The Astrophysical Journal*, 648:95–110.

Prochaska, J. X., Chen, H.-W., Bloom, J. S., Dessauges-Zavadsky, M., O'Meara, J. M., and Foley, R. J. (2007a). The Interstellar Medium of Gamma-Ray Burst Host Galaxies. I. Echelle Spectra of Swift GRB Afterglows. *The Astrophysical Journal Supplement*, 168:231–267.

Prochaska, J. X., Chen, H.-W., Dessauges-Zavadsky, M., and Bloom, J. S. (2007b). Probing the ISM Near Star Forming Regions with GRB Afterglow Spectroscopy: Gas, Metals, and Dust. *ArXiv Astrophysics e-prints*.

Ralchenko, Y. (2005). NIST atomic spectra database . *Memorie della Societa Astronomica Italiana Supplement*, 8:96–+.

Reichart & Price (2002). Evidence for a Molecular Cloud Origin of Gamma-Ray Bursts: Implications for the Nature of Star Formation in the Universe. *The Astrophysical Journal*, 565:174–181.

Riess, A. G., Filippenko, A. V., Challis, P., Clocchiatti, A., Diercks, A., Garnavich, P. M., Gilliland, R. L., Hogan, C. J., Jha, S., Kirshner, R. P., Leibundgut, B., Phillips, M. M., Reiss, D., Schmidt, B. P., Schommer, R. A., Smith, R. C., Spyromilio, J., Stubbs, C., Suntzeff, N. B., and Tonry, J. (1998). Observational Evidence from Supernovae for an Accelerating Universe and a Cosmological Constant. *aj*, 116:1009–1038.

Savage & Sembach (1996). Abundances in the Galactic Halo Gas. In Holt, S. S. and Sonneborn, G., editors, *Cosmic Abundances*, volume 99 of *ASP Conf. Ser.*, pages 315–+.

Savaglio, S., Fall, S. M., and Fiore, F. (2003). Heavy-Element Abundances and Dust Depletions in the Host Galaxies of Three Gamma-Ray Bursts. *The Astrophysical Journal*, 585:638–646.

Savaglio, S., Panagia, N., and Stiavelli, M. (2000). The Metallicity Evolution of Damped Lyman-α systems. In Franco, J., Terlevich, L., López-Cruz, O., and Aretxaga, I., editors, *ASP Conf. Ser. 215: Cosmic Evolution and Galaxy Formation: Structure, Interactions, and Feedback*, pages 65–+.

Schaefer, B. E. (2006). The Hubble Diagram to Redshift > 6 from 69 Gamma-Ray Bursts. *ArXiv Astrophysics e-prints*.

Silva & Viegas (2002). Physical conditions in quasi-stellar object absorbers from fine-structure absorption lines. *Memoirs of the RAS*, 329:135–148.

Sokolov, V. V., Fatkhullin, T. A., Castro-Tirado, A. J., Fruchter, A. S., Komarova, V. N., Kasimova, E. R., Dodonov, S. N., Afanasiev, V. L., and Moiseev, A. V. (2001). Host galaxies of gamma-ray bursts: Spectral energy distributions and internal extinction. *Astronomy and Astrophysics*, 372:438–455.

Sollerman, J., Jaunsen, A. O., Fynbo, J. P. U., Hjorth, J., Jakobsson, P., Stritzinger, M., Féron, C., Laursen, P., Ovaldsen, J.-E., Selj, J., and Thöne, C. C. (2006).

Supernova 2006aj and the associated X-Ray Flash 060218. *Astronomy and Astrophysics*, 454:503–509.

Sollerman, J., Östlin, G., Fynbo, J. P. U., Hjorth, J., Fruchter, A., and Pedersen, K. (2005). On the nature of nearby GRB/SN host galaxies. *New Astronomy*, 11:103–115.

Spitzer, L. (1978). *Physical processes in the interstellar medium*. New York Wiley-Interscience, 1978. 333 p.

Stanek, K. Z., Gnedin, O. Y., and Beacom, J. F. (2006). Protecting Life in the Milky Way: Metals Keep the GRBs Awayt. *Acta Astronomica*, 56:333–345.

Stanek, K. Z., Matheson, T., Garnavich, P. M., Martini, P., Berlind, P., Caldwell, N., Challis, P., Brown, W. R., Schild, R., Krisciunas, K., Calkins, M. L., Lee, J. C., Hathi, N., Jansen, R. A., Windhorst, R., Echevarria, L., Eisenstein, D. J., Pindor, B., Olszewski, E. W., Harding, P., Holland, S. T., and Bersier, D. (2003). Spectroscopic Discovery of the Supernova 2003dh Associated with GRB 030329. *The Astrophysical Journal Letters*, 591:L17–L20.

Starling, R. L. C., Vreeswijk, P. M., Ellison, S. L., Rol, E., Wiersema, K., Levan, A. J., Tanvir, N. R., Wijers, R. A. M. J., Tadhunter, C., Zaurin, J. R., Gonzalez Delgado, R. M., and Kouveliotou, C. (2005). Gas and dust properties in the afterglow spectra of GRB 050730. *Astronomy and Astrophysics*, 442:L21–L24.

Tennyson, J. (2005). *Astronomical spectroscopy : an introduction to the atomic and molecular physics of astronomical spectra*. Imperial College Press advanced physics texts, vol. 2 London: Imperial College Press, 2005 ISBN 1860945295.

Thomsen, B., Hjorth, J., Watson, D., Gorosabel, J., Fynbo, J. P. U., Jensen, B. L., Andersen, M. I., Dall, T. H., Rasmussen, J. R., Bruntt, H., and Laurikainen, E. (2004). The supernova 2003lw associated with X-ray flash 031203. *Astronomy and Astrophysics*, 419:L21–L25.

Tinney, C., Stathakis, R., Cannon, R., Galama, T., Wieringa, M., Frail, D. A., Kulkarni, S. R., Higdon, J. L., Wark, R., and Bloom, J. S. (1998). GRB 980425. *iaucirc*, 6896:1–+.

Trulsen, J. (2006). Radiation.

van Dokkum, P. G. (2001). Cosmic-Ray Rejection by Laplacian Edge Detection. *pasp*, 113:1420–1427.

van Marle, A. J., Langer, N., and García-Segura, G. (2005). Constraints on gamma-ray burst and supernova progenitors through circumstellar absorption lines. *Astronomy and Astrophysics*, 444:837–847.

Viegas, S. M. (1995). Abundances at high redshift: ionization correction factors. *Memoires of the RAS*, 276:268–272.

Vladilo, G., Centurión, M., Bonifacio, P., and Howk, J. C. (2001). Ionization Properties and Elemental Abundances in Damped Lyα Systems. *The Astrophysical Journal*, 557:1007–1020.

Vreeswijk, P., Smette, A., and Fruchter, A. (2005). Low-resolution vl spectroscopy of grbs 991216, 011211 and 021211. *astro-ph/0510404*, 2:12.

Vreeswijk, P. M., Ellison, S. L., Ledoux, C., Wijers, R. A. M. J., Fynbo, J. P. U., Møller, P., Henden, A., Hjorth, J., Masi, G., Rol, E., Jensen, B. L., Tanvir, N., Levan, A., Castro Cerón, J. M., Gorosabel, J., Castro-Tirado, A. J., Fruchter, A. S., Kouveliotou, C., Burud, I., Rhoads, J., Masetti, N., Palazzi, E., Pian, E., Pedersen, H., Kaper, L., Gilmore, A., Kilmartin, P., Buckle, J. V., Seigar, M. S., Hartmann, D. H., Lindsay, K., and van den Heuvel, E. P. J. (2004). The host of GRB 030323 at z=3.372: A very high column density DLA system with a low metallicity. *Astronomy and Astrophysics*, 419:927–940.

Vreeswijk, P. M., Ledoux, C., Smette, A., Ellison, S. L., Jaunsen, A., Andersen, M. I., Fruchter, A. S., Fynbo, J. P. U., Hjorth, J., Kaufer, A., Moller, P., Petitjean, P., Savaglio, S., and Wijers, R. A. M. J. (2006a). Rapid-Response Mode VLT/UVES spectroscopy of GRB060418: Conclusive evidence for UV pumping from the time evolution of FeII and NiII excited- and metastable-level populations. *ArXiv Astrophysics e-prints*.

Vreeswijk, P. M., Ledoux, C., Smette, A., Ellison, S. L., Jaunsen, A., Andersen, M. I., Fruchter, A. S., Fynbo, J. P. U., Hjorth, J., Kaufer, A., Moller, P., Petitjean, P., Savaglio, S., and Wijers, R. A. M. J. (2006b). Rapid-Response Mode VLT/UVES spectroscopy of GRB060418: Conclusive evidence for UV pumping from the time evolution of FeII and NiII excited- and metastable-level populations. *ArXiv Astrophysics e-prints*.

Watson, D., Fynbo, J. P. U., Ledoux, C., Vreeswijk, P., Hjorth, J., Smette, A., Andersen, A. C., Aoki, K., Augusteijn, T., Beardmore, A. P., Bersier, D., Castro Cerón, J. M., D'Avanzo, P., Diaz-Fraile, D., Gorosabel, J., Hirst, P., Jakobsson, P., Jensen, B. L., Kawai, N., Kosugi, G., Laursen, P., Levan, A., Masegosa, J., Näränen, J., Page, K. L., Pedersen, K., Pozanenko, A., Reeves, J. N., Rumyantsev, V., Shahbaz, T., Sharapov, D., Sollerman, J., Starling, R. L. C., Tanvir, N., Torstensson, K., and Wiersema, K. (2006). A logN HI = 22.6 Damped Lyα Absorber in a Dark Gamma-Ray Burst: The Environment of GRB 050401. *The Astrophysical Journal*, 652:1011–1019.

Watson, D., Hjorth, J., Fynbo, J. P. U., Jakobsson, P., Foley, S., Sollerman, J., and Wijers, R. A. M. J. (2007). Very different X-ray to optical column density ratios in gamma-ray burst afterglows: ionisation in GRB environments. *ArXiv Astrophysics e-prints*.

Welty, D. E., Lauroesch, J. T., Blades, J. C., Hobbs, L. M., and York, D. G. (1997). Interstellar Abundances in the Magellanic Clouds. I. GHRS Observations of the Small Magellanic Cloud Star SK 108. *The Astrophysical Journal*, 489:672–+.

White, G. J., Nelson, R. P., Holland, W. S., Robson, E. I., Greaves, J. S., McCaughrean, M. J., Pilbratt, G. L., Balser, D. S., Oka, T., Sakamoto, S., Hasegawa, T., McCutcheon, W. H., Matthews, H. E., Fridlund, C. V. M., Tothill, N. F. H., Huldtgren, M., and Deane, J. R. (1999). The Eagle Nebula's fingers - pointers to the earliest stages of star formation? *Astronomy and Astrophysics*, 342:233–256.

Wolf & Podsiadlowski (2007). The metallicity dependence of the long-duration gamma-ray burst rate from host galaxy luminosities. *memoires of the RAS*, 375:1049–1058.

Woosley & Heger (2006). The progenitor stars of gamma-ray bursts. *The Astrophysical Journal*, 673:914–921.

Woosley, S. E. (2005). The Supernova Gamma-Ray Burst Connection. In *Bulletin of the American Astronomical Society*, pages 1426–+.

Woosley & Weaver (1995). The Evolution and Explosion of Massive Stars. II. Explosive Hydrodynamics and Nucleosynthesis. *The Astrophysical Journal Supplements*, 101:181–+.

Yoon & Langer (2005). Evolution of rapidly rotating metal-poor massive stars towards gamma-ray bursts. *Astronomy and Astrophysics*, 443:643–648.

Zhang, B., Zhang, B.-B., Liang, E.-W., Gehrels, N., Burrows, D. N., and Mészáros, P. (2007). Making a Short Gamma-Ray Burst from a Long One: Implications for the Nature of GRB 060614. *The Astrophysical Journal, Letters*, 655:L25–L28.

Zhang & Mészáros (2004). Gamma-Ray Bursts: progress, problems and prospects. *International Journal of Modern Physics A*, 19:2385–2472.

Zwaan, M. A., van der Hulst, J. M., Briggs, F. H., Verheijen, M. A. W., and Ryan-Weber, E. V. (2005). Reconciling the local galaxy population with damped Lyman α cross-sections and metal abundances. *Memoirs of the RAS*, 364:1467–1487.